Deutsches Zentrum
DLR  für Luft- und Raumfahrt

Universität
zu Köln

# Properties of Tailored Granular Media

# Inaugural-Dissertation

zur

Erlangung des Doktorgrades

der Mathematisch-Naturwissenschaftlichen Fakultät

der Universität zu Köln

vorgelegt von

Jan Haeberle

aus Fürth

Köln, 2018

Berichterstatter:                        Prof. Dr. Matthias Sperl
(Gutachter)                           Prof. Dr.-Ing Dr.-Ing E.h. A. Erman Tekkaya

Tag der mündlichen Prüfung:     11. Januar 2019

# ABSTRACT

The macroscopic behavior of granular media is determined by interactions at the grain scale. While some phenomena in granular media can be explained by hard sphere models, experiments always deal with friction, van-der-Waals forces, liquid bridge formation and tribocharging. In how far these interactions determine the macroscopic behavior and the relative strength of each interaction in a real experiment are often difficult to estimate. In this thesis, we investigate how changes at the surfaces of granular spheres can influence the macroscopic behavior of a granular medium. In a first experiment, we measure the rheological properties of surface modified granular particles. Such modifications necessarily influence multiple factors at once and so we measure the influence of the surface modifications on friction, wettability and triboelectric charging behavior and then correlate the changes at the grain scale to the macroscopic behavior. In a second experiment, we investigate in how far charging effects due to tribocharging can determine the packing structure of a granular packing. In the context of controlling the triboelectric effect, we investigate the stochastic nature of exchanged charges in collisions of granular particles and investigate the effect of surface treatments on triboelectric charging behavior. We show that triboelectric charging can indeed define the packing structure and lead to ordered structures in which electrostatic potential is minimized. The effect of boundary conditions is also investigated. Finally, we show that wall friction and piston shape influence the force propagation and displacements in a two dimensional granular medium.

# Zusammenfassung

Das makroskopische Verhalten granularer Medien wird von Interaktionen auf Partikelebene bestimmt. Obwohl einige granulare Phänomene durch harte Kugel Modelle erklärt werden können beinhalten Experimente immer Reibung, van-der-Waals Kräfte, Wasserbrücken und triboelektrisches Aufladen. Inwieweit diese Interaktionen das makroskopische Verhalten bestimmen und die relative Stärke der einzelnen Interaktionen in realen Experimenten sind oft schwierig abzuschätzen. In dieser Dissertation untersuchen wir, wie Veränderungen an der Oberfläche von granularen Kugeln die makroskopischen Eigenschaften des Mediums beeinflussen. In einem ersten Experiment messen wir die rheologischen Eigenschaften von oberflächenmodifizierten granularen Teilchen. Solche Modifikationen beeinflussen zwangsläufig mehrere Faktoren auf einmal und deshalb messen wir den Einfluss der Oberflächenmodifikationen auf Reibung, Benetzbarkeit und triboelektrisches Aufladungsverhalten und korrelieren dann die Veränderung auf Partikelebene mit dem makroskopischen Verhalten. In einem zweiten Experiment untersuchen wir inwieweit Ladungseffekte durch Triboelektrizität die Packungsstruktur granularer Packungen bestimmen. In dem Zusammenhang, den triboelektrischen Effekt zu kontrollieren, untersuchen wir die stochastische Natur der ausgetauschten Ladungen in Kollisionen granularer Teilchen und untersuchen den Effekt von Oberflächenmodifikationen auf das triboelektrische Aufladungsverhalten. Wir zeigen, dass triboelektrisches Aufladen tatsächlich die Packungsstruktur definieren kann und zu geordneten Strukturen führt, in denen das elektrostatische Potential minimiert wird. Der Einfluss von Randeffekten wird ebenfalls untersucht. Schließlich zeigen wir, dass Wandreibung und Form von Kolben die Kraftausbreitung und das Verschiebungsverhalten in einem zweidimensionalen granularen Medium beeinflussen.

# CONTENTS

# LIST OF ABBREVIATIONS

**1D** one dimensional

**2D** two dimensional

**3D** three dimensional

**A/D** analog-digital (typically converter)

**BCC** body centered cubic

**CT** (X-ray) computed tomography

**FCC** face centered cubic

**HCP** hexagonally close packed

**HMDS** hexamethyldisilazane

**ISS** international space station

**PECVD** plasma enhanced chemical vapor deposition

**PMMA** polymethylmethacrylate

**PP** polypropylene

**PTFE** polytetrafluoroethylene, Teflon

**PTMS** 1H,1H,2H,2H-perfluorodecyltrimethoxysilane

**RCP** random close packing

**RLP** random loose packing

**SA** self assembly

**SC** simple cubic

**SEM** scanning electron microscope

**X-ray** X radiation, Röntgen radiation

# LIST OF SYMBOLS

| Sign | Description | Unit |
|------|-------------|------|
| $a$ | time derivative of the velocity of an object | m/s$^2$ |
| $A$ | peak amplitude during vibration | m |
| $\alpha_s$ | angle at which sliding occurs in the inclined plane experiments | ° |
| $d_{\mathrm{asp}}$ | size of asperities | m |
| $Bo$ | cohesive granular bond number | |
| $q_l$ | bond orientational order parameter | |
| $C_F$ | capacity of Faraday cup | C/V |
| $Q$ | charge | C |
| $\theta$ | contact angle | ° |
| $\tau_p$ | torque at plateau, continuous yield limit | N m |
| $\rho$ | solid density of an object | kg/m$^3$ |
| $E$ | elastic modulus, also called Young's modulus; slope of stress-strain curve in the elastic region | Pa |
| $h_0$ | equilibrium separation due to van-der-Waals forces | m |
| $E^*$ | reduced elastic modulus combining the contributions of two contacting bodies | Pa |
| $E_f$ | Fermi energy | |
| $F$ | force | N |
| $f$ | frequency | 1/s |
| $\mu$ | coefficient of friction | |
| $g$ | gravitational acceleration on earth | m/s$^2$ |
| $A$ | Hamaker constant relating to the strength of van der Waals interactions | |
| $H$ | height of granular column | m |

| Sign | Description | Unit |
|------|-------------|------|
| $I$ | intensity, e.g. optical | J/(m$^2$s) |
| $\Delta P_z$ | inter-plane distance in vertical direction | |
| $m$ | mass of an object | kg |
| $N$ | number of objects | |
| $\varphi$ | packing fraction | |
| $\gamma$ | peak acceleration due to vertical vibrations | m/s$^2$ |
| $\pi$ | ratio of circumference of circle to its diameter | |
| $D_P$ | diameter of top plate in the particle-particle friction experiment | m |
| $\nu$ | Poisson ratio; ratio of transveral expansion for a uniaxially compressed body | |
| $U$ | potential; energy difference between two points | J |
| $p$ | pressure per grain | N/m$^2$ |
| $\Delta P^t$ | difference in pressure compared to the start of the experiment | N/m$^2$ |
| $\tau_{pr}$ | principal stress | N/m$^2$ |
| $g(r)$ | radial distribution function, also known as pair correlation function | |
| $R$ | radius of object | m |
| $R_g$ | resistance to gas flow of granular column | 1/m$^2$ |
| $\varepsilon_p$ | coefficient of restitution | |
| $n$ | rotation rate in revolutions per second | 1/s |
| $\sigma^s$ | scattering cross section | |
| $h$ | separation between objects | m |
| $\sigma$ | shear stress | N/m$^2$ |
| $\gamma$ | shear strain | |
| $k$ | stress-optical coefficient | m$^2$/N |
| $u$ | superficial gas velocity | m/s |
| $\gamma$ | surface energy | J/m$^2$ |
| $V_c$ | difference in surface potential | V |

| Sign | Description | Unit |
|------|-------------|------|
| $\sigma_T$ | tensile strength | $N/m^2$ |
| $d$ | thickness | m |
| $t$ | time | s |
| $\tau$ | torque | $N\,m$ |
| | | |
| $\varepsilon_0$ | vacuum permittivity | $C^2/(N\,m^2)$ |
| $\eta$ | viscosity as the relation of shear stress and shear strain | $N\,s/m^2$ |
| $V$ | volume | $m^3$ |
| $\dot{V}$ | volumetric flow rate | $m^3/s$ |
| | | |
| $\lambda$ | wave length | m |
| $\phi$ | work function | J |

# 1 INTRODUCTION
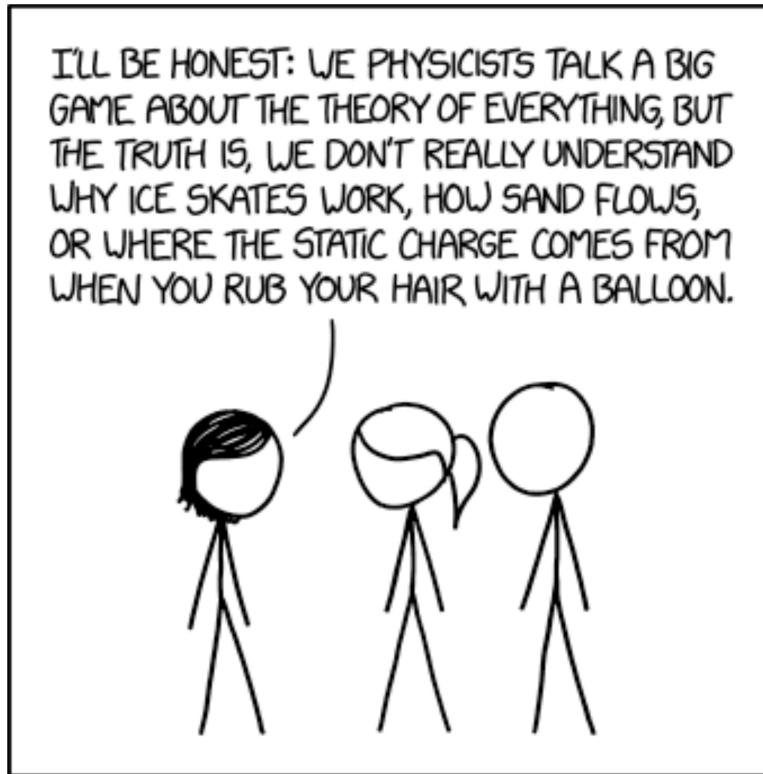


Figure 1.1: xkcd cartoon reprinted with permission from `https://xkcd.com/1867/`[1].

The cartoon depicted in figure 1.1 highlights an apparent discrepancy of how on the one hand, physicists have developed extremely well tested fundamental models describing processes such as happen in high-energy particle collisions at the large hadron collider (LHC), while on the other hand everyday phenomena such as sand flowing in an hourglass or the charges exchanged through frictional contacts remain difficult to predict. One problem that arises when describing such everyday phenomena is that often times there are processes at many length and time scales acting together.

The first example mentioned in figure 1.1 is that we do not know why ice skates work. On a macroscopic level, one would like to describe this system by use of a friction coefficient for metal sliding on ice and such friction coefficients are typically about 0.03 at -3°C [2]. However, to explain why the friction coefficient is so low, exact knowledge of the processes happening in the contact area are required. The current explanations

typically involve formation of a water film due to either pressure melting or frictional heating and a subsequent reduction in friction due to the low viscosity of the water film [2, 3]. A part of the difficulty when it comes to describing this situation and frictional contacts in general is that the real contact area is only a small fraction of the macroscopic contact area. This small fraction might be $\frac{1}{10}$th or $\frac{1}{1000}$th and the difference in resulting local pressures will be two orders of magnitude. Also in terms of time scales, one must consider heat transfer rates to the ice, melting rate at the contact and compare those to the macroscopic sliding speeds.

The second example in figure 1.1 considers the flowing of sand such as it might be encountered in an hourglass. Flowing of sand is fundamentally different to that of other media such as liquids. The flow of a Newtonian liquid through an opening is well described by Bernoulli's equation and the flow velocity will be described well by continuum quantities like the pressure exerted by the liquid on top. This works because water molecules are orders of magnitude smaller than even a small opening and because the pressure is distributed isotropically in the medium.

A granular medium like sand is an athermal agglomerate of macroscopic constituents which interact via dissipative contacts. The concept of pressure is different to that in a liquid in the sense that the force imparted on every grain of sand will be the sum of the contact forces on the grain and this quantity varies considerably even between neighboring grains [4, 5]. Instead of a scalar continuum quantity like liquid pressure, the forces in a granular system are characterized by formation of force networks and in fact the flow of sand through the orifice does not depend on the amount of material on top [6]. To describe the flow of sand through the orifice, the force network at the interface between granular medium and orifice needs to be considered. The important characteristic here is that the opening is not many orders of magnitude greater in size than the grains of sand. This can lead to effects like arching that can either temporarily or permanently stop the flow [6, 7]. The distance over which arches form depends critically on the friction between particles [8].

So as we can see, the behavior of the granular medium flowing through an orifice which may be in a small hourglass or in a giant corn silo is defined by the interactions of the particles which happen in contacts where asperities of a few micrometers determine if the system will arch or not. This is also an example of how the arrangement of the constituents defines the macroscopic behavior. Continuum models of granular media that do not account for the structure of the granular medium have no option to describe such phenomena [8].

The third example of figure 1.1 is about the electric charge that appears when we rub

our hair with a balloon. We call this phenomenon triboelectricity and it is indeed still poorly understood. A number of mechanisms that involve different exchanged charge carriers have been proposed [9–11] and depending on the environmental conditions some mechanisms will be more important than others [12–14]. In addition to that, a discharge step immediately following the tribocharging step has been suggested to explain experimental findings [15, 16]. What also makes tribocharging so difficult to predict is that the macroscopic effects can be caused by a relatively small fraction of atoms in the contact region. For the charge densities measured in the collision between a 2 mm glass sphere and a PTFE slab such as will be presented in chapter 4, only about 1 in every $10^6$ atoms in the contact region would need to transfer an elementary charge to account for the measured charge densities. Despite the small length and time scales on which tribocharging occurs, the effects of it can be macroscopically visible such as in spectacular volcano plumes [17, 18] or dust devils [19].

The systems we have mentioned this far are not just of scientific interest but also highly relevant for industrial processes. Accurate knowledge of frictional properties in extreme conditions are required to allow for safe braking of cars on roads and reduction of friction in manufacturing processes yields greater efficiency and less wear on components.

Flow properties of granular media are of immediate interest to pharmaceutical companies, the food industry or anyone handling powders. Clogging of pipes caused by arching [20] and segregation of reaction materials [21] in a fluidized bed reactor are common problem that can be traced back to the granular nature of the medium that is used.

The use of granular media in novel processes such as granular-medium based tube press hardening [22, 23] promises exciting improvements for the light-weight construction of car parts which require high stiffness. In the tube press hardening process, the steel part is heated and subjected to high pressure during the forming process. The pressure is provided by a forming medium which can be a liquid, a gas or a granular medium. The process is illustrated in figure 1.2. To achieve greatest material strength, the steel must be formed while above the austenitization temperature and cooled down quickly enough to attain the martensite structure. This means that hot tube press hardening for steels such as 22MnB5 with an austenitization temperature above 950°C [24] can not be accomplished by e.g. oils as forming medias since those are only stable until 350°C. Gaseous media are an alternative but their use poses different challenges such as leakage and high compressibility. Therefore, granular media which can sustain high temperatures and pressures and do not suffer from leakage are the best choice for the
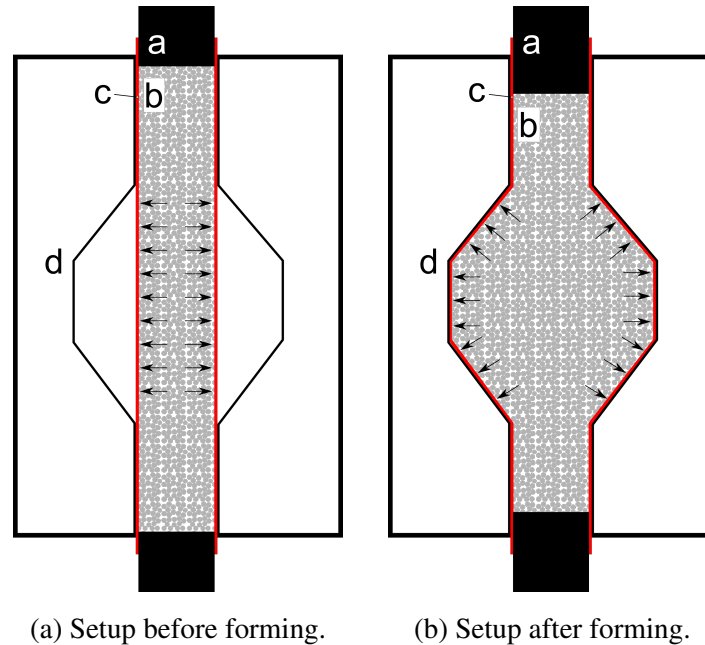
(a) Setup before forming.  (b) Setup after forming.

Figure 1.2: Schematic of the setup used during the granular medium based tube press hardening process. The punch (a) exerts a pressure on the granular medium (b) which pushes the metal sheet (c) against the die (d).

hot tube press hardening process.

However, using a granular medium as forming medium introduces additional challenges because of the non-hydrostatic pressure transmission inside a granular medium. This problem is highlighted in figure 1.2. For ideal forming, the pressure exerted by the granular medium on the tube should be high even in the center of the granular column. In granular media however, a branched force network and friction with the wall lead to decrease of the axial pressure with distance from the pressure source in a granular column in accordance with the Janssen effect [25, 26]. In Janssens original experiments, he showed that the measured pressure on the bottom of a silo filled with corn saturates once enough corn is filled. Once the saturation pressure is approached, the additional pressure of corn placed at the top will be redirected almost completely to the silo walls. This pressure decrease with difference from the piston is the first difficulty arising from using granular media as a forming medium.

The second problem becomes apparent when considering the difference in shape of the granular medium in figure 1.2a and 1.2b. During the forming process, the granular medium needs to not only deform the tube but also change shape itself in order to fit into the die in the final forming step. A system that is elongated in one direction while
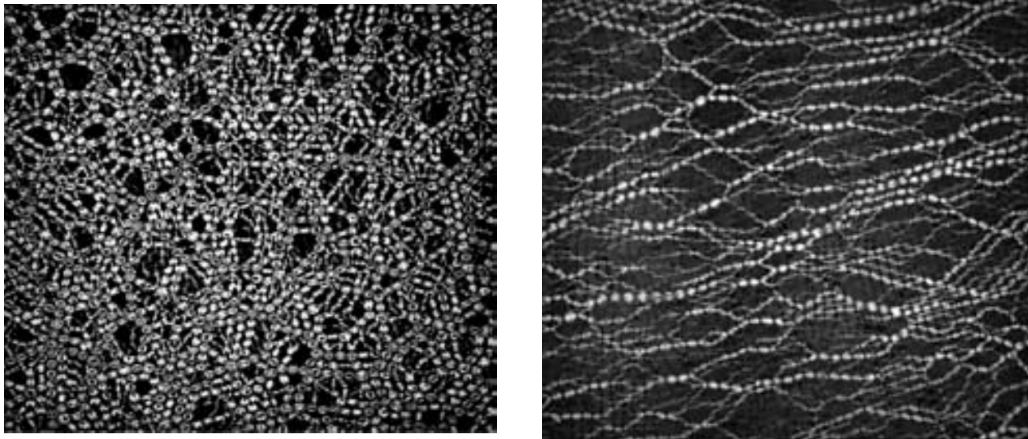
(a) Force chains in compression geometry.



(b) Force chains in pure shear geometry.

Figure 1.3: Force network as it develops for isotropic compression (fig. 1.3a) and pure shear (fig. 1.3b). The force network in the case of isotropic compression has short range correlations of the force network. The force network in the pure shear geometry instead exhibits long range correlations in the direction in which the shear is applied. Reprinted with permission from [4]

being compressed perpendicular to that direction is referred to as pure shear and the force network that develops is qualitatively different to a pure compressive system [4]. The force networks that were measured for each geometry are demonstrated in figure 1.3. Majmudar and Behringer measured long-range correlations in the direction of force chains in a sheared system, whereas isotropically compressed systems exhibited short-range correlations of the forces. In addition, the distributions of normal forces were qualitatively different.

In summary, using granular media as forming media in tube hydroforming requires understanding of both the force propagation and the shear response of the granular medium. The behavior of a granular medium depends on interactions at all scales: microscopic interactions at the grain scale determine the force network and finally the macroscopic response that we measure. This motivates a study of how exactly the macroscopic behavior changes when microscopic parameters are modified by e.g. surface treatment of the particles making up the granular medium. This thesis tackles this question. An overview of the interdependence between microscopic and macroscopic interactions in granular media as well as a note about which chapter of this thesis will discuss these topics is given in figure 1.4.

In chapter 2, we will present measurements on the influence of surface treatments
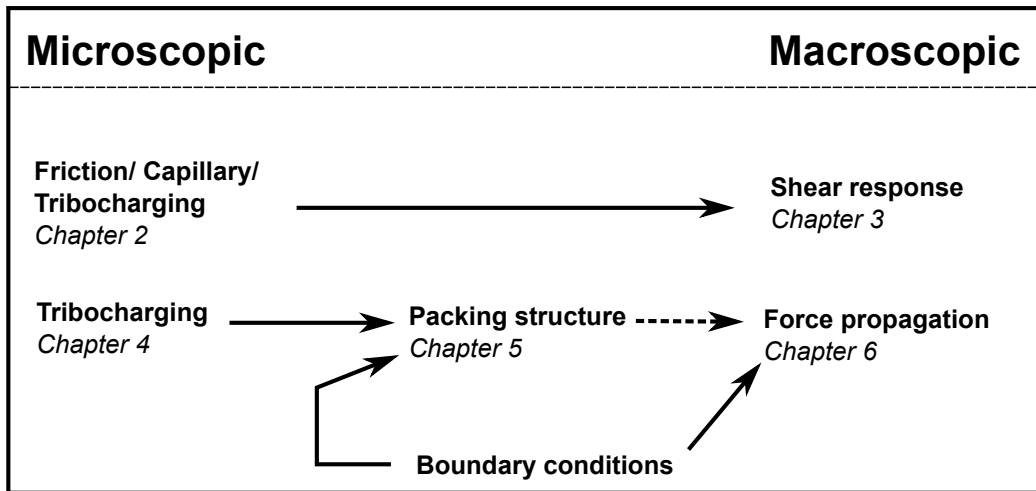
Figure 1.4: Interdependence between microscopic and macroscopic interactions in granular media. The arrows can be read as "influences".

on the microscopic interactions relevant for granular media. These measurements include friction, capillary bridge formation and triboelectric charging behavior of zirconia beads whose surface has been coated with a flowing agent, graphite, boron nitride or a carbofluorination technique. The modifications at grain scale are related to the macroscopic flowing behavior and shear response in chapter 3.

The second part of this thesis is dedicated to a novel approach to influencing the packing structure of granular media through the use of triboelectric charging. For this purpose, we investigate the stochastic nature of triboelectric charging and the feasibility of modifying the charging behavior through surface treatment in chapter 4. In chapter 5 we then show that the packing structure is indeed defined by triboelectric charging. Finally the influence of boundary conditions like wall friction and piston shape on the force transmission in granular media is explicitly shown in chapter 6.

# BIBLIOGRAPHY

[1]  R. Munroe. *xkcd: Physics Confession*. July 24, 2017. URL: https://xkcd.com/1867/ (visited on 10/23/2018).

[2]  F. P. Bowden and T. P. Hughes. "The Mechanism of Sliding on Ice and Snow". *Proceedings of the Royal Society A: Mathematical, Physical and Engineering Sciences* 172.949 (Aug. 3, 1939), pp. 280–298.

[3]  S. C. Colbeck, L. Najarian, and H. B. Smith. "Sliding temperatures of ice skates". *American Journal of Physics* 65.6 (June 1, 1997), pp. 488–492.

[4]  T. S. Majmudar and R. P. Behringer. "Contact force measurements and stress-induced anisotropy in granular materials". *Nature* 435.7045 (June 2005), pp. 1079–1082.

[5]  R. P. Behringer, K. E. Daniels, T. S. Majmudar, and M. Sperl. "Fluctuations, correlations and transitions in granular materials: statistical mechanics for a non-conventional system". *Philosophical Transactions of the Royal Society of London A: Mathematical, Physical and Engineering Sciences* 366.1865 (Feb. 28, 2008), pp. 493–504.

[6]  M. A. Aguirre, J. G. Grande, A. Calvo, L. A. Pugnaloni, and J.-C. Géminard. "Pressure Independence of Granular Flow through an Aperture". *Physical Review Letters* 104.23 (June 11, 2010), p. 238002.

[7]  A. Janda, I. Zuriguel, A. Garcimartín, L. A. Pugnaloni, and D. Maza. "Jamming and critical outlet size in the discharge of a two-dimensional silo". *EPL (Europhysics Letters)* 84.4 (2008), p. 44002.

[8]  L. Pournin, M. Ramaioli, P. Folly, and T. M. Liebling. "About the influence of friction and polydispersity on the jamming behavior of bead assemblies". *The European Physical Journal E* 23.2 (June 2007).

[9]  D. J. Lacks, N. Duff, and S. K. Kumar. "Nonequilibrium Accumulation of Surface Species and Triboelectric Charging in Single Component Particulate Systems". *Physical Review Letters* 100.18 (May 2008), p. 188305.

[10] L. S. McCarty, A. Winkleman, and G. M. Whitesides. "Ionic Electrets: Electrostatic Charging of Surfaces by Transferring Mobile Ions upon Contact". *Journal of the American Chemical Society* 129.13 (Apr. 2007), pp. 4075–4088.

[11]  F. Galembeck, T. A. L. Burgo, L. B. S. Balestrin, R. F. Gouveia, C. A. Silva, and A. Galembeck. "Friction, tribochemistry and triboelectricity: recent progress and perspectives". *RSC Adv.* 4.109 (Nov. 2014), pp. 64280–64298.

[12]  S. R. Waitukaitis, V. Lee, J. M. Pierson, S. L. Forman, and H. M. Jaeger. "Size-dependent same-material tribocharging in insulating grains". *Physical Review Letters* 112.21 (2014), p. 218001.

[13]  T. R. D. Ducati, L. H. Simões, and F. Galembeck. "Charge Partitioning at Gas-Solid Interfaces: Humidity Causes Electricity Buildup on Metals". *Langmuir* 26.17 (Sept. 2010), pp. 13763–13766.

[14]  T. Shinbrot, T. S. Komatsu, and Q. Zhao. "Spontaneous tribocharging of similar materials". *EPL (Europhysics Letters)* 83.2 (July 2008), p. 24004.

[15]  T. Matsuyama and H. Yamamoto. "Charge relaxation process dominates contact charging of a particle in atmospheric conditions". *Journal of Physics D: Applied Physics* 28.12 (1995), p. 2418.

[16]  J. Haeberle, A. Schella, M. Sperl, M. Schröter, and P. Born. "Double origin of stochastic granular tribocharging". *Soft Matter* 14.24 (2018), pp. 4987–4995.

[17]  C. Cimarelli, M. A. Alatorre-Ibargüengoitia, U. Kueppers, B. Scheu, and D. B. Dingwell. "Experimental generation of volcanic lightning". *Geology* 42.1 (Jan. 2014), pp. 79–82.

[18]  C. Cimarelli, M. A. Alatorre-Ibargüengoitia, K. Aizawa, A. Yokoo, A. Díaz-Marina, M. Iguchi, and D. B. Dingwell. "Multiparametric observation of volcanic lightning: Sakurajima Volcano, Japan". *Geophysical Research Letters* 43.9 (May 2016), pp. 4221–4228.

[19]  C. D. Stow. "Dust and Sand Storm Electrification". *Weather* 24.4 (Apr. 1969), pp. 134–144.

[20]  H. G. Sheldon and D. J. Durian. "Granular discharge and clogging for tilted hoppers". *Granular Matter* 12.6 (Dec. 1, 2010), pp. 579–585.

[21]  S. Wu and J. Baeyens. "Segregation by size difference in gas fluidized beds". *Powder Technology* 98.2 (Aug. 1998), pp. 139–150.

[22]  H. Chen, A. Güner, N. B. Khalifa, and A. Tekkaya. "Granular media-based tube press hardening". *Journal of Materials Processing Technology* 228 (Feb. 2016), pp. 145–159.

[23]  H. Chen, S. Hess, J. Haeberle, S. Pitikaris, P. Born, A. Güner, M. Sperl, and A. E. Tekkaya. "Enhanced granular medium-based tube and hollow profile press hardening". *CIRP Annals* 65.1 (2016), pp. 273–276.

[24]  L. Vadillo, M. T. Santos, M. A. Gutierrez, I. Pérez, B. González, and V. Uthaisangsuk. "Simulation And Experimental Results Of The Hot Metal Gas Forming Technology For High Strength Steel And Stainless Steel Tubes Forming". *AIP Conference Proceedings*. Vol. 908. Porto (Portugal): AIP, 2007, pp. 1199–1204.

[25]  H. Janssen. "Versuche über Getreidedruck in Silozellen". *Zeitschr. d. Vereins deutscher Ingenieure* 39.35 (1895), pp. 1045–1049.

[26]  M. Sperl. "Experiments on corn pressure in silo cells – translation and comment of Janssen's paper from 1895". *Granular Matter* 8.2 (May 1, 2006), pp. 59–65.

# 2 MICROSCOPIC INTERACTIONS OF TAILORED GRANULAR MEDIA

Modifications of the surface of granular particles influences friction, contact angle and triboelectric charging. We show that a reduction of friction coefficient against a flat surface does not necessarily translate to a reduction of particle-particle friction if the surface roughness is changed at the same time. We also present a method of coating granular media that leads to lower friction, higher contact angle and switches the sign of acquired charges in a triboelectric charging experiment.

## 2.1 INTRODUCTION

The behavior of granular media at the bulk level depends on microscopic interactions in grain contacts. Cohesion between constituents determines the boundary between freely flowing powders and cohesive powders prone to clogging in e.g. fluidized bed experiments [27, 28]. Friction is present in all experiments containing granular particles and its presence has important consequences for the dynamics of granular systems, especially dense ones [29]. In the next section, we will review the most common grain-scale interactions relevant for granular media. In section 2.3, we present experiments that investigate how microscopic interactions might change when surface treatments are applied. The surface treatments include common solid lubricants as well as a carbofluorination technique adapted to granular spheres. These results are discussed in section 2.4.

## 2.2 MICROSCOPIC INTERACTIONS IN GRANULAR MEDIA

Predicting macroscopic behavior of granular media has proven to be a difficult task. This may seem surprising, given that on the grain scale the motion of constituents is

simply governed by Newtons second and third laws of motion [30], namely:

$$m\vec{a} = \sum_i \vec{F}_i \qquad\qquad (\text{II}-1)$$

$$\vec{F}_{AB} = -\vec{F}_{BA}, \qquad\qquad (\text{II}-2)$$

where $\vec{F}_{AB}$ describes the force exerted by object $A$ on object $B$. In static granular piles, equation (II−1) requires that the sum of all forces on each sphere is equal to 0. In this section, we will review the forces acting on spherical granular particles and how they scale with particle size and depend on environmental conditions.

GRAVITATIONAL FORCES:    Gravitational forces act on every object proportional to its mass $m$. Therefore, spheres with radii $R$ and density $\rho$ will be subjected to a gravitational force:

$$\vec{F}_g = mg\vec{e}_z = g\rho\frac{4}{3}\pi R^3\vec{e}_z, \qquad\qquad (\text{II}-3)$$

where $\vec{e}_z$ is a unit vector pointing to the center of earth. Because of the $\propto R^3$ scaling, gravitational forces dominate for large sphere sizes. In any experiment in standard laboratory conditions, gravitational forces limit the available ranges for packing densities and pressures to packings that are mechanically stable. When observing a granular medium in a jar, doubling the size of the jar will not alter the local densities inside the granular medium. To achieve lower volume fractions or lower confining pressures, experiments need to be done in microgravity environments like drop tower, parabolic flight, sounding rocket or ISS experiments. Alternative approaches of decreasing the influence of gravity include suspending the granular medium in a liquid or fluidizing the granular medium.

CONTACT FORCES:    The simplest model describing some characteristics of a granular media is the hard-sphere model. In the hard sphere model, all particles are perfect spheres and the interaction potential is 0 if the spheres do not overlap and infinite if they do overlap. No real object is perfectly hard, and real materials deform when a force is applied. Granular deformations for objects in contact are typically related to the contact forces using Hertzian contact mechanics [31]. For two spherical bodies

with radii $R_1$ and $R_2$ that are in an elastic contact with indentation $h$, the normal force $F$ will be [32, p.35]:

$$F = \frac{h^{3/2}}{E^*} \left( \frac{R_1 R_2}{R_1 + R_2} \right)^{1/2} \tag{II-4}$$

where $E^*$ is defined for the materials with Poisson ratio $v_1$ and $v_2$ and Young's moduli $E_1$ and $E_2$:

$$E^* = \frac{3}{4} \left( \frac{1 - v_1^2}{E_1} + \frac{1 - v_2^2}{E_2} \right). \tag{II-5}$$

For in the inelastic regime, see for example ref. [33].

VAN-DER-WAALS FORCES: In non-polar materials, these forces arise from spontaneously induced dipole-dipole interactions between neighboring molecules. The functional form was given by Hamaker [34] based on London's dispersion interaction energy [35] and reads:

$$U(h;R_1,R_2) = -\frac{A}{6} \left( \frac{2R_1 R_2}{r^2 - (R_1 + R_2)^2} + \frac{2R_1 R_2}{r^2 - (R_1 - R_2)^2} + \ln \left[ \frac{r^2 - (R_1 + R_2)^2}{r^2 - (R_1 - R_2)^2} \right] \right), \tag{II-6}$$

where $A$ is the material dependent Hamaker constant and $r = R_1 + R_2 + h$ is the total center-to-center distance of the two spheres. For small separation $h << R_1, R_2$, this equation can be approximated as:

$$U(h;R_1,R_2) = -\frac{AR_1 R_2}{(R_1 + R_2)6h}. \tag{II-7}$$

From the functional form, we see that this force scales with the curvature of contact. Because of this, van-der-Waals forces have roughly the same magnitude regardless of particle size. This means that they are of greater significance if influences of other forces like gravity or electrostatic charging are smaller. Because of the dependence on particle separation, van-der-Waals forces greatly depend on surface roughness [36]. Whether or not cohesive forces can be expected to dominate behavior can be estimated based on the cohesive granular Bond number $Bo$ which is defined as the ratio of cohesive forces to gravitational forces and is [37]:

$$Bo = \frac{3A d_{\mathrm{asp}}}{20\pi \rho g d_p^3 h_0^2}, \tag{II-8}$$
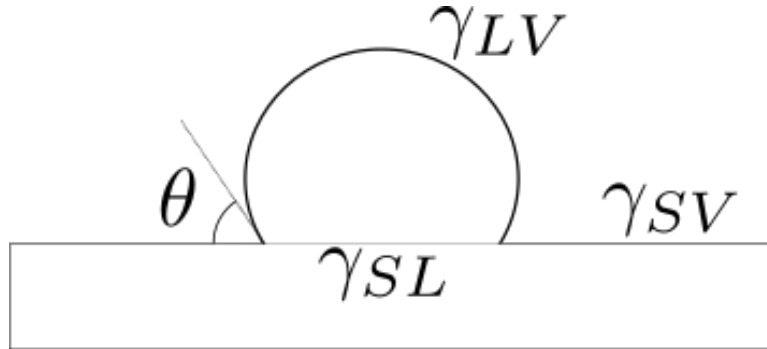
Figure 2.1: A drop of liquid resting on a solid will form an angle $\theta_e$ at the point of contact. Measuring the contact angle can be used to calculate the surface energy of the solid-liquid interface.

where $d_{\mathrm{asp}}$ is the average size of asperities and $h_0$ is the equilibrium separation based on the van-der-Waals forces.

van-der-Waals forces are a major contributor to the cohesive behavior of dry fine powders for example in a fluidized bed [28, 37].

FRICTION:    Friction is the force resisting the motion of two bodies in contact moved relative to each other. It is not a fundamental force but rather a consequence of inter-surface adhesion, surface deformations, and surface roughness and as such, the field of tribology is extremely complex. Dry friction is described by the Coulomb friction law:

$$F_\mu \leq \mu F_N, \tag{II--9}$$

where $F_\mu$ is the frictional force, $\mu$ is the coefficient of friction and $F_N$ is the normal force applied at the contact. The coefficient of friction is an empirical parameter that is typically independent of applied load and apparent area of contact. There are two regimes for dry friction, namely the static and dynamic regime that have different friction coefficients where generally the coefficient of static friction $\mu_s$ is greater than the coefficient of dynamic friction $\mu_d$.

The coefficients of friction have been shown to depend on materials in contact [38], surface topography [39–41] and triboelectricity [11, 42].

Friction in granular systems has been linked to segregation [43], force propagation [44, 45] and avalanching [46].

28
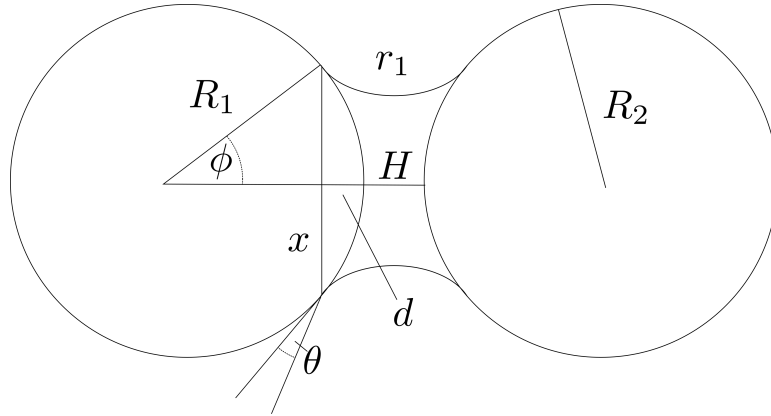
Figure 2.2: Geometry of a liquid bridge of two spheres of radius $R_1$ and $R_2$ a distance $H$ apart. For an accurate calculation of the liquid bridge force, knowledge of $\phi$ and $\theta$ would be required.

LIQUID BRIDGES [36, 47]:   The study of water adsorption onto solid surfaces is a relatively old problem originally described by Young and Laplace [48, 49]. The contact angle of a droplet resting on a solid surface is typically described by:

$$\gamma_{SV} - \gamma_{SL} - \gamma_{LV}\cos(\theta) = 0, \tag{II–10}$$

where $\gamma_{AB}$ is the surface energy density of the $AB$ interface and $\theta$ is the contact angle (see figure 2.1). Measuring the contact angle is an easy way to determine the surface energy difference between the solid-vapor interface and the solid-liquid interface. If $\gamma_{SL} > \gamma_{SV}$, spreading of liquid reduces free energy and the liquid will accumulate in a drop instead of spreading.

Water adsorption plays an important role for granular media because of formation of liquid bridges at the contacts of partially wetted spheres. The forces exerted by a liquid bridge are always attractive and in general depend on the geometry of the meniscus that is formed as illustrated in figure 2.2. Liquid bridge interactions are most relevant for particles in contact since the capillary bridge can rupture for larger sphere separations. In the humidity region where liquid bridges are relevant, the force exerted by a liquid bridge of two spheres in contact is given by [50]:

$$F_b = 2\pi R \gamma_{LV}\cos(\theta) \tag{II–11}$$

The presence of liquids in granular media affect tensile strength[51], flow properties[52, 53] and mixing behavior[54, 55].

ELECTROSTATIC FORCES: The electrostatic force between two homogeneously charged spheres of charge $Q_1$ and $Q_2$ that are a distance $r$ apart will be equal to the Coulomb force:

$$F_q = \frac{Q_1 Q_2}{4\pi\varepsilon_0 r^2} \qquad\qquad (\text{II--}12)$$

where $\varepsilon_0$ is the vacuum permittivity $\varepsilon_0 = 8.85 \times 10^{-12} \text{C}^2\text{N}^{-1}\text{m}^{-2}$. Electrostatic charges on spheres can arise for example from contact electrification which will be discussed in detail in chapter 4. The coulomb forces will be attractive if the charges on the objects have different sign and repulsive for charges of the same sign. Coulomb forces are long range interactions and the contributions of each charged sphere will superimpose to create an electric field that spheres interact with.

MODIFYING INTERACTIONS OF GRANULAR MEDIA  In simulations, properties of granular media like coefficient of friction can easily be changed through simply changing a line of code. In experimental systems, changing one variable, like for example surface roughness, will have an influence on van-der-Waals forces, liquid bridge formation, friction and triboelectric charging. The macroscopic effect of such changes will depend on e.g. the particle size: for small spheres with high $Bo$, increased roughness leads to a decrease in van-der-Waals forces and thus to better flowability. For large spheres with low $Bo$, however, increased roughness will increase friction due to additional interlocking, thus reducing flowability [37].

Methods for influencing friction in experiments include the addition of lubricants to the surface. Solid lubricants can be classified in four categories [38]:

- Carbon-based materials (e.g. graphite or diamond-like carbons): In graphite, the carbon atoms form hexagonally packed and covalently bonded planes. The planes are connected to each other by van-der-Waals forces that are weaker than the in-plane covalent bonds, so that the planes can slide across each other relatively easily [56]. The same mechanism can be used to explain the low friction properties of boron nitride [57]

- Transition metal dichalcogenide compounds (e.g. $MoS_2$ and $WS_2$): Like in graphite, the low friction in these compounds is a result of the crystal structure leading to interlamellar weak planes.

- Polymers (e.g. Teflon): Chemically, teflon is a compound made up of fully fluorinated carbon chains. This results in high inertness and low polarizability, leading to low adhesive forces in the contacts [58]. Shorter chains of fluorocarbons can be seen between two PTFE surfaces in contact as a consequence of wear, influencing frictional properties [59].

- Soft metals (e.g. siver, tin, gold): Thin films of soft metals reduce the friction between surfaces by providing shear accommodation.

These additives are typically deposited onto the surfaces using techniques such as physical vapor deposition (e.g. sputtering) which are typically line of sight and therefore not suited for granular matter. An alternative is chemical vapor deposition (CVD). CVD can be made practical at lower temperatures by use of a plasma (plasma enhanced CDV, PECVD) which offers homogeneous coating even in samples made up of spheres [60].

## 2.3 Experimental methods and results

In an ideal world, one would like to change only a single variable on the grain scale (e.g. friction, hydrophobicity) and then observe the macroscopic influences on granular behavior like packing properties or rheology. However, as we have seen, the way the interactions are connected to each other make such an approach difficult. One solution is to design the experiment in a way that limits all interactions except the one under investigation. We present here an alternative approach that involves combining measurements of multiple relevant parameters on the microscopic scale in an effort to identify the parameters that really influence macroscopic behavior.

We will start by describing the surface treatment methods that were applied. We then characterize the surfaces using scanning electron microscopy. Finally, we show measurements of friction coefficient, contact angle and charging behavior of the coated samples.

### 2.3.1 Surface treatments

We measure changes in friction coefficient and contact angle for industrially applicable granular media where the surface has been modified with commercially available additives or a plasma based carbofluorination technique. The granular media we use are cerium stabilized zirconium oxide spheres (CeraBeads 0.4, Netzsch) with a particle size of 400-600 $\mu$m.

The carbofluorination technique is an adaption of similar plasma deposition techniques [61] to granular samples. In the carbofluorination process, the carbon-carbon bonds in fully fluorinated carbon chains are broken by the plasma and the resulting radicals are attached to the surface by covalent bonds. The carboflourine chains on the surface are chemically similar to PTFE which is known for its low coefficient of friction and high contact angle. Since the deposition method is self-terminating, only a one-molecule thick layer of material is deposited. For details about the deposition method, see appendix (2.6.1).

The first additive we use is a hydrophobic fumed silica (Aerosil® R812 supplied by Evonik industries). The particles are nanometer sized silica spheres that form aggregates on the material to be coated. The additive is turned hydrophobic by coating with hexamethyldisilazane (HMDS). Fumed silica is a flowing agent typically used in industrial fine powder applications to improve flow properties. This effect is based on

(a) Two large spheres in contact without flowing agent.

(b) Two large spheres in contact with flowing agent in the contact.
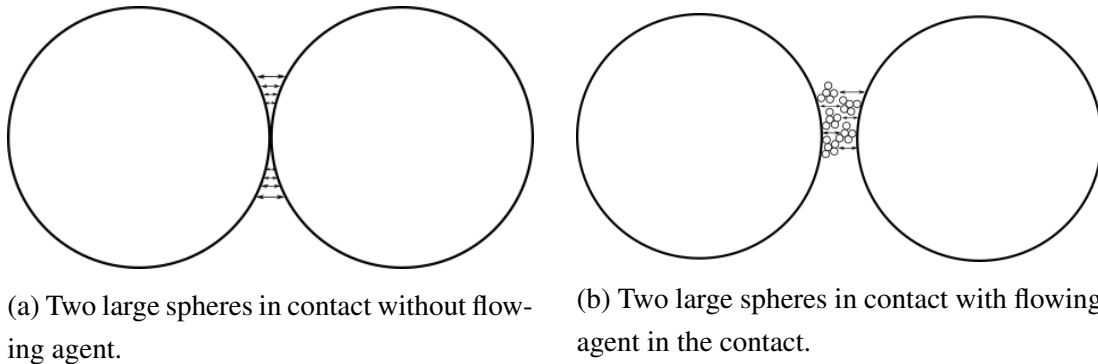
Figure 2.3: Reduction of van-der-Waals forces between two spheres by addition of fumed silica additives. The van-der-Waals forces depend on the curvature of the contacting bodies and their separation. In fig. 2.3a, the forces are high because the distance of the two large spheres is small. In fig. 2.3b, the interaction between the two big spheres is reduced because the separation between them has been increased. The additional interactions of the large spheres with the flowing agent are generally small because the curvature of contact is small.

the reduction of van-der-Waals forces between the contacting bodies as illustrated in figure 2.3. In addition to reducing van-der-Waals forces, fumed silica aggregates can form intertwining networks which need to be broken for the material to flow. This can give suspensions shear-thinning properties, i.e. a reduction of shear stress needed when strain rate is increased. We will refer to results with this additive as "flowing agent".

The additives graphite and hexagonal boron nitride are both common lubricants. The reduction in friction is typically explained by the tendency of these materials to form hexagonal planes, where the bond strength inside the plane is significantly stronger than the bonds between planes. This effectively allows the planes to slide over each other, leading to the low friction coefficient. We use graphite powder supplied by E-Coll and boron nitride powder (HeBoFill® 410) supplied by Henze.

Aerosil, graphite and boron nitride were all purchased in powder form and mixed with the granular medium in a vortex mixer. All samples were cleaned in an argon plasma before the surface treatment. Argon is inert, and so the surfaces are physically cleaned off dirt without chemically altering the surface of the spheres. We compare the surface treated samples to a plasma cleaned sample for reference.

### 2.3.2 MEASUREMENT OF SURFACE COVERAGE AND ROUGHNESS

Scanning electron microscopy (SEM) images of the zirconia beads after surface treatments are shown in figure 2.4. The plasma cleaned surface shown in figure 2.4a is relatively smooth with few asperities. In figure 2.4b, the agglomerates of the flowing agent can be seen on the surface. The agglomerate size varies locally so that these surfaces can be expected to have a higher roughness.

The carbofluorinated surfaces (see figure 2.4c) are visually identical to the plasma cleaned zirconia beads. Both graphite (see figure 2.4d) and boron nitride (see figure 2.4e) are clearly visible in the electron microscopy images and an equal coverage of the entire surface can be verified. For graphite, no visible agglomeration takes place while some is visible for boron nitride. This could indicate a higher roughness of the boron nitride samples.

### 2.3.3 MEASUREMENT OF FRICTION COEFFICIENTS

FRICTION AGAINST A SMOOTH SURFACE    We use an inclined plane setup to measure static ($\mu_s$) and dynamic ($\mu_d$) friction coefficients of the surface treated particles against a smooth surface (CZ-Si-wafer, MicroChemicals GmbH). We chose a Si-wafer because in a first set of experiments with glass microscopy slides as a medium, the spread of results was greater and dynamic friction coefficients were impossible to measure because stick-slip motion set in instead of a constant motion with constant acceleration. A picture of the setup is shown in figure 2.5. We glue three spheres to the bottom of a carrier to prevent rolling of the spheres, while making sure the only contact with the Si-wafer surface is by spheres. We adjust the angle to the horizontal $\alpha$ by slowly moving the linear rail until the slider starts moving down the slope. The static friction coefficient is then calculated as (see appendix for details):

$$\mu_s = \tan(\alpha_s), \tag{II–13}$$

where $\alpha_s$ is the angle at which sliding started. We record videos of the sliding motion using a camera recording at 60 Hz and measure the distance to the initial position at every frame. From this information, we calculate the trajectory down the slope as shown in figure 2.6. We find that a quadratic fit works quite well to describe the data, meaning that the assumption of a constant, velocity-independent dynamic friction coefficient $\mu_d$ appears valid in this context. From a fit of the form $s(t) = \frac{a}{2}t^2 + c$, we calculate the apparent acceleration down the slope.
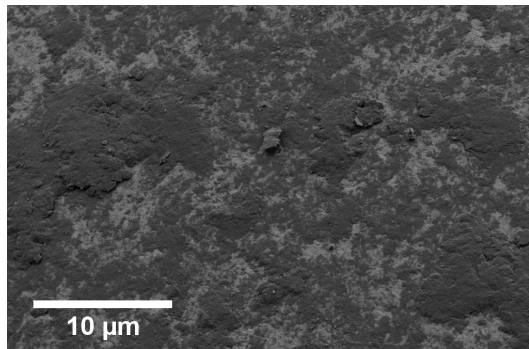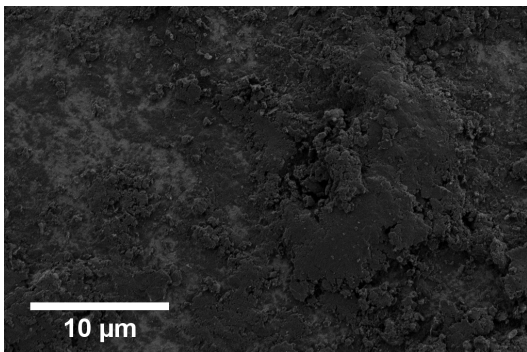
34
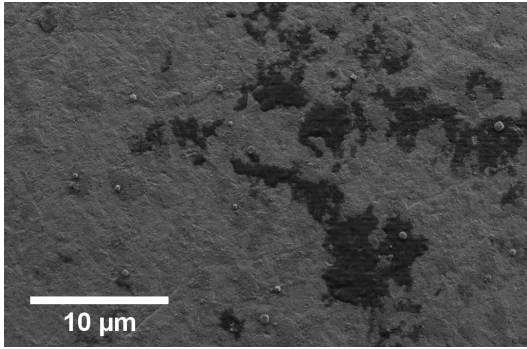
(a) Plasma cleaned zirconia beads.
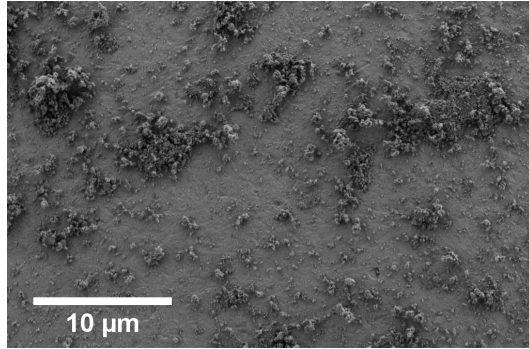


(b) Zirconia beads with flowing agent.
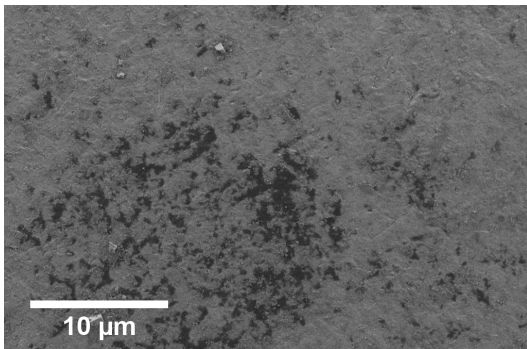


(c) Carbofluorinated zirconia beads.



(d) Zirconia beads coated with graphite.



(e) Zirconia beads coated with boron nitride.

Figure 2.4: Electron microscopy images of the surface on zirconia beads after applying the specified surface treatment.
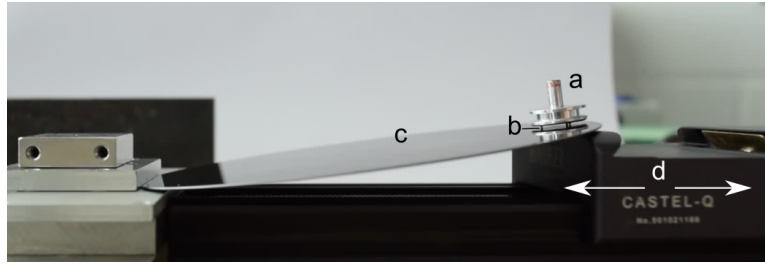
Figure 2.5: Setup used to measure static and dynamic friction coefficients. The components are: The slider (a) with 3 surface treated particles (b) glued to the bottom sits on top of a silicon wafer (c). The angle to the horizontal is increased by moving the linear rail (d) further left.
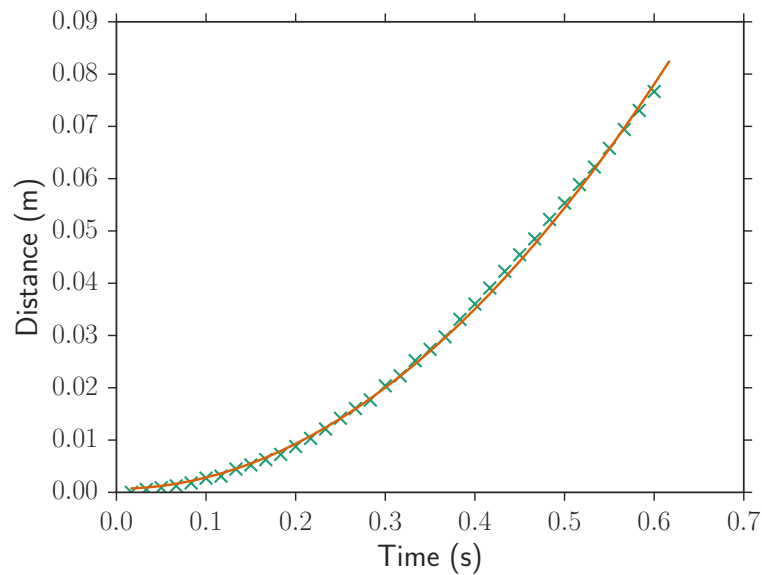


Figure 2.6: Trajectory down the slope as determined from analyzing video footage (crosses). The solid line is a quadratic fit from which we can calculate the effective acceleration down the slope.

Table 2.1: Measured friction coefficients.

| Treatment | $\alpha(°)$ | $\Delta\alpha$ | $\mu_s$ | $\Delta\mu_s$ | $a(ms^{-2})$ | $\Delta a$ | $\mu_d$ | $\Delta\mu_d$ | $\mu_{pp}$ | $\Delta\mu_{pp}$ |
|---|---|---|---|---|---|---|---|---|---|---|
| Cleaned | 12.4 | 2.5 | 0.22(1) | 0.046 | 0.741 | 0.460 | 0.14(3) | 0.052 | 0.37(6) | 0.016 |
| Carboflourinated | 10.9 | 1.2 | 0.19(4) | 0.022 | 0.401 | 0.192 | 0.15(7) | 0.022 | 0.40(9) | 0.010 |
| Flowing agent | 10.4 | 1.0 | 0.18(3) | 0.018 | 0.296 | 0.122 | 0.15(2) | 0.014 | 0.45(6) | 0.010 |
| Graphite | 9.1 | 1.3 | 0.16(0) | 0.023 | 0.306 | 0.230 | 0.12(9) | 0.026 | 0.29(5) | 0.018 |
| Boron nitride | 8.6 | 0.8 | 0.15(1) | 0.014 | 0.081 | 0.042 | 0.14(3) | 0.006 | 0.42(2) | 0.010 |
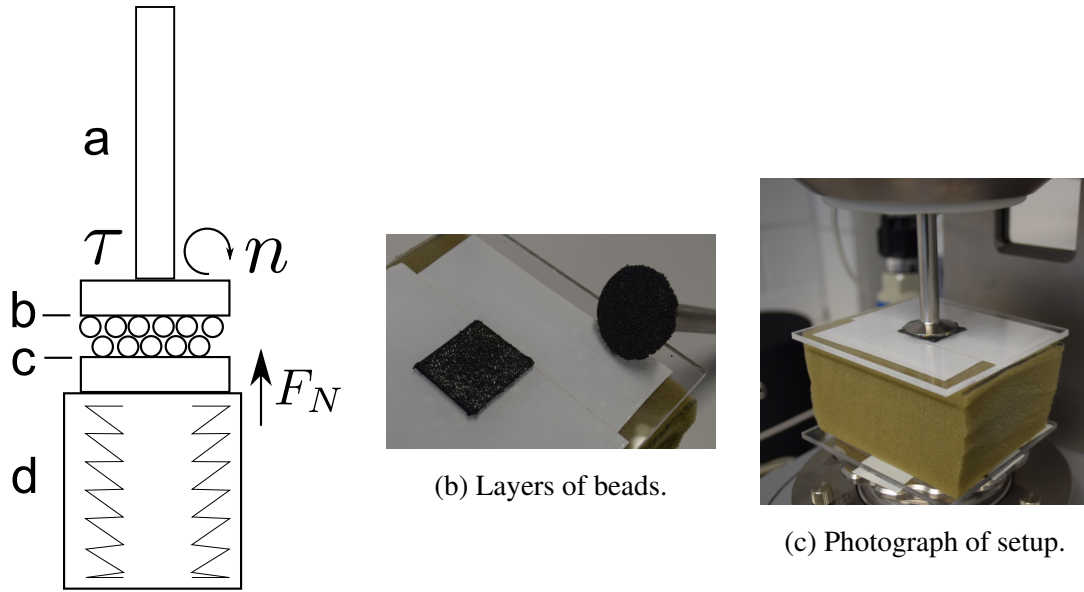
(a) Sketch of setup used to measure particle-particle friction.



(b) Layers of beads.



(c) Photograph of setup.

Figure 2.7: A sketch of the setup is shown in 2.7a. A single layer of particles (b and fig. 2.7b right) is attached to the plate of a rheometer (a). A second layer of particles (c and fig. 2.7b left) is attached to a foam (d) that presses the surfaces together. The layers of particles are shown in figure 2.7b.The setup is shown in figure 2.7c.

From the static friction coefficient and the acceleration down the slope, we can calculate the coefficient of dynamic friction as:

$$\mu_d = \tan \alpha_s - \frac{a}{g \cos \alpha_s}. \tag{II--14}$$

The measured angles, accelerations and coefficients of static and dynamic friction as well as the errors on the quantities are given in table 2.1. Each value is an average of at least 9 measurements. The friction coefficients are also visualized in figure 2.8. We see the highest static friction coefficient for cleaned samples. The carbofluorinated and samples with added flowing agent had a slightly lower friction coefficient, while graphite and boron nitride reduced the friction even more. The differences in dynamic friction coefficient are comparably smaller and all samples are within one standard deviation of each other.
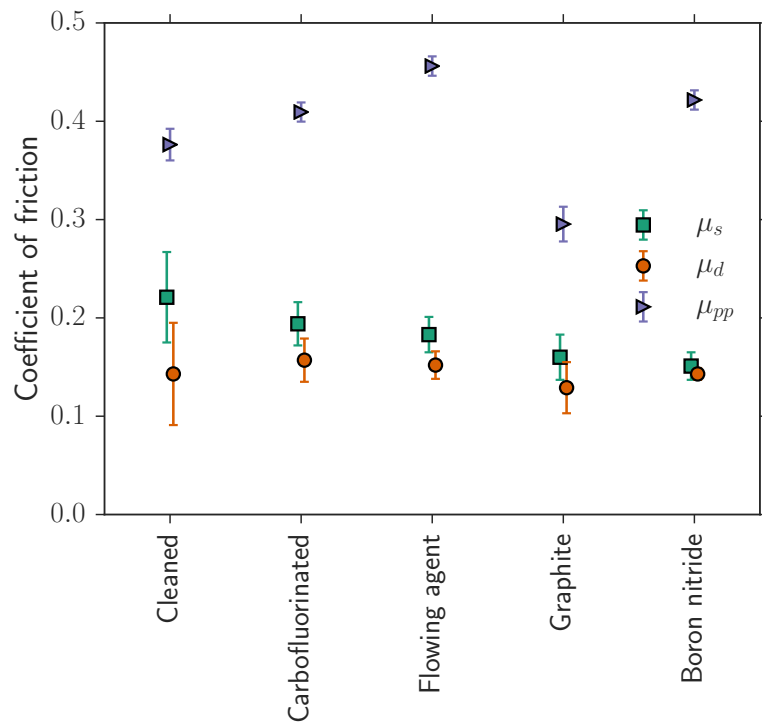
Figure 2.8: Coefficients of static ($\mu_s$) and dynamic ($\mu_d$) friction as calculated from the inclined slope experiments as well as particle particle friction $\mu_{pp}$. The error bars are calculated using error propagation and the statistical error of at least 8 measurements (see appendix (2.6.2) for details).
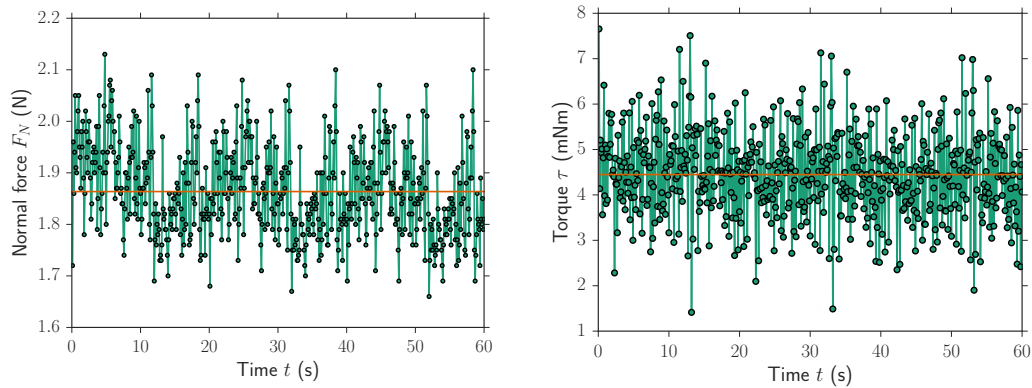
(a) Normal force recorded by the rheometer during one measurement.

(b) Torque recorded by the rheometer during one measurement.

Figure 2.9: Normal force (2.9a) and torque (2.9b) as recorded for a plasma-cleaned sample for two single layers of spheres rotated against each other in a rheometer. Also shown is the mean of each measurement. Both normal force and torque fluctuate strongly throughout the measurement but no systematic drift away from the mean is present.

FRICTION OF PARTICLES IN CONTACT WITH OTHER PARTICLES    In addition to the friction coefficient of individual spheres against a smooth surface, we also measure the particle-particle friction with a setup as shown in figure 2.7. Here, two single layers of spheres are pressed together by the force exerted by a deformed foam. We then rotate the top layer controlled by a rheometer (MCR 102 by Anton Paar) and measure the normal force as well as the torque needed to maintain rotation. The top layer is smaller than the bottom layer and the diameter of the circular top layer thus determines the area of contact. The normal force can be increased by compressing the foam more.

An example of the forces and torques recorded during one such measurement is shown in figure 2.9. Both normal force and torque fluctuate strongly around a mean value during the experiment.

When averaging the normal force and torque over the period of each measurement and plotting the two against each other, we see a linear relation (see fig. 2.10). We verified that the slopes do not depend on rotational speed over the tested range from $0.1\text{s}^{-1}$ to $10\text{s}^{-1}$. Figure 2.10 combines the results of multiple rotational speeds tested. The slope of the linear relation depends on the surface treatment with graphite coated samples exhibiting the lowest slope while samples with added flowing agent exhibit the highest slope. We can relate the slope to a coefficient of particle-particle friction
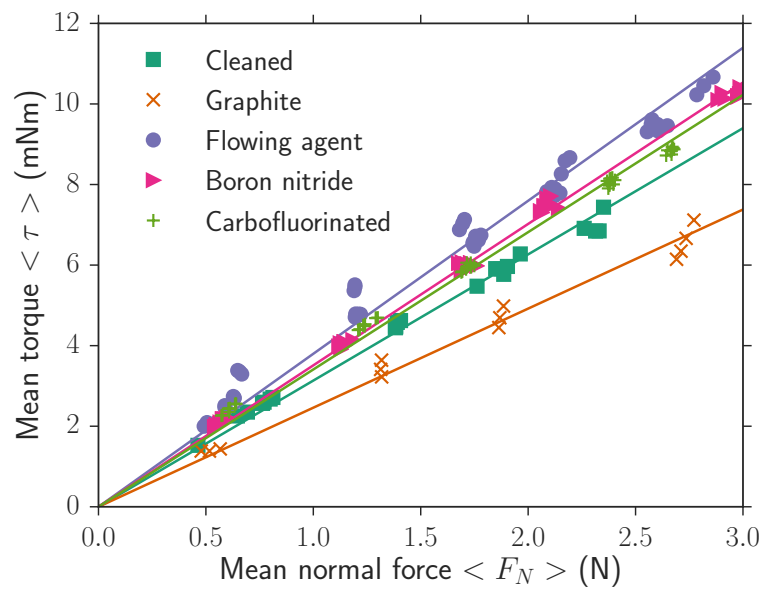
Figure 2.10: The mean torque as a function of applied normal force follows a straight line from which we can calculate a coefficient of particle-particle friction. The slope of the fitted linear functions changes with surface treatment, where the sample with added flowing agent shows the highest slope and the graphite coated sample exhibits the lowest slope. This figure combines the results of various rotation rates from $0.1 s^{-1}$ to $10 s^{-1}$.

$\mu_{pp}$ via the relation (see appendix section 2.6.2):

$$\mu_{pp} = \frac{3\tau}{DF_N},$$

$(\text{II}-15)$

where $D$ is the diameter of the top layer of spheres. The coeffcents of friction for particle particle contacts are listed in table 2.1 and visualized in figure 2.8. The coefficient of particle particle friction is greater and varies more strongly with surface treatment than the static and dynamic coefficents of friction against a smooth plane. The ordering of lowest to highest coefficient of friction is quite different for the particle particle measurements. While the plasma cleaned surfaces exhibited the highest static coefficient against a smooth plane, their particle particle friction coefficient is the second lowest. While boron nitride exhibited the lowest static friction, it's particle particle friction is second highest. The sample with added flowing agent exhibited slightly better static friction than the cleaned or carbofluorinated samples but has the highest friction for particle particle contacts.

### 2.3.4 MEASUREMENT OF CONTACT ANGLES

We additionally measure changes in contact angle with water since formation of water bridges plays a crucial role for granular systems. We measure the contact angle of a layer of zirconia spheres attached to an adhesive strip. We place a drop of $10\,\mu\text{L}$ on the monolayer and immediately record a photo using a Nikon D3300. The images are later analyzed using the imaging software ImageJ with the plugin DropSnake [62]. A picture of the sphere monolayer with water drop and fitted drop curvature is shown in figure 2.11.

Table 2.2: Measured contact angles.

| Treatment | $\theta_l$ (left) | $\Delta\theta_l$ | $\theta_r$ (right) | $\Delta\theta_r$ | Contact angle $\theta$ | $\Delta\theta$ |
|---|---|---|---|---|---|---|
| Cleaned | 78.1 | 8.8 | 74.8 | 6.4 | 76.5 | 7.6 |
| Carboflourinated | 103.7 | 8.1 | 98.2 | 5.7 | 101.0 | 6.9 |
| Flowing agent | 108.9 | 4.0 | 107.8 | 3.5 | 108.3 | 3.7 |
| Graphite | 108.8 | 5.2 | 109.8 | 4.4 | 109.3 | 4.8 |
| Boron nitride | 91.1 | 5.9 | 94.0 | 2.8 | 92.6 | 4.4 |

The contact angles with errors are listed in table 2.2. Each stated value is an average of at least six individual measurements. We individually calculated the contact angles
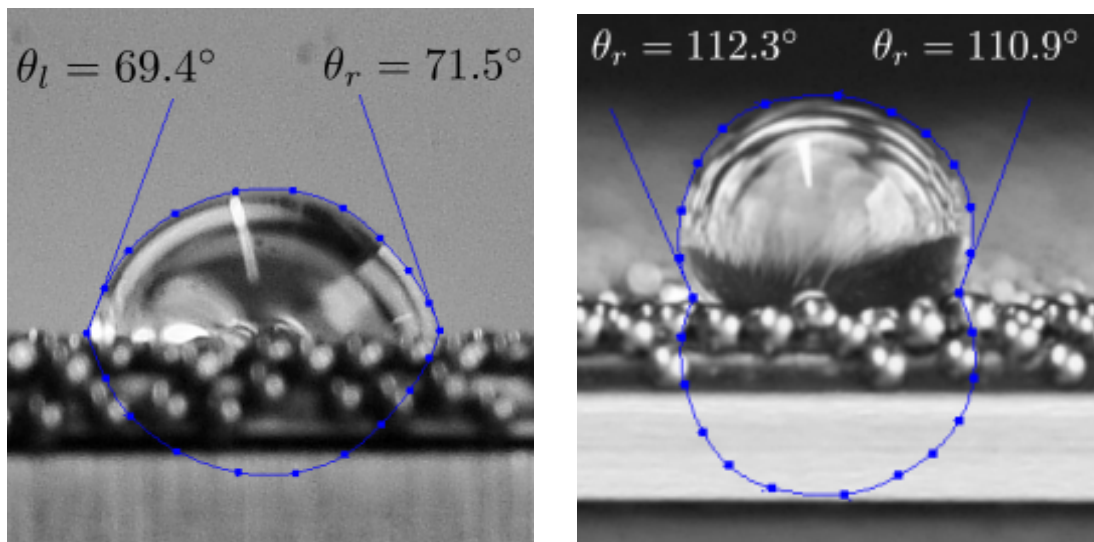
(a) Contact angle for plasma cleaned spheres.

(b) Contact angle for graphite coated spheres.

Figure 2.11: Measurement of water contact angle for plasma cleaned spheres (2.11a) and graphite coated spheres (2.11b). Error bars indicate the statistical error from at least 8 measurements.
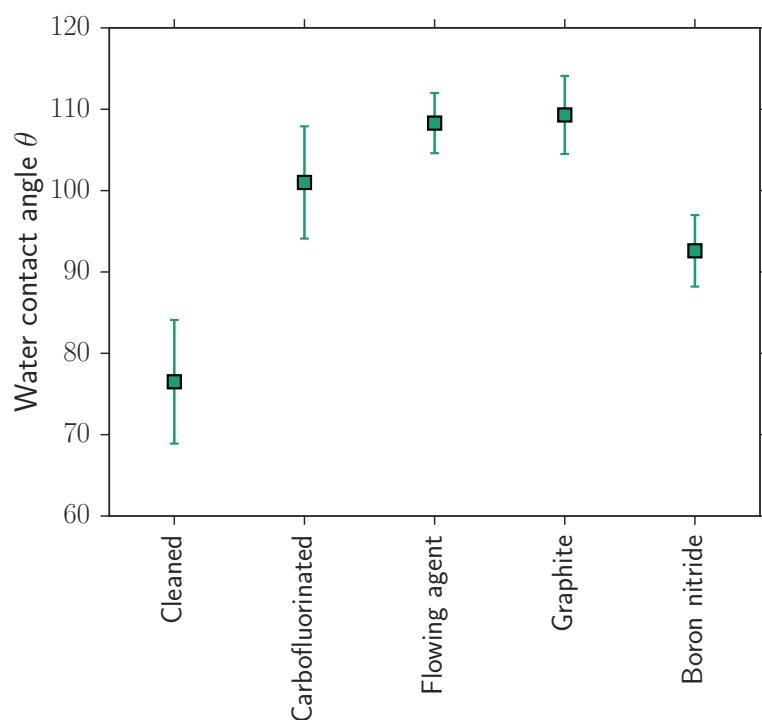


Figure 2.12: Water contact angles of a monolayer of zirconia spheres with specified surface treatments.
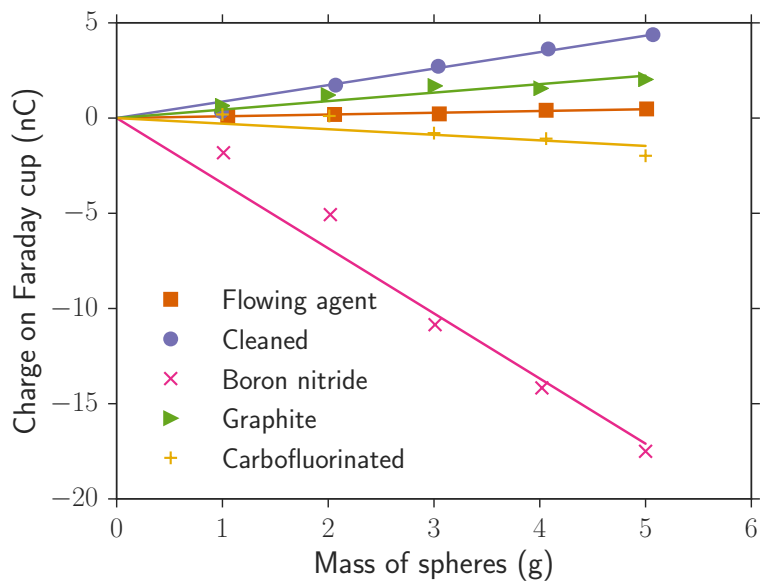
Figure 2.13: Charges acquired by zirconia beads against a polypropylene container for different surface treatments.

on the left and right sides, but no systematic difference between the sides is found. The contact angle results are visualized in figure 2.12. The plasma-cleaned sample features the lowest and graphite the highest contact angle.

### 2.3.5 TRIBOELECTRIC CHARGE MEASUREMENT

Table 2.3: Measured charge to mass ratio.

| Treatment | Charge to mass ratio (nC/g) | Charge per sphere (pC) |
|---|---|---|
| Cleaned | 0.87 | 0.35 |
| Carbofluorinated | -0.29 | -0.12 |
| Flowing agent | 0.093 | 0.038 |
| Graphite | 0.45 | 0.18 |
| Boron nitride | -3.42 | -1.39 |

We perform simple Faraday cup measurements to determine how charging behavior changes with surface treatment. The method of how to measure a charge with a Faraday cup will be described in more detail in chapter 4. We measure the charge that a previously discharged sample of a certain mass acquires during slow pouring

out of a polypropylene (PP) container. The slow pouring and the relatively low sample amount was chosen to maximize the effect of particle-container charging, since particle-particle charging cannot be measured with this method. The results of such a measurement are show in figure 2.13. The charge on the Faraday cup and therefore the charge acquired by the sample increases roughly linearly with sample amount for all surface treatments. The slopes and even the sign of the charge on the Faraday cup vary quite strongly with the plasma-cleaned and graphite coated sample charging positively and the carbofluorinated and boron nitride coated sample charging negatively. The sample with added flowing agent charged positively but by roughly an order of magnitude less than the cleaned sample. The slopes are listed in table 2.3.

## 2.4 DISCUSSION

The results presented in section 2.3 show that a variety of conventionally available surface coating methods as well as the carbofluorination technique can be used to reduce static friction of granular spheres. We also show that these surface treatments additionally influence wettability and charging behavior. Finally, there is a difference between the friction coefficient that is measured against a smooth surface and for particle particle contact.

While the carbofluorination technique does not produce changes visible in e.g. an electron microscope due to the small amount of material deposited, we can see the effects of the fluorinated carbon chains on the surface in a reduced static friction coefficient, higher contact angle and negative charging against a PP container. All these behaviors are consistent with the expected behavior of teflon. While the reduction in static friction is small, it is still remarkable that application of a single molecule layer influences macroscopic behavior measurably.

Addition of the flowing agent led to reduced static friction, higher contact angles and a reduction of the magnitude of charging. The higher contact angles and reduction of charging are expected since the material is surface treated for hydrophobicity and marketed to reduce charging. The flowing agent exhibited the greatest difference between static friction against a smooth surface and particle-particle friction. This could be explained by the increase in roughness due to agglomerate formation as seen in the electron microscopy images (see 2.4b). Against the smooth Si-wafer surface, the roughness on the surface does not lead to interlocking and therefore friction is reduced due to a decrease of effective contact area. When particles are in contact with other particles on the other hand, the roughness of both surfaces leads to increased friction as measured in our experiments.

The same explanation can be used for the boron nitride coated samples, which exhibit the lowest coefficient of static friction but the second highest coefficient of particle-particle friction. Zirconia beads with added boron nitride exhibited strong negative charging against a PP container, showing that such additives can be used to control and even switch charging behavior. However, since boron nitride was used as additive dispersed in the sample as a powder, it is possible that charging was influenced by patches of boron nitride transferring off the surface. We can also only measure the mean charge of all spheres which as the measurements in chapter 4 will show is not sufficient to accurately describe charging behavior.

Graphite coated samples had the second lowest coefficient of static friction, the lowest

coefficient of particle-particle friction, the highest contact angle and did not influence charging behavior strongly compared to cleaned samples.

The contact angles we measure could be related to a surface energy on the spheres according to equation (II–10). However, we chose not to do this since spreading on the single layer of spheres is different to a plane surface and this geometric contribution would have to be accounted for to calculate the surface energy.

## 2.5 CONCLUSION

We have shown that friction, contact angle and triboelectric charging are sensitive to modifications at the surfaces of granular particles. The friction coefficient against a smooth surface differs from the particle particle friction which can be related to surface roughness. We have therefore presented a way to measure friction with and without the influence of roughness and it will depend on the specific experiment which coefficient of friction is most telling of the macroscopic behavior. Modification of the surfaces of granular particles is inherently connected to changes in contact angle and triboelectric charging properties.

# 2.6 APPENDIX

## 2.6.1 THE CARBOFLUORINATION TECHNIQUE

CARBOFLUORINATION BY PLASMA DEPOSITION: All plasma treatments were performed in a Diener electronic Femto low pressure plasma device. Before the plasma deposition, the zirconia beads are cleaned in a plasma with argon (Ar) as gas medium. For the cleaning, we used a gas flow of 10 sccm with the generator operating at $100\,W$ for a duration of 10 minutes.

For the carbofluorination process, we attach a vial filled with roughly 0.5 ml of hexafluoropropene (Hexafuoropropene, Trimer 97 % purchased from T.H. Geyer) to the plasma device. Hexafluoropropene was chosen because according to ref. [61], chains containing double bonds between carbon atoms are particularly suited for plasma deposition. Hexafluoropropene as a trimer is liquid at room temperature, so we use a heating tape to heat it above the boiling point of $110°C$ directly before start of the deposition process. For the deposition process, an Ar gas flux of 2 sccm at pressures of between 0.6 and 0.8 mbar and generator power of 60 W are maintained for 10 minutes. During the deposition, the spheres are in a rotating bottle to achieve homogeneous coverage of the entire surface. After deposition, the spheres are heat treated in a oven at $200\,°C$ for two hours which has been found to increase the stability of the films.

## 2.6.2 CALCULATION OF FRICTION COEFFICIENTS

STATIC AND DYNAMIC FRICTION COEFFICIENT CALCULATIONS: The force balance on the slider in the inclined plane experiments is shown in figure 2.14. The gravitational force $F_g$ can be split up into a component parallel to the slope $F_\parallel$ and one perpendicular to the inclined plane $F_\perp$. The slider will remain stationary, as long as $F_\parallel$ is balanced by the frictional force $F_\mu$ (see situation I in 2.14). According to the Coulomb friction law, the friction force can not be higher than the friction coefficient times the normal force:

$$F_\mu \leq \mu_s F_\perp. \tag{II–16}$$

This means that the slider will start sliding, as soon as the inequality is broken. At this point, $F_\parallel = F_\mu$ so that the coefficient of friction is related to the angle at which sliding first occurs $\alpha_s$:

$$\mu_s = \frac{F_\perp}{F_\parallel} = \frac{mg\sin(\alpha_s)}{mg\cos(\alpha_s)} = \tan(\alpha_s). \tag{II–17}$$
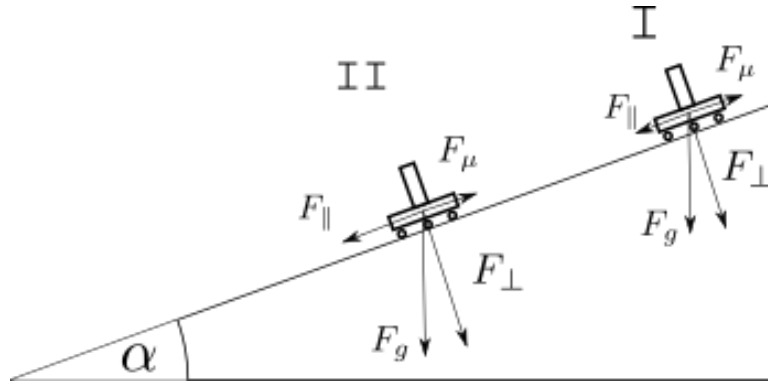
Figure 2.14: Forces acting on the slider: gravitational force $F_g$ can be split up into two components, one down the slope $F_\parallel$ and the other into the Si-wafer $F_\perp$. As long as the slider is stationary (situation I), the friction force $F_\mu$ balances the force down the slope. Once the slider starts moving (situation II), the force down the slope will be higher than the friction force.

Once sliding starts (see situation II in 2.14, there will be a net acceleration because the friction force is reduced to $F_\mu = \mu_d F_\perp$ and $\mu_d < \mu_s$, therefore:

$$ma = F_\parallel - \mu_d F_\perp = mg\sin(\alpha_s) - \mu_d mg\cos(\alpha_s) \qquad \text{(II–18)}$$

$$\Rightarrow \mu_d = \tan(\alpha_s) - \frac{a}{g\cos(\alpha_s)}, \qquad \text{(II–19)}$$

where $a$ is the acceleration down the slope.

The errors on the friction coefficients were calculated using the variance formula:

$$\Delta f(x,y,\dots) = \sqrt{\left(\frac{\partial f}{\partial x}\right)^2 \Delta x^2 + \left(\frac{\partial f}{\partial y}\right)^2 \Delta y^2 + \dots} \qquad \text{(II–20)}$$

where $\Delta f$ is the standard deviation of the function $f$ and $\Delta x$ is the standard deviation of the observable $x$. The coefficient of static friction only depends on one observable, namely the angle $\alpha_s$. We therefore get:

$$\Delta \mu_s = \left| \frac{\partial \tan(\alpha_s)}{\partial \alpha_s} \right| \Delta \alpha_s = \left| \frac{1}{\cos^2(\alpha_s)} \right| \Delta \alpha_s, \qquad \text{(II–21)}$$

where $\Delta \alpha_s$ is the statistic error for the angle at which sliding occurs as determined from the at least 9 measurements performed for each sample. In analog, the error on the coefficient of dynamic friction is:

$$\Delta \mu_d = \sqrt{\left(\frac{1}{\cos^2(\alpha_s)} - \frac{a\sin(\alpha_s)}{g\cos^2(\alpha_s)}\right)^2 (\Delta \alpha_s)^2 + \left(\frac{1}{g\cos(\alpha_s)}\right)^2 (\Delta a)^2} \qquad \text{(II–22)}$$

PARTICLE-PARTICLE FRICTION COEFFICIENT CALCULATION: The coefficient of friction relates the lateral forces to the normal forces. We can assume that the normal forces are equally distributed across the disk of diameter $D$. If we assume that the lateral forces are equally distributed as well, we can relate the lateral forces to the measured torques. The assumption of equal lateral forces is not invalidated by the location dependent speeds on the contact area since we find no dependence of friction on rotation velocity. The total torque is calculated from the average lateral force $\frac{F_l}{\frac{\pi}{4}D^2}$ as:

$$\tau = \int_0^{D/2} dr \int_0^{2\pi} r d\phi \frac{F_l r}{\frac{\pi}{4}D^2} \tag{II–23}$$

$$= \frac{F_l D}{3} \tag{II–24}$$

Since the particle particle friction is the lateral force divided by the normal force, we get:

$$\mu_{pp} = \frac{F_l}{F_N} = \frac{3\tau}{D F_N} \tag{II–25}$$

# BIBLIOGRAPHY

[11]    F. Galembeck, T. A. L. Burgo, L. B. S. Balestrin, R. F. Gouveia, C. A. Silva, and A. Galembeck. "Friction, tribochemistry and triboelectricity: recent progress and perspectives". *RSC Adv.* 4.109 (Nov. 2014), pp. 64280–64298.

[27]    D. Geldart. "Types of gas fluidization". *Powder Technology* 7.5 (May 1, 1973), pp. 285–292.

[28]    A. Castellanos, J. M. Valverde, A. T. Pérez, A. Ramos, and P. K. Watson. "Flow regimes in fine cohesive powders". *Physical review letters* 82.6 (1999), p. 1156.

[29]    M. Schröter. "A local view on the role of friction and shape". *EPJ Web of Conferences* 140 (2017), p. 01008.

[30]    I. Newton. *Philosophiae naturalis principia mathematica*. Vol. 1. Edmond Halley, 1686.

[31]    H. Hertz. "Ueber die Berührung fester elastischer Körper". *Journal für die reine und angewandte Mathematik* 92 (1882), pp. 156–171.

[32]    L. D. Landau and E. Lifshitz. "Theory of Elasticity, vol. 7". *Course of Theoretical Physics* 3 (1986), p. 109.

[33]    H. Masuda and K. Iinoya. "Electrification of particles by impact on inclined metal plates". *AIChE Journal* 24.6 (Nov. 1, 1978), pp. 950–956.

[34]    H. C. Hamaker. "The London—van der Waals attraction between spherical particles". *Physica* 4.10 (Oct. 1, 1937), pp. 1058–1072.

[35]    F. London. "The general theory of molecular forces". *Transactions of the Faraday Society* 33 (1937), pp. 8–26.

[36]    I. Zimmermann, M. Eber, and K. Meyer. "Nanomaterials as flow regulators in dry powders". *Zeitschrift für physikalische Chemie* 218.1 (2004), pp. 51–102.

[37]    A. Castellanos. "The relationship between attractive interparticle forces and bulk behaviour in dry and uncharged fine powders". *Advances in Physics* 54.4 (June 2005), pp. 263–376.

[38]    T. W. Scharf and S. V. Prasad. "Solid lubricants: a review". *Journal of Materials Science* 48.2 (Jan. 1, 2013), pp. 511–531.

[39]  S. Utermann, P. Aurin, M. Benderoth, C. Fischer, and M. Schröter. "Tailoring the frictional properties of granular media". *Physical Review E* 84.3 (Sept. 22, 2011).

[40]  S. Ecke and H.-J. Butt. "Friction between Individual Microcontacts". *Journal of Colloid and Interface Science* 244.2 (Dec. 2001), pp. 432–435.

[41]  J. Meyer, R. Fuchs, T. Staedler, and X. Jiang. "Effect of surface roughness on sliding friction of micron-sized glass beads". *Friction* 2.3 (Sept. 2014), pp. 255–263.

[42]  T. A. L. Burgo, C. A. Silva, L. B. S. Balestrin, and F. Galembeck. "Friction coefficient dependence on electrostatic tribocharging". *Scientific Reports* 3 (Aug. 12, 2013), p. 2384.

[43]  S. Ulrich, M. Schröter, and H. L. Swinney. "Influence of friction on granular segregation". *Physical Review E* 76.4 (Oct. 9, 2007), p. 042301.

[44]  D. L. Blair, N. W. Mueggenburg, A. H. Marshall, H. M. Jaeger, and S. R. Nagel. "Force distributions in 3D granular assemblies: Effects of packing order and inter-particle friction". *Physical Review E* 63.4 (Mar. 27, 2001).

[45]  M. Muthuswamy and A. Tordesillas. "How do interparticle contact friction, packing density and degree of polydispersity affect force propagation in particulate assemblies?" *Journal of Statistical Mechanics: Theory and Experiment* 2006.9 (Sept. 7, 2006), P09003–P09003.

[46]  T. Börzsönyi, T. C. Halsey, and R. E. Ecke. "Two Scenarios for Avalanche Dynamics in Inclined Granular Layers". *Physical Review Letters* 94.20 (May 25, 2005), p. 208001.

[47]  P.-G. De Gennes. "Wetting: statics and dynamics". *Reviews of modern physics* 57.3 (1985), p. 827.

[48]  T. Young. "III. An essay on the cohesion of fluids". *Philosophical Transactions of the Royal Society of London* 95 (Jan. 1, 1805), pp. 65–87.

[49]  P. S. Marquis de Laplace. *Traité de mécanique céleste*. Vol. 1. Crapelet, 1799.

[50]  C. D. Willett, M. J. Adams, S. A. Johnson, and J. P. K. Seville. "Capillary Bridges between Two Spherical Bodies". *Langmuir* 16.24 (Nov. 1, 2000), pp. 9396–9405.

[51]  P. Pierrat and H. S. Caram. "Tensile strength of wet granula materials". *Powder Technology* 91.2 (May 15, 1997), pp. 83–93.

[52] J. M. Valverde and A. Castellanos. "Bubbling Suppression in Fluidized Beds of Fine and Ultrafine Powders". *Particulate Science and Technology* 26.3 (Apr. 29, 2008), pp. 197–213.

[53] S. Nowak, A. Samadani, and A. Kudrolli. "Maximum angle of stability of a wet granular pile". *Nature Physics* 1.1 (Oct. 2005), pp. 50–52.

[54] D. Geromichalos, M. M. Kohonen, F. Mugele, and S. Herminghaus. "Mixing and Condensation in a Wet Granular Medium". *Physical Review Letters* 90.16 (Apr. 25, 2003), p. 168702.

[55] A. Schella, S. Herminghaus, and M. Schröter. "Influence of humidity on triboelectric charging and segregation in shaken granular media". *Soft Matter* 13.2 (2017), pp. 394–401.

[56] R. F. Deacon and J. F. Goodman. "Lubrication by lamellar solids". *Proc. R. Soc. Lond. A* 243.1235 (Feb. 11, 1958), pp. 464–482.

[57] J. O. Koskilinna, M. Linnolahti, and T. A. Pakkanen. "Friction coefficient for hexagonal boron nitride surfaces from ab initio calculations". *Tribology Letters* 24.1 (Oct. 1, 2006), pp. 37–41.

[58] I. Jang, D. L. Burris, P. L. Dickrell, P. R. Barry, C. Santos, S. S. Perry, S. R. Phillpot, S. B. Sinnott, and W. G. Sawyer. "Sliding orientation effects on the tribological properties of polytetrafluoroethylene". *Journal of Applied Physics* 102.12 (Dec. 15, 2007), p. 123509.

[59] P. R. Barry, P. Y. Chiu, S. S. Perry, W. G. Sawyer, S. R. Phillpot, and S. B. Sinnott. "Effect of Fluorocarbon Molecules Confined between Sliding Self-Mated PTFE Surfaces". *Langmuir* 27.16 (Aug. 16, 2011), pp. 9910–9919.

[60] B. Borer, A. Sonnenfeld, and P. Rudolf von Rohr. "Influence of substrate temperature on morphology of SiOx films deposited on particles by PECVD". *Surface and Coatings Technology* 201.3 (Oct. 5, 2006), pp. 1757–1762.

[61] H. Yasuda and T. S. Hsu. "Some aspects of plasma polymerization of fluorine-containing organic compounds". *Journal of Polymer Science: Polymer Chemistry Edition* 15.10 (1977), pp. 2411–2425.

[62] A. Stalder, G. Kulik, D. Sage, L. Barbieri, and P. Hoffmann. "A Snake-Based Approach to Accurate Determination of Both Contact Points and Contact Angles". *Colloids And Surfaces A: Physicochemical And Engineering Aspects* 286.1 (Sept. 2006), pp. 92–103.

# 3 FLOW PROPERTIES OF TAILORED GRANULAR MEDIA

The flow behavior of granular media is related to interactions at grain scale. We measure the tensile strength of surface treated granular media and find that the tensile strength is lower in samples with lower static friction coefficient. We measure an increased continuous torque required to maintain a steady rotation in samples with higher particle-particle friction. We also show that the scaling of the torque against rotation rate depends on friction coefficient and gas velocity in experiments with simultaneous fluidization and shearing.

## 3.1 INTRODUCTION

The flow behavior of granular solids is a topic that has been extensively studied in the context of soil mechanics to understand phenomena such as avalanches or landslides [46, 63]. Depending on the circumstances, the behavior of granular particles will be similar to a solid (e.g. in a sand pile), a liquid (e.g. when pouring cereal) or a gas (e.g. when strongly agitated) [64]. For each regime, different scaling laws apply and the material can transition between one state and another. Due to dissipative collisions, a constant supply of energy is required to keep a granular medium in the flowing state and even more energy to keep it in the gas-like state. In this chapter, we will consider two alternative ways of agitating granular media, namely fluidization by a gas stream and shearing in a rheometer and finally combine both to best characterize granular flow behavior. We will start by reviewing past experiments on the fluidization behavior in section 3.2 and on the response of granular media to shearing in section 3.3. Our experiments and results will be structured similarly and focus on fluidization experiments in section 3.4.1, shear experiments in section 3.4.2 and finally the combination of both processes in section 3.4.3.

## 3.2 Fluidization behavior of granular media

The flow of gas through a static porous medium is governed by Darcy's law which we can write as [65]:

$$\Delta P = R_g H \eta_g u \qquad (\text{III}-1)$$

with $\Delta P$ the pressure difference before and after the bed, $R_g$ the resistance to gas flow imposed by the granular medium, $H$ the height of the bed, $\eta_g$ is the gas viscosity and $u$ the superficial gas velocity, i.e. the total gas flow divided by the tube cross section $u = \frac{\dot{V}}{A_T}$. There exist a number of constitutive equations to describe $R_g$ of granular media, among others the Kozeny-Carman equation [66]:

$$R_g = a \frac{\varphi^2}{(1-\varphi)^3 d_p^2} \qquad (\text{III}-2)$$

where $a$ is a proportionality constant, $\varphi$ is the packing fraction of the granular medium and $d_p$ is the particle diameter. We note the dependence of granular air resistance on packing fraction and particle diameter. This is a continuum approximation that assumes constant $\varphi$ to fully describe the granular medium disregarding ordering or local inhomogeneities.

If we increase the gas velocity going through a cohesionless granular medium, the pressure difference $\Delta P$ will eventually be higher than the gravitational pressure exerted by the packing $P_g = \frac{mg}{A_T}$ where $A_T$ is the cross sectional area of the tube. At this point the granular medium will go from a solid-like state to a fluid-like state where contacts are periodically broken. The fluidization behavior of granular media is qualitatively different for fine powders compared to granular particles of $100\mu$m size or more [27, 28]. Here we will only consider the behavior of spherical zirconia beads with a size of 400-600$\mu$m such as were used in the experiments in chapter 2 and will be used for the experiments here. According to eq. (8) in ref. [27], the zirconia beads are in the Geldart D regime, meaning that fluidization will be accompanied by formation of bubbles and that the bubble velocity is less than the superficial gas velocity.

Fluidization can be used to measure a material's tensile strength as described in ref. [67]. If the granular medium is cohesive, the pressure that can build up in front of the bed before fluidization sets in is increased by the tensile strength $\Delta P_F = \frac{mg}{A_T} + \sigma_T$. As such, the tensile strength can easily be measured by measuring the sudden decrease of pressure at the point of fluidization.

Fluidized beds are additionally of interest for research on granular media because the

fluid flow can be used to prepare packings in densities that are otherwise only attainable by e.g. microgravity experiments or by suspension in a liquid. Schröter et al. have shown that using a water fluidized bed, the packing fraction that is achieved during settling after applying a flow pulse can be set continuously by the flow pulse flow rate [68].

## 3.3 RESPONSE TO SHEAR IN GRANULAR MEDIA

The shear response of granular media is often described using continuum models that attempt to relate the shear stress to shear velocities. This may have been motivated by the early works of Bagnold who found that the shear stress scales with the shear velocity squared for dense suspensions in the limit of large velocities [69]. Since then, a number of scientists have refined such models and the progress is summarized in review papers [64, 70–72].

The shear response is often described using the viscosity $\eta$, which is the factor relating shear stress $\sigma$ and shear rate $\dot{\gamma}$:

$$\sigma = \eta \dot{\gamma}. \tag{III–3}$$

There are three possibilities for the scaling of $\eta$:

1. $\eta$ independent of $\dot{\gamma}$: This is called viscous behavior and fluids who exhibit it are called Newtonian fluid. Examples include water, air and alcohol for the range of strain rates typically encountered. Theoretical predictions for inelastic hard sphere systems also exhibit a Newtonian regime but at low densities and low shear rates not typically encountered in granular media experiments [73].

2. $\eta$ decreasing with increasing $\dot{\gamma}$: This behavior is called shear-thinning and is encountered in paints that flow easily when applied but stop flowing once on the wall. Dense granular media exhibit shear-thinning in the low shear rate regime where formation of shear bands lead to shear-rate independent stresses [74],[75, p.149].

3. $\eta$ increasing with increasing $\dot{\gamma}$: We call this behavior shear-thickening and it is encountered most famously in suspensions of e.g. cornstarch that allow a person to walk on them if they run fast enough even though they will sink if trying to stand still on the suspension. This behavior is common to granular media in the high-shear regime where Bagnold scaling predicts the shear stress to increase

with the shear velocity squared and therefore the viscosity increases linearly with shear rate in this regime [76].

As we can see, shear behavior of granular media is highly complex since shear thinning, shear thickening and viscous behavior can all occur under certain experimental situations. This is exemplified by the experiments performed by Peters et al. [77] who investigated a sheared granular medium in suspension and observed that as the strain rate is increased, the suspension exhibits a shear thinning, a Newtonian and a shear thickening regime. In addition, they related the response to a sudden impact to the structure of the medium. In dense suspensions where the underlying granular medium is structurally jammed, a sphere dropped onto the suspension would rebound whereas it would sink if the granular structure is unjammed. Peters et al. further identified a regime where the underlying force network was initially unjammed but the impact of the sphere was enough to locally jam the network so that the sphere would rebound on impact.

The relation between shearing and granular structure is also investigated by Rietz et al. [78], who show how granular systems locally crystallize when the system is sheared repeatedly.

While many studies have investigated fluidization or shearing in granular media, only few studies investigate the shear response of granular media under simultaneous fluidization [79]. One advantage of being able to control a gas flow going through the granular medium is that the lift force imposed by the gas flow partially counteracts the influence of gravity. This could otherwise only be achieved by suspension of the granular medium in liquid which introduces hydrodynamic interactions and influences rheology measurements. The other alternative would be microgravity experiments which are more difficult to realize.

While shearing of granular systems is a relatively well studied subject predictive theories relating the microscopic particle properties to macroscopic properties like the torque required to shear a sample are missing. We have presented in chapter 2 a series of surface treatments to influence particle behavior at the grain scale and have measured the influence on friction, contact angle and triboelectric charging. On this basis, we can test the same surface treatments with respect to their fluidization and rheological behavior to relate the microscopic properties to macroscopic flow properties.

## 3.4 Experimental methods and results

We perform rheological measurements using the samples prepared in chapter 2 to identify the macroscopic influence of the surface modifications. We measure both the fluidization behavior of the granular samples, the response to shear and the response to shear under simultaneous fluidization. From the measurements we will determine two quantities which could be used to characterize the flow behavior of the granular medium, namely the tensile strength as well as the continuous yield limit and relate these to the microscopic friction measurements.

We use the identical granular media as were prepared in chapter 2, namely cerium stabilized zirconium oxide spheres (CeraBeads 0.4, Netzsch) with a particle size of 400-600 $\mu$m. We applied 4 different surface treatments and compare it to one reference. The samples are:

- **Cleaned**: A reference sample that was cleaned using an inert Ar-plasma. In the following we will compare each surface treatment to this sample.

- **Carbofluorinated**: Chains of fully fluorinated carbon are deposited on the surface of the zirconia spheres, giving the samples surface properties similar to teflon, i.e. a reduced coefficient of static friction, high contact angle against water and a propensity to charge negatively.

- **Flowing agent**: Agglomerates of nanometer-sized glass spheres that effectively increase surface roughness. The samples exhibited a lower coefficient of static friction but higher coefficient of particle-particle friction. The water contact angle was increased compared to the cleaned sample and we measured a reduced absolute charge exchanged during tribocharging.

- **Graphite**: The sample with this solid lubricant exhibited a decrease of both static and particle-particle friction, higher water contact angle and comparable tribocharging behavior to the cleaned sample.

- **Boron nitride**: We added boron nitride as a solid lubricant and measured an increase in surface roughness, a decrease in static friction coefficient but increase in particle particle friction. The sample had a slightly increased contact angle against water and charged oppositely in the tribocharging experiment.

All measurements are done using a rheometer (MCR 102) built by Anton Paar GmbH. The rheometer allows exact control over gas flow rate of dry compressed air and rota-
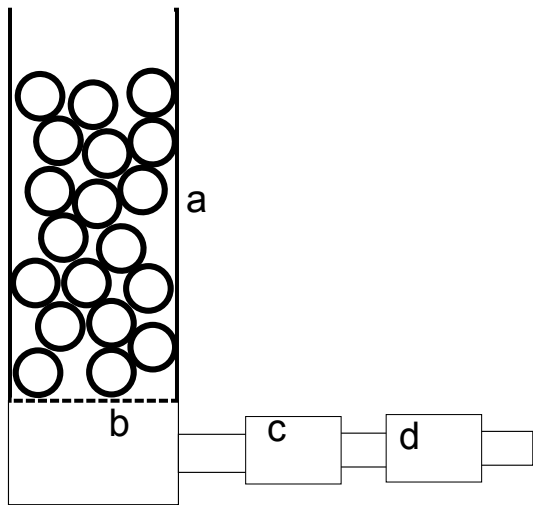
(a) Sketch of setup used for fluidization.
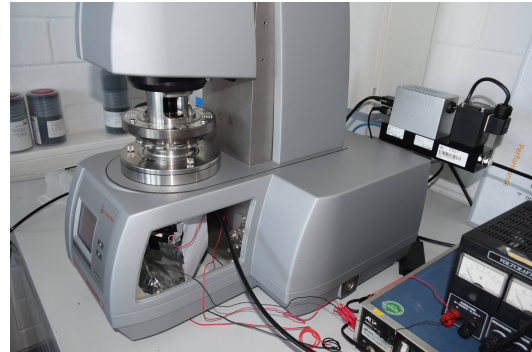


(b) Rheometer MCR 102 by Anton Paar.

Figure 3.1: Setup used to investigate fluidization behavior of granular samples. A gas flow rate $\dot{V}$ is set by the mass flow controller (d). The air passes through the filter (b) and then through the granular medium inside the sample cell (a). The air pressure is measured before the filter (c).

tion speed of a paddle-like stirrer. We have sensors to read the air pressure before the bed, the normal force on the stirrer as well as the torque required to maintain rotation of the stirrer.

We will start by discussing the fluidization behavior of our samples.

### 3.4.1 FLUIDIZATION OF GRANULAR PACKINGS

For these experiments we operated the setup without stirrer. A sketch and photograph of the setup is shown in figure 3.1. Compressed air is first dried and the desired flow rate is set by a mass flow controller (d). The air passes through a glass frit acting as a filter (b). The air then passes through the granular medium inside the sample cell (a). The air pressure is measured before the filter (c). Details about the working principle of the components used are given in the appendix 3.7.1. In order to measure the pressure curve of the granular medium, we perform two measurements: one without granular medium that measures the resistance of the air system and a second measurement with granular medium in the sample cell. Every sample has a mass of $m_s = 270$g.

An example of such pressure curves can be seen in the inset of figure 3.2. Here, the gas velocity $u$ was calculated from the set gas flow rate $Q$ as $u = Q/A_T$ where $A_T$ is the
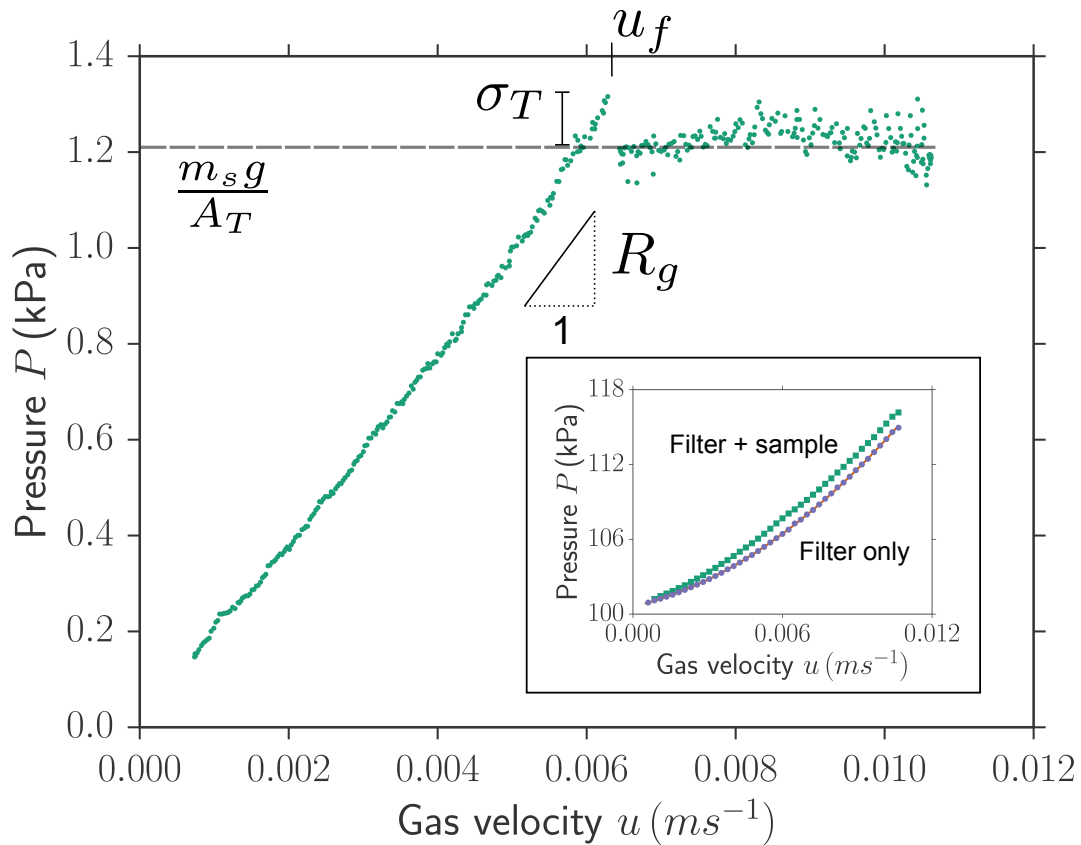
Figure 3.2: Pressure curve for granular sample (shown here: zirconia beads coated with graphite) without rheological measurement. The contribution of the granular medium is obtained by subtracting a measurement of sample and filter from a measurement of only the filter (see inset). Before fluidization, the pressure increases linearly with gas velocity where the slope is determined by the sample packing fraction and particle diameter. After fluidization, the pressure remains constant at the value determined by sample mass and tube cross section. An overshoot can be seen that increases with particle cohesion and can be interpreted as the material's tensile strength.

cross section of the tube. As such, the gas velocity is to be understood as an average over the total cross section, although the true local gas velocity will certainly have a distribution. If we now subtract the measurement of sample and filter from the measurement without sample, we can determine the contribution of the granular sample to the pressure curve (see fig. 3.2). The sample shown here are graphite coated zirconia beads. Before fluidization, the pressure increases linearly with gas velocity. In this regime, the granular packing is static and does not rearrange significantly. Therefore, the resistance for the gas will be a constant depending on the packing fraction, particle diameter and gas viscosity. As the gas velocity is increased, more and more load is taken off the contacts because some of the gravitational pull is reduced by hydrostatic lifting.

For flow rates beyond the fluidization gas velocity $u_f$, the contacts inside the granular medium are continuously broken and reformed. The air passes through the granular medium in bubbles. This is because the gas velocity is high enough to break the granular medium if it forms a dense packing but not so strong as to carry away individual particles. Increasing the gas flow rate further will increase the size and frequency of such bubbles, but does not lead to an increase of air pressure in front of the granular bed. The value that is reached in this regime will correspond to the gravitational pressure exerted by the sample of mass $m_s$ on the bottom of the tube with cross-sectional area $A_T$.

We see that right before the point of fluidization, the pressure increases beyond the gravitational pressure of the sample and then abruptly falls at the point of fluidization. The overshoot is the tensile strength of the granular material. We measure both the flow curve for increasing gas flow rate and then for decreasing gas flow rate without taking the air flow away in between. During the measurement with increasing flow rate, the granular sample starts in the static regime with permanent contacts which contribute to the tensile strength. During the measurement with decreasing flow rate, the same sample will start in the fluidized state without permanent contacts and will therefore not exhibit an overshoot. We determine the tensile strength as the maximum difference between the flow curve recorded for increasing flow rate and the flow curve recorded with decreasing flow rate. Details on the data analysis are given in the appendix in section 3.7.2.

We measured the tensile strength after filling the sample cell by pouring the zirconia beads. Fluidizing the sample and then letting it settle slowly did not produce a measurable tensile strength upon repeated fluidization. The measured tensile strength is visualized in figure 3.3. The argon-cleaned sample exhibited the smallest tensile
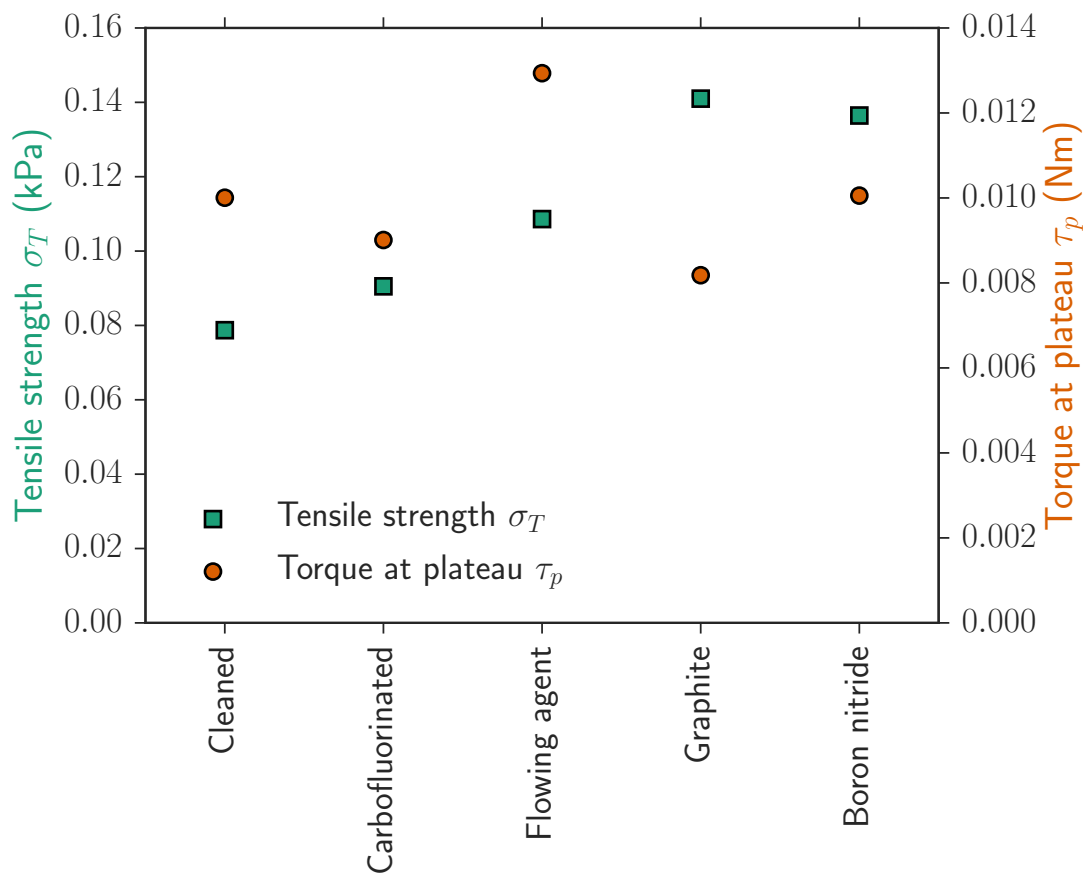
Figure 3.3: Measured tensile strength $\sigma_T$ and plateau torque $\tau_p$ for the different surface treatments.

strength while the graphite-coated sample exhibited the highest tensile strength.

### 3.4.2 RHEOLOGICAL MEASUREMENT OF UNFLUIDIZED GRANULAR PACKINGS

In this series of experiments, we shear the granular medium using a paddle-shaped intruder in a setup as pictured in figure 3.4. The intruder rotation rate can be set and normal force and torque acting on the intruder can be measured. The machine uses an optical encoder to measure deflection angle and calculates rotation speed from that. From the current needed to drive the motor, the torque on the stirrer can be calculated if it was beforehand calibrated by rotating in air. The device comes installed with translation factors to translate the torque into a shear stress and the rotation rate to a shear strain. We chose not to do so because in doing so we would have to make assumptions about the stress distribution inside the granular medium that we cannot measure. In a viscous liquid, the assumption is valid that the stress distribution is homogeneous. For a granular medium, formation of shear bands or force inhomogeneities violate such an assumption.

We start with a low rotation rate and increase that rate in logarithmically spaced steps so that we achieve a uniform point density on a plot with logarithmic rotation rate axis. After reaching the maximum rotation rate, we again decrease the rotation rate with the same recorded steps. The results we show are from the measurements with continuously decreasing rotation rate.

A measurement of torque as a function of rotation rate for each surface treatment is shown in figure 3.5. For rotation rates up to about $1\text{s}^{-1}$, the torque is mostly stable and we thus define $\tau_p$ as the average of all measured torques in the region from $10^{-3} - 10^{-1}\text{s}^{-1}$ for each sample. The plateau torque is sometimes also referred to as continuous yield limit. The value of $\tau_p$ changes measurably with surface treatment, where the sample with flowing agent exhibited the highest value and the graphite coated sample the lowest one.

We can now attempt to correlate the macroscopic flow properties to the microscopic measurements that were presented in chapter 2. For this, we plot $\sigma_T$ and $\tau_p$ as a function of static friction coefficient, particle-particle friction coefficient and contact angle. A graph of all possible combinations is shown in the appendix in figure 3.14. Of these combinations, only the ones shown in figure 3.6 produced reasonable agreement with a linear fit as indicated by a high coefficient of determination.
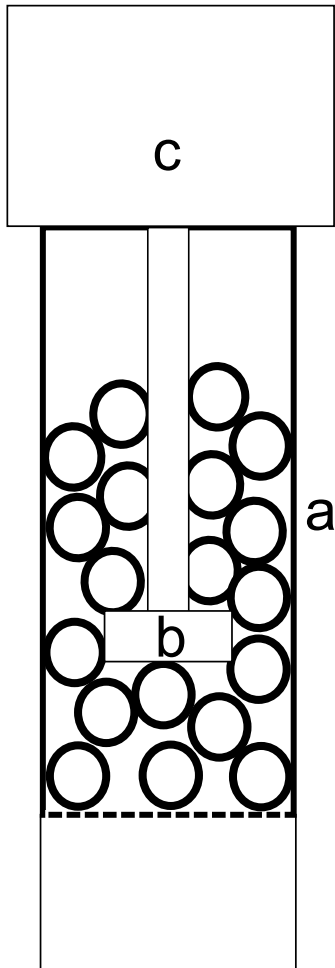
(a) Sketch of setup used for rheological measurement.

(b) Photograph of paddle intruder used in the rheological measurements.

Figure 3.4: Setup used to investigate rheological behavior of granular samples. The granular sample inside the powder cell (a) is sheared by an intruder (b and fig. 3.4b) which is controlled by a motor control unit (c).
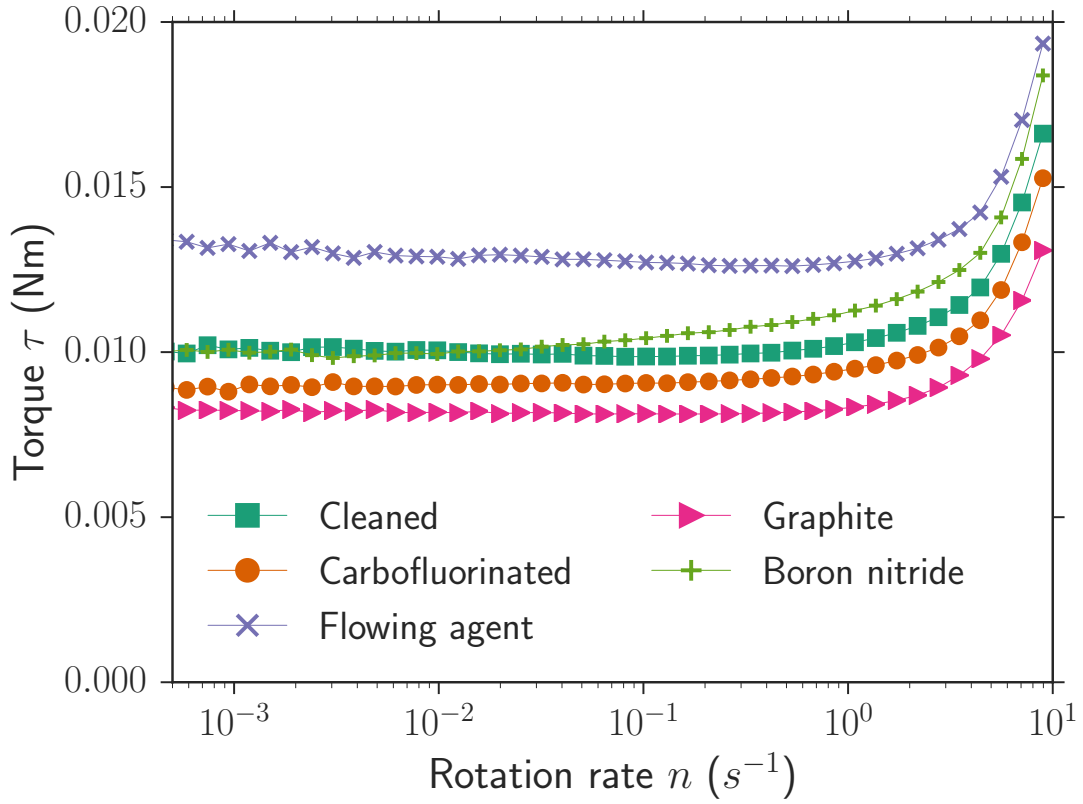
Figure 3.5: Measured torque as a function of rotation rate without gas flow for different surface treatments. The plateau torque $\tau_p$ depends on surface treatment where samples with flowing agent exhibit the highest while graphite coated samples exhibited the lowest value.

Table 3.1: Measured rheological quantities.

| Treatment | $u_f$(cm/s) | $\sigma_T$(Pa) | $\tau_p$(mNm) | $\beta$ | | | | |
|---|---|---|---|---|---|---|---|---|
| | | | | $u=0$ | $u=0.33u_f$ | $u=0.67u_f$ | $u=1u_f$ | $u=1.3u_f$ |
| Cleaned | 0.72 | 78.72 | 10.01 | 1.21 | 1.33 | 1.35 | 1.76 | 1.70 |
| Carbofluorinated | 0.7 | 90.51 | 9.01 | 1.24 | 1.54 | 1.48 | 1.60 | 1.72 |
| Flowing agent | 0.83 | 108.60 | 12.94 | 1.26 | 1.21 | 1.43 | 1.65 | 1.66 |
| Graphite | 0.61 | 140.99 | 8.18 | 1.43 | 2.03 | 2.01 | 1.67 | 1.78 |
| Boron nitride | 0.83 | 136.45 | 10.06 | 1.61 | 1.35 | 1.36 | 1.65 | 1.65 |
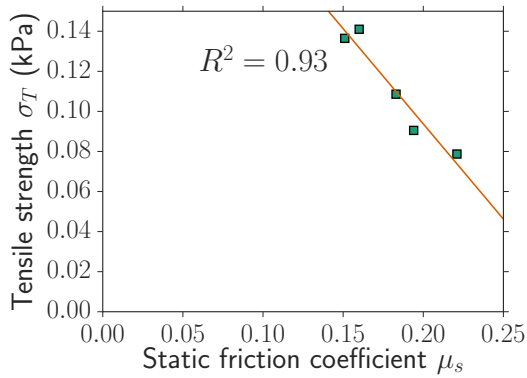
(a) Tensile strength of bulk material as measured in the fluidization experiments as a function of static friction coefficient as determined from inclined plane experiments against a smooth surface. For the tested samples the tensile strength decreases linearly with increasing friction coefficient.
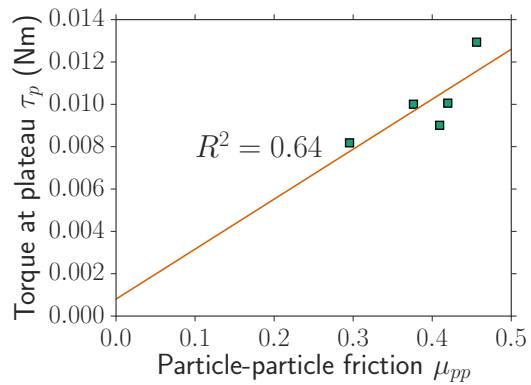
(b) Torque at plateau as determined from shear experiments with the paddle-shaped stirrer plotted against particle-particle friction coefficients. The plateau torque increases linearly with particle-particle friction.

Figure 3.6: Correlations found between microscopic parameters $\mu_s$ and $\mu_{pp}$ against macroscopic properties like $\sigma_T$ and $\tau_p$. Also shown is a linear fit to the data and the coefficient of determination $R^2$ of that fit. Other combinations like plotting $\sigma_T$ as a function of $\mu_{pp}$ or $\tau_p$ as a function of $\mu_s$ showed obvious lack of correlation with $R^2 < 0.3$.
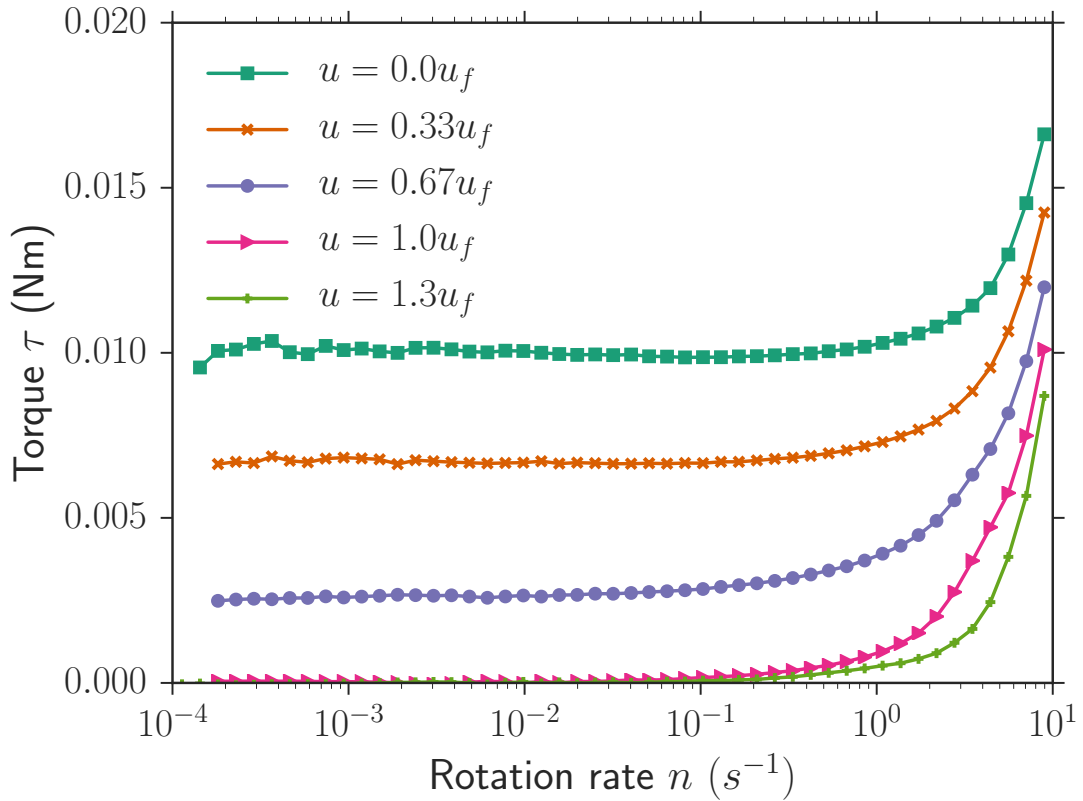
Figure 3.7: Measured torque at a set rotation rate for various gas velocities for the cleaned sample. For gas flow rates below fluidization, the torque needed to maintain rotation remains roughly constant up to a rotation rate of around $1s^{-1}$. This plateau torque $\tau_p$ reduces with increasing gas flow rate. For high rotation rates, the torque needed for rotation increases.

All the quantities determined in these measurements are also presented in table 3.1.

### 3.4.3 RHEOLOGICAL MEASUREMENTS WITH SIMULTANEOUS FLUIDIZATION

We measure the response to shear using the same protocol as in section 3.4.2 but we increase the gas velocity for each measurement. We write the gas velocity as a function of the fluidization gas velocity $u_f$ that we determine as the average of the fluidization velocity for all tested samples. The torque curves for the four tested gas velocities and the unfluidized experiment are shown in figure 3.7. The results displayed there are for the argon-cleaned sample but similar trends hold for all surface treatments.
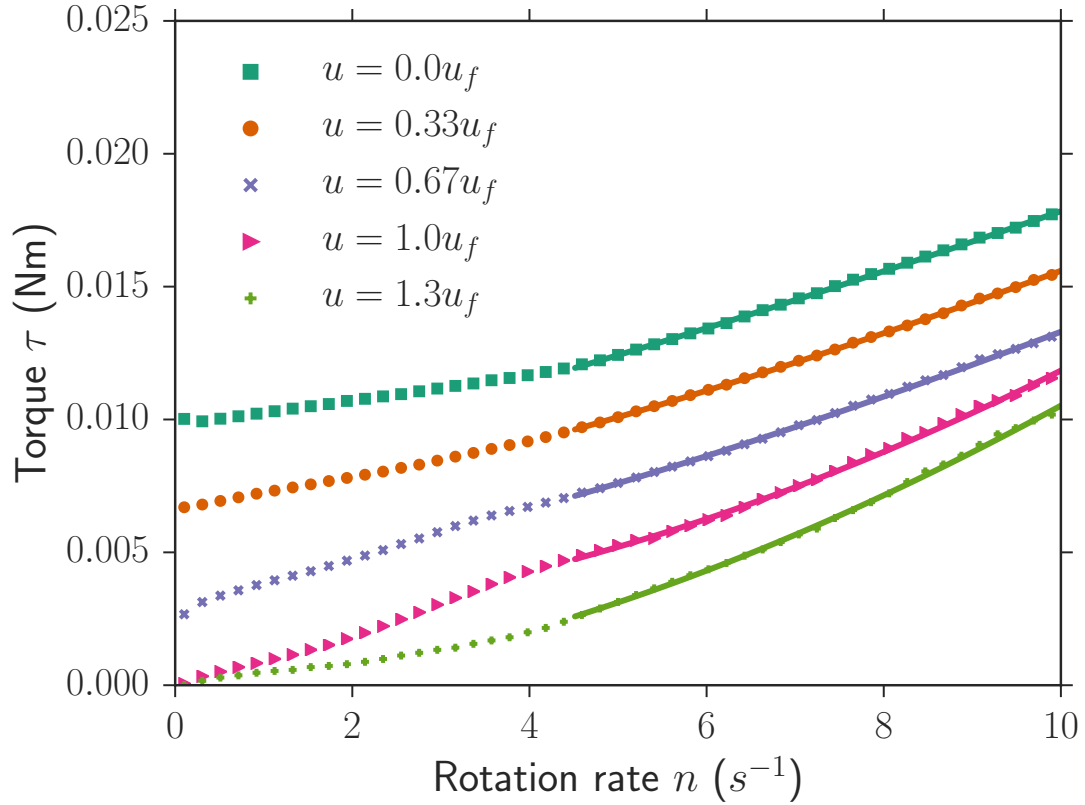
Figure 3.8: Torque against rotation rate for various gas velocities. We identify a high rotation rate regime beyond $4.5\mathrm{s}^{-1}$ where the torque increases smoothly. The solid lines are fits of the form $\tau(n) = a * n^\beta + c$ to the data in this regime from which we extract the exponent $\beta$.

We measure a linear decrease of the plateau torque $\tau_p$ with increasing gas velocity. Close to the point of fluidization and beyond, the plateau torque is close to zero in this rotation regime. For higher rotation rates, the torque increases.

The same plot as figure 3.7 is shown in figure 3.8 but with linear scaling on both axes. For rotation rates up to around $4\mathrm{s}^{-1}$ the slope appears to change if the gas velocity is close to fluidization. We therefore consider a high rotation rate regime beyond $4.5\mathrm{s}^{-1}$ where the scaling appears more stable and we determine the scaling by fitting an equation of the form

$$\tau(n) = an^\beta + c \qquad \text{(III–4)}$$

to the data. The fits are also shown in figure 3.8.

The exponent $\beta$ obtained from the fit is shown in figure 3.9 as a function of gas ve-
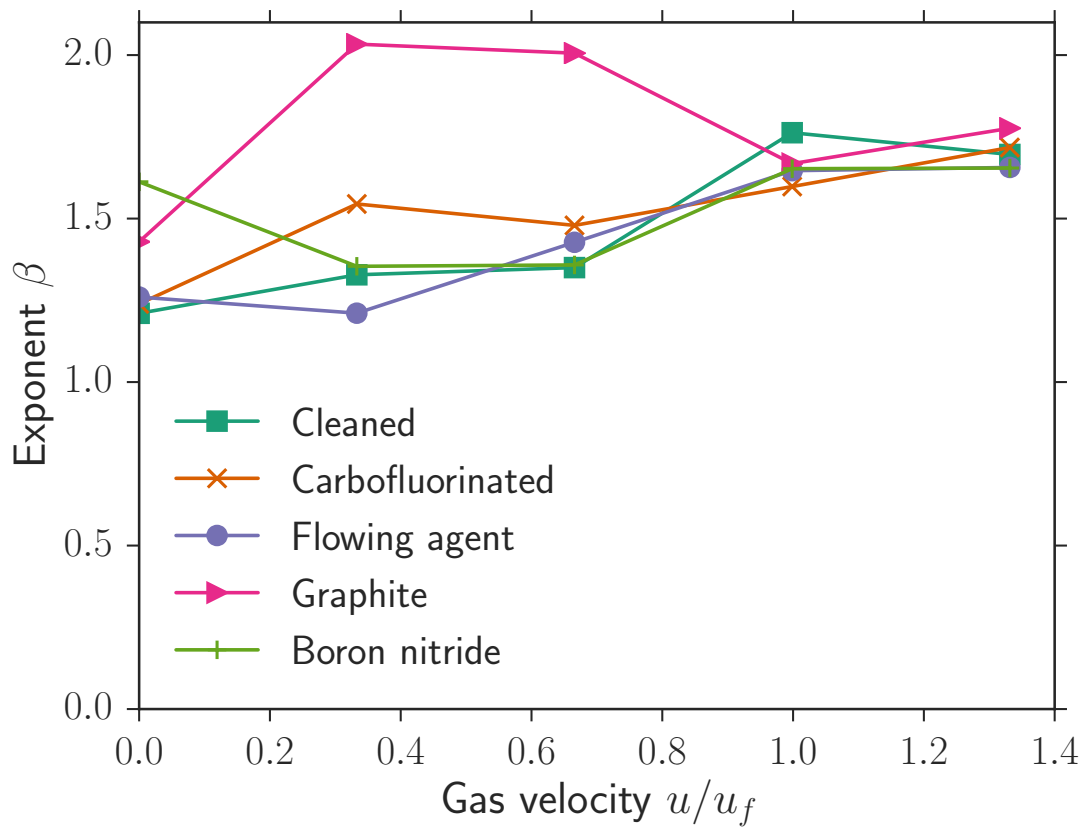
Figure 3.9: The exponent $\beta$ as a function of flow rate and surface treatment. For most surface treatments, $\beta$ increases from 1.2 to 1.8 as the flow rate is increased. Graphite coated samples exhibit an exponent $\beta$ of around 2 for low flow rates.
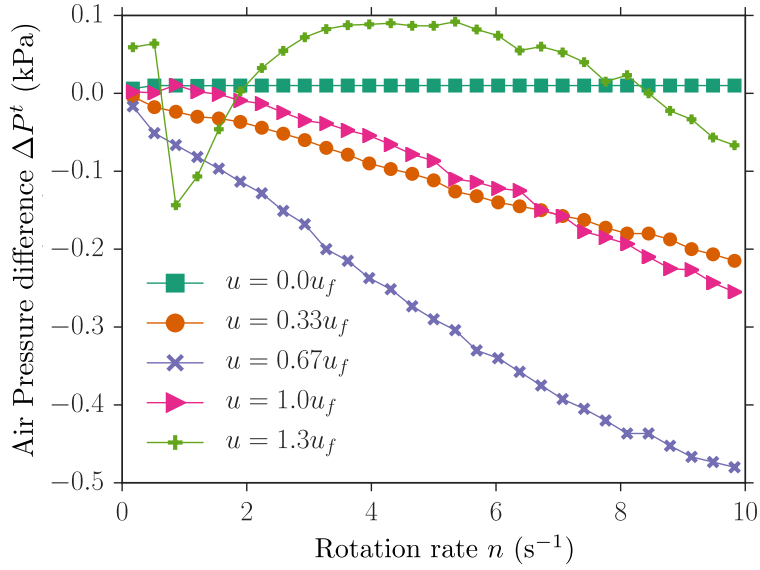
Figure 3.10: Evolution of measured air pressure difference as a function of rotation rate for the cleaned sample. We measure the absolute pressure at every point in time and obtain the pressure difference by subtracting from value measured at the start of the experiment. Therefore, the air pressure difference is $\Delta P^t = P(t) - P(t_0)$ where $t_0$ is the start of the experiment. For flow rates below fluidization the measured air pressure decreases as the rotation rate is increased. For gas velocities in the fully fluidized regime, the measured pressures fluctuate seemingly random.

locity for all surface treatments. For the argon cleaned sample, the exponent increases from about 1.3 to 1.7 after fluidization. This trend appears to be similar for all surface treatments. An exception to this is the graphite coated sample which exhibits an exponent $\beta$ very close to 2.0 for gas velocities lower than the fluidization velocity.

One interesting phenomenon we encountered during the course of these measurements is the decrease of measured gas pressure as a function of rotation rate for simultaneous fluidization and stirring of the samples. We define $\Delta P^t = P(t) - P(t_0)$ where $t_0$ is the start of the experiment and plot $\Delta P^t$ as a function of rotation rate as shown in figure 3.10. If no gas flow is applied, the air pressure does not change throughout the experiment. We measure that the air pressure decreases linearly with rotation rate if any gas flow is present and if the gas velocity is not in the fully fluidized regime. The downward slope increases going from $0.33u_f$ to $0.67u_f$ but at $1u_f$ the slope is again similar to the one of $0.33u_f$. In the fully fluidized regime, the pressure difference curve increases and decreases in a seemingly random way.
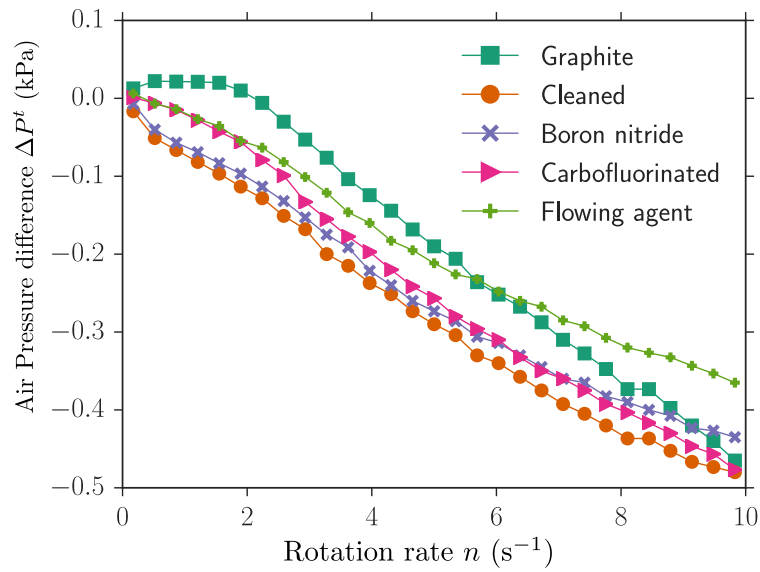
Figure 3.11: Measured air pressure difference as a function of rotation rate at a fixed gas velocity of $u = 0.67 u_f$ for different surface treatments. The pressure difference evolution is similar for all samples.

We have measured that this behavior is qualitatively the same for all surface treatments. The measurements for $u = 0.67 u_f$ for all surface treatments are shown in figure 3.11. The only noticeably different behavior is that for the graphite coated sample $\Delta P^t$ did not decrease immediately but instead started decreasing once a rotation speed of $2\mathrm{s}^{-1}$ was reached.

## 3.5 Discussion

We have measured the fluidization behavior and shear response of zirconia beads with surface treatments. From the fluidization measurements, we determine a tensile strength that was lower in the samples with a high coefficient of static friction. The tensile strength depends on the consolidation pressure of the sample which in our case only comes from the weight of the zirconia beads themselves. The fact that we only measure a tensile strength in samples that have been poured and then directly measured indicates that the tensile strength depends on the way in which the sample is allowed to settle. A granular packing with higher coefficients of friction is able to form mechanically stable packings at a lower packing fraction and with fewer contacts per particle than a packing without friction. Therefore, a possible explanation for a reduction of tensile strength with increasing static friction is that the samples with higher static friction form looser packings with fewer contacts. The tensile strength is a measure of the total cohesive energy stored in contacts and will therefore be lowered by a reduction in contacts.

An additional factor to consider is that the increase in friction will amplify the Janssen effect and thus lead to less average load on the contacts. Naively, one might think that friction will hinder fluidization and thus increase tensile strength because friction could be believed to prevent the motion at the contacts that is required to break apart the granular medium. However, this should not occur since at the point of fluidization the weight of the particles is compensated by the gas flow and therefore there is only little load acting on the contacts. One should therefore not expect an increase of tensile strength with friction coefficient in an identically prepared granular packing. Of course, correlation does not always mean causation and the changes in tensile strength could be due to some additional factors we did not consider or could not measure.

While shearing the samples, we measure a torque that remains constant for low rotation rates. This behavior can be explained by the formation of shear bands and has been described in the literature. We measure that this torque changes measurably when surface treatments are applied to the zirconia beads. A reasonable correlation has been found between the plateau torque and the particle-particle friction. After formation of a shear band, the resistance to shearing could come from spheres of one side of the band coming into frictional contact with spheres on the other side of the band. This is a possible explanation for why the torque required for stirring the sample would increase linearly with increasing particle-particle friction.

Despite the correlations that were found, some questions still remain. For example the

influence of charging in this experiment is difficult to estimate. We can see that after the experiment, there are some spheres stuck to the wall so we know that the spheres can attain enough charge from tribocharging to overcome gravity. Some options for limiting the effect of charging are to apply an electrically conducting coating to the walls which will reduce sticking of spheres to the walls. This is possible and comparing such experiments to the current one could serve to quantify the influence of particle-wall charging. However, it would not tell us anything about particle-particle charging. Alternative options are to add humidity to the gas stream so that the accumulated charges can be dissipated more easily but this would also increase the effect of liquid bridge formation. Finally, by conducting the experiment in a water fluidized bed the effect of charges is completely eliminated but now hydrodynamic interactions between the particles need to be considered.

We have measured that for high rotation rates, the torque scales with the rotation rate with a scaling exponent $\beta$ that is between 1.3 at low gas velocities and 2.0 at low friction and intermediate gas velocities. The scaling in the Bagnold regime would be expected to be 2.0 and the argument for this scaling is that an increase in rotation rate increases both the amount of collisions as well as the collision energies that are involved. Therefore the dissipated energy and in a rotation rate controlled experiment the energy that needs to be provided to maintain rotation scales with the square of the rotation rate. For those assumptions to be valid, the interactions between spheres needs to be dominated by collisions. This is not the case when the spheres are in contact most of the time such as when they are continuously pushed together by gravity. The gas flow will create a lift force on the spheres that will partly counteract gravity as we can see from the torque measurements. This explains why increased gas flows lead to a higher exponent because the assumption of being in a collision dominated regime is more likely to be fulfilled. The fact that the graphite coated sample which has the lowest particle-particle friction coefficient exhibited the highest scaling exponent $\beta$ can be argued in a similar manner. Friction will prevent spheres in loaded contact from moving and thus increase contact times. Therefore, a sample with low friction can be expected to enter the collision dominated regime sooner. Once the sample is fully fluidized, the difference between surface treatments diminishes because the contacts are no longer continuously loaded and therefore the influence of friction is reduced.

The reduction of gas pressure in front of the granular bed with increasing rotation rate is a phenomenon not to our knowledge described in the literature. To understand why this may be happening, we need to consider the air resistance of the granular medium which increases as the packing density increases. We measure a decrease of pressure

which means that the resistance of the granular medium is also decreased. Shearing granular media will locally increase density but also form shear bands with locally reduced densities. An inhomogeneity of densities could explain the decrease in air resistance even if the global packing fraction remains the same. A very simple model could be that shearing the granular medium will create one region of higher density and one region of lower density in a way that allows the air to pass through the sample using either the high density or low density path. Since the flow through the low density region will be greater, the effective resistance of the total medium will decrease. In addition, the granular medium in our cell is not confined at the top, so it is possible that the global packing fraction decreases by means of the granular medium expanding. Either way, this discovery could be combined with density sensitive measurements like diffusive wave spectroscopy or X-ray radiography to measure local densities and density inhomogeneities.

## 3.6 CONCLUSIONS

We have presented rheological measurements on fluidized granular samples with various surface treatments that influence friction, contact angle and triboelectric charging. We identified two measures that describe the flow behavior, namely the tensile strength of a granular sample settled under its own weight that we determine from fluidization experiments and the torque at low rotation speeds that we determine from rheological measurements. We find that the tensile strength decreases with increasing static friction of the particles. We additionally find that the torque at low rotation speeds increases with increasing particle-particle friction. We measure a transition to Bagnold scaling and that the scaling exponent is closest to Bagnold scaling in samples with low friction and intermediate gas velocities. We also find that the air pressure in front of the granular bed decreases when partly fluidized granular samples are sheared. This opens potentially new opportunities to measure density inhomogeneities in such systems.

# 3.7 APPENDIX

## 3.7.1 DETAILS REGARDING DEVICES USED

WORKING PRINCIPLE OF A MASS FLOW CONTROLLER    The rheometer is equipped
with a mass flow controller (MFC 8626 by Bürkert). One way to realize a mass flow
controller is shown in figure 3.12. A small portion of the gas stream (a) is redirected
into a bypass (b) where a heating element (c) is kept at a temperature $T$. The amount
of heat lost to the gas is proportional to the gas velocity and so the gas velocity can
be determined by measuring the current to the heating element required to maintain $T$.
The control system (d) compares the determined mass flow with the desired mass flow
and adjusts a magnetic valve (e) to set the correct mass flow.

WORKING PRINCIPLE OF AIR PRESSURE SENSOR    The air pressure in the rheometer
is measured with a piezoresistive transducer (Model 33X by Keller AG). To measure
the air pressure, a silicon membrane is deformed by the air pressure. The membrane
is piezoresistive, meaning that the resistance varies with applied strain. An auxiliary
electronics circuit measures the value of the resistance which can be converted to ob-
tain the air pressure.

## 3.7.2 DETAILS REGARDING THE DATA ANALYSIS PROCEDURE

DETERMINING CORRELATIONS WITH COEFFICIENT OF DETERMINATION    The co-
efficient of determination we use to quantify correlation is a special case of the Pear-
son correlation coefficient [80, 81]. If we experimentally observe a set of values $y$
with mean $\bar{y}$ as a function of $x$, the coefficient of determination of the linear fit which
produces values $\tilde{y}$ is given by:

$$R^2 = 1 - \frac{\sum_i (\tilde{y} - \bar{y})^2}{\sum_i (y_i - \bar{y})^2}. \tag{III–5}$$

$R^2$ essentially compares the model fit to a model which only uses the mean of the data
set. $R^2 = 1$ for perfect correlation and $R^2 = 0$ for independent quantities.

PROCEDURE TO DETERMINE TENSILE STRENGTH FROM FLUIDIZATION CURVES
There were three major difficulties we encountered when trying to determine the ten-
sile strength from the flow curves. The first problem is that the air pressure data
recorded by the rheometer contains outliers that have to be removed. We eliminate
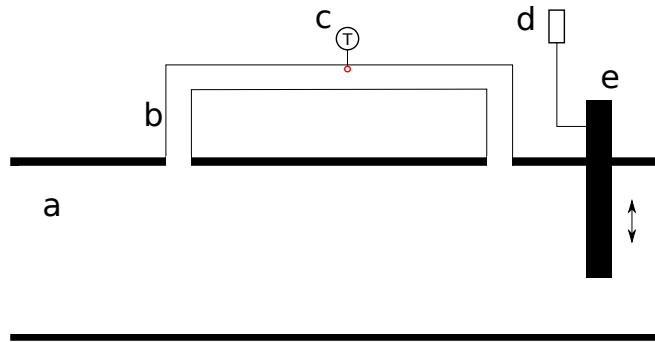
Figure 3.12: Schematic of working principle of a mass flow controller. From the main gas stream (a) a small fraction is rerouted into a bypass (b). A heating element (c) is brought to a specified temperature. The amount of heat dissipated to the gas flow will be proportional to the gas velocity. From the amount of power required to keep the heating element at a constant temperature, the control system (d) can determine the mass flow and adjust it by opening or closing a magnetic valve (e).

the outliers by applying a median filter to the pressure data. Alternative filters like a mean filter would not be suitable for this, because they are less efficient at removing single outliers and because they would average over the sharp edge encountered at the point of fluidization. The effectiveness of the median filter is shown in figure 3.13a where the data for the cleaned sample is shown. We highlighted an obvious outlier which is not present in the filtered data.

The second problem encountered is that the fluidization transition that takes the medium from static to the fluidized regime for some samples happened abruptly (see figure 3.2 for the flow curve of the graphite sample) and for other samples happens in multiple smaller steps (see figure 3.13a for the argon cleaned sample). This means that any approach based on determining the tensile strength as the greatest difference between neighboring measurement points would produce unreliable results for samples with a step wise fluidization transition. Instead we consider the tensile strength as the greatest difference between a granular sample with cohesive contacts and an identical sample without such contacts.

Ideally one would want to use the pressure value of the flow curve after fluidization. However, this introduces the third problem which is that the subtraction of the filter contribution as shown in the inset of figure 3.2 works with varying degrees of success. We identify problems in this area when there is a slope after fluidization in the flow curve of the granular medium. A slope in the flow curve after fluidization makes it unreliable to use the pressure in this region because it is varying for reasons not related
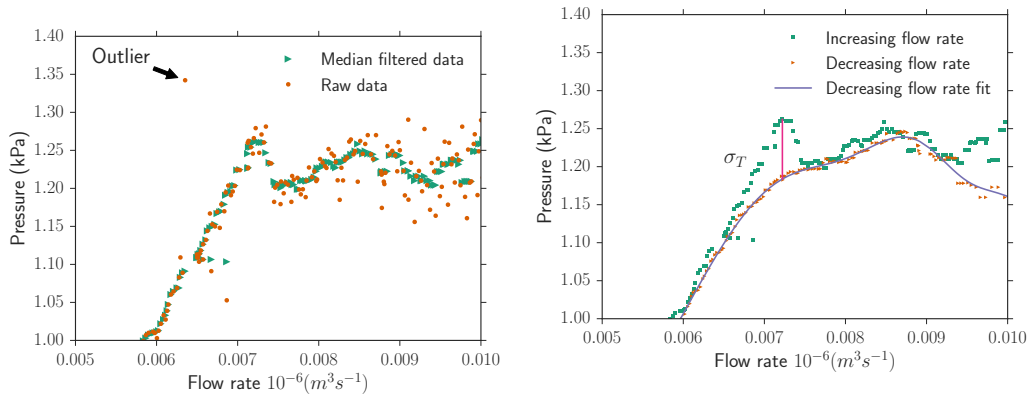
(a) Application of median filter to get rid of outliers in noisy data while preserving the sharp transition at the point of fluidization.

(b) The tensile strength is calculated as the maximum difference between the measurement with increasing flow rate an decreasing flow rate.

Figure 3.13: Data analysis steps required to reliably determine the tensile strength from flow curves.

to the granular sample.

We solve both the second and third problem by instead relying on the flow curve with decreasing flow rate where the sample is taken from a fluidized state to the static one. Since at the fluidization velocity, we measure here a forming of contacts rather than a breaking of contacts, the overshoot is not seen in the measurements with decreasing flow rate. We can therefore determine the tensile strength as the maximum difference between measurement with increasing flow rate and decreasing flow rate at the point of fluidization. The result of this procedure is shown in figure 3.13b. To be able to calculate a pressure value for every possible flow rate in the decreasing flow rate flow curve, we approximate this curve by a spline.

ALL GRAPHS RELATING MICROSCOPIC PARAMETERS TO MACROSCOPIC OBSERVABLES    In the following figure (3.14), we will show the macroscopic observables tensile strength and torque at plateau as a function of the microscopic parameters static friction coefficient, particle particle friction and contact angle.
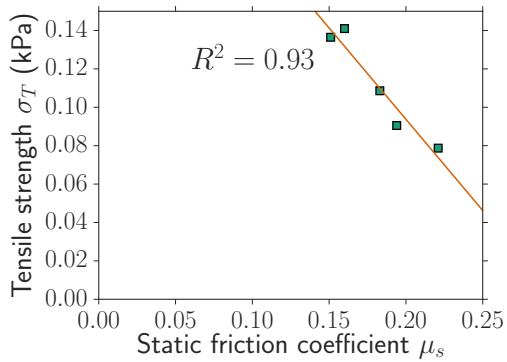
(a) Tensile strength of bulk material as measured in the fluidization experiments as a function of static friction coefficient.
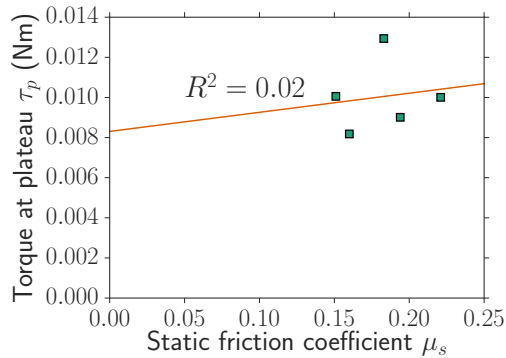
(b) Torque at plateau as determined from shear experiments with the paddle-shaped stirrer plotted against static friction.
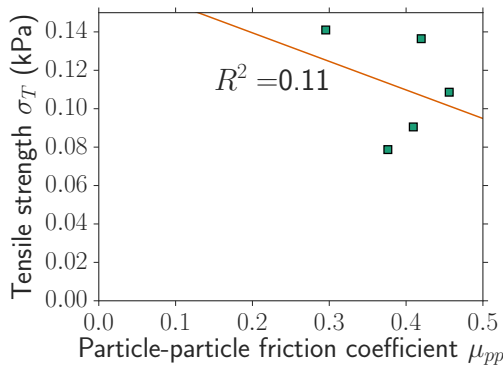
(c) Tensile strength of bulk material as measured in the fluidization experiments as a function of particle-particle friction.
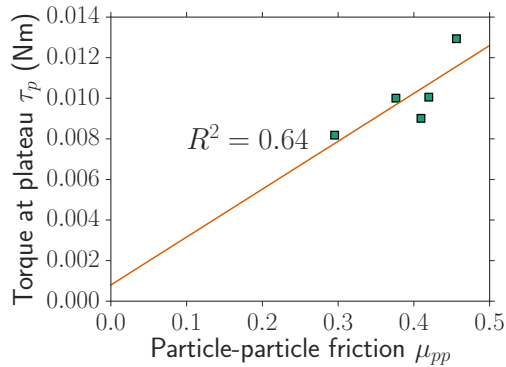
(d) Torque at plateau as determined from shear experiments with the paddle-shaped stirrer plotted against particle particle friction coefficients.
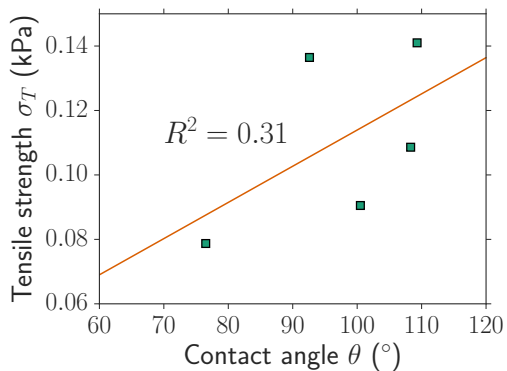
(e) Tensile strength of bulk material as measured in the fluidization experiments as a function of water contact angle.
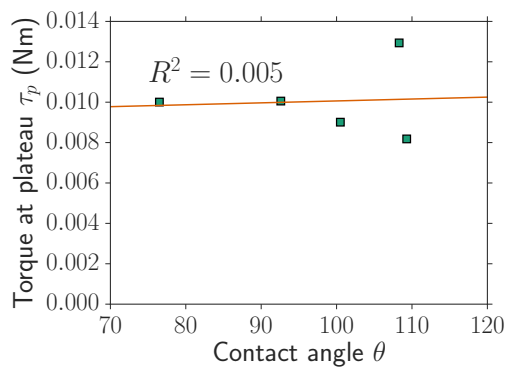
(f) Torque at plateau as determined from shear experiments with the paddle-shaped stirrer plotted against water contact angle.

Figure 3.14: Macroscopic parameters tensile strength and torque at plateau plotted against microscopic parameters static friction, particle-particle friction and water contact angle (see individual panel) with linear fits and coefficient of determination.

# Bibliography

[27]  D. Geldart. "Types of gas fluidization". *Powder Technology* 7.5 (May 1, 1973), pp. 285–292.

[28]  A. Castellanos, J. M. Valverde, A. T. Pérez, A. Ramos, and P. K. Watson. "Flow regimes in fine cohesive powders". *Physical review letters* 82.6 (1999), p. 1156.

[46]  T. Börzsönyi, T. C. Halsey, and R. E. Ecke. "Two Scenarios for Avalanche Dynamics in Inclined Granular Layers". *Physical Review Letters* 94.20 (May 25, 2005), p. 208001.

[63]  C. van Westen, T. van Asch, and R. Soeters. "Landslide hazard and risk zonation—why is it still so difficult?" *Bulletin of Engineering Geology and the Environment* 65.2 (May 1, 2006), pp. 167–184.

[64]  P. Jop, Y. Forterre, and O. Pouliquen. "A constitutive law for dense granular flows". *Nature* 441.7094 (June 2006), pp. 727–730.

[65]  H. Darcy. *Les fontaines publiques de la ville de Dijon: exposition et application...* Victor Dalmont, 1856.

[66]  P. C. Carman. "Fluid flow through granular beds". *Trans. Inst. Chem. Eng.* 15 (1937), pp. 150–166.

[67]  J. M. Valverde, A. Castellanos, A. Ramos, A. T. Pérez, M. A. Morgan, and P. Keith Watson. "An automated apparatus for measuring the tensile strength and compressibility of fine cohesive powders". *Review of Scientific Instruments* 71.7 (July 2000), pp. 2791–2795.

[68]  M. Schröter, D. I. Goldman, and H. L. Swinney. "Stationary state volume fluctuations in a granular medium". *Physical Review E* 71.3 (Mar. 30, 2005).

[69]  R. A. Bagnold. "Experiments on a gravity-free dispersion of large solid spheres in a Newtonian fluid under shear". *Proc. R. Soc. Lond. A* 225.1160 (Aug. 6, 1954), pp. 49–63.

[70]  C. S. Campbell. "Rapid Granular Flows". *Annual Review of Fluid Mechanics* 22.1 (Jan. 1, 1990), pp. 57–90.

[71]  I. Goldhirsch. "Rapid granular flows". *Annual review of fluid mechanics* 35.1 (2003), pp. 267–293.

[72] Y. Forterre and O. Pouliquen. "Flows of Dense Granular Media". *Annual Review of Fluid Mechanics* 40.1 (2008), pp. 1–24.

[73] W. T. Kranz, F. Frahsa, A. Zippelius, M. Fuchs, and M. Sperl. "Rheology of Inelastic Hard Spheres at Finite Density and Shear Rate". *Physical Review Letters* 121.14 (Oct. 2, 2018), p. 148002.

[74] T. Kawasaki, A. Ikeda, and L. Berthier. "Thinning or thickening? Multiple rheological regimes in dense suspensions of soft particles". *EPL (Europhysics Letters)* 107.2 (2014), p. 28009.

[75] R. M. Nedderman. *Statics and kinematics of granular materials*. Cambridge University Press, 2005.

[76] A. Fall, A. Lemaître, F. Bertrand, D. Bonn, and G. Ovarlez. "Shear Thickening and Migration in Granular Suspensions". *Physical Review Letters* 105.26 (Dec. 22, 2010).

[77] I. R. Peters, S. Majumdar, and H. M. Jaeger. "Direct observation of dynamic shear jamming in dense suspensions". *Nature* 532.7598 (Apr. 2016), pp. 214–217.

[78] F. Rietz, C. Radin, H. L. Swinney, and M. Schröter. "Nucleation in Sheared Granular Matter". *Physical Review Letters* 120.5 (Feb. 2, 2018), p. 055701.

[79] L. Bocquet, W. Losert, D. Schalk, T. C. Lubensky, and J. P. Gollub. "Granular shear flow dynamics and forces: Experiment and continuum theory". *Physical Review E* 65.1 (Dec. 21, 2001).

[80] F. Galton. "Regression towards mediocrity in hereditary stature." *The Journal of the Anthropological Institute of Great Britain and Ireland* 15 (1886), pp. 246–263.

[81] K. Pearson. "Note on regression and inheritance in the case of two parents". *Proceedings of the Royal Society of London* 58 (1895), pp. 240–242.

# 4 DOUBLE ORIGIN OF STOCHASTIC GRANULAR TRIBOCHARGING

Results published in:

Haeberle J, Schella A., Sperl M., Schröter M., & Born P. (2018). Double origin of stochastic granular tribocharging. Soft Matter, 14, 4987-4995.

In addition to the results already published, we present here the influence of surface treatments on the tribocharging distribution and provide additional details regarding the electron transfer model, the devices used in the experiments and the silanization technique used for the surface treatments as well as a detailed calculation of the Hertzian contact area in the single collision experiment.

The mechanisms underlying triboelectric charging have a stochastic nature. We investigate how this randomness affects the distributions of charges generated on granular particles during either a single or many collisions. The charge distributions we find in our experiments are more heavy-tailed than normal distributions with an exponential decay of the probability, they are asymmetric, and exhibit charges of both signs. Moreover, we find a linear correlation between the width and mean of these distributions. We rationalize these findings with a model for triboelectric charging which combines stochastic charge separation during contact and stochastic charge recombination after separation of the surfaces. Our results further imply that subsequent charging events are not statistically independent.

## 4.1 INTRODUCTION

Forming and breaking of contacts among solid bodies is intrinsically connected to generation of electrostatic charge [82–84]. This contact- or triboelectric charging has many spectacular manifestations in granular media, among which are flashes in volcano plumes [17, 18], lightnings in sand storms [19] and self-ignition of dust explosions [85, 86]. Triboelectric charging in granular media has also found technical implementations as in photocopying [87], electrostatic powder coating [88] or electrostatic dust removal [89–91]. Despite the widespread occurrence of triboelectric charging, no generally accepted theoretical framework has been developed for all these effects.

Experimental evidence suggests that the charge separation occurs by a wealth of mechanisms, out of which individual mechanisms may prevail under certain circumstances [12–14], and quantitative predictions seem to be out of reach [92, 93].

A joint feature of the mechanisms proposed to build up and dissipate static charging is their stochastic nature (see discussion in sec. 4.2). Here we focus on this stochastic nature of triboelectric charging of dielectric particles. Knowing the characteristics of the probability distribution of the charges is of interest in various situations. The probability of igniting a spark depends on the probability of accumulating an extreme charge in a contact between particles, while the efficiency of coating processes and dust removal may be better derived from the average charge of the particles. Correct modeling of particle interaction depends on the whole range of accessible charges.

In this work, we study the probability distribution of triboelectric charging in both single collision experiments and for many subsequent collisions (see sec. 4.3). We find asymmetric, exponential-tailed distributions which range from positive to negative charges as a common feature in all our experiments. Additionally, the experimental results imply that subsequent charging events are not statistically independent and that the mean and the width of the charge distributions are linearly correlated.

These results motivated a search for a common underlying stochastic mechanisms. In section 4.4 we suggest a model for the probability distribution of triboelectric charges based on the two stochastic triboelectric processes, charge separation and charge dissipation. The model reproduces the general features of our measured charge distributions which suggests that charging and discharging are equally relevant for understanding triboelectricity.

## 4.2  MECHANISMS OF TRIBOELECTRICITY

The charge build-up upon breakage of contact of solid bodies is often described in a first approximation as a material property. This may be motivated by the well-understood contact charging of metals, where charge build-up can be predicted by the work functions of the materials [94, 95]. We provide a more thorough description of this model in the appendix in section 4.7.1. Based on this material-focused view, triboelectric series, which rank the affinity of a material to charge positively or negatively after a contact [82], have been developed for a number of materials including insulators.

However, inconsistencies among different reported triboelectric series can be found

repeatedly [96–98]. This problem motivated the search for further parameters relevant to charge separation. Experiments identified, among others, hydrophobicity [55, 99], humidity [100–102], temperature [103], strain [104], particle size [9, 12], impact velocity and angle [15, 102, 105] and particle shape and contact mode [106–108] as relevant parameters influencing triboelectric charging.

Four mechanisms are presently discussed to fundamentally cause charge separation in contacts of insulators. One mechanism is the exchange of electrons trapped in localized states within the band gap of the insulators [94, 95, 109]. Electrons can relax from such excited trapped states near the surface of one body into states in the valence band of another body in contact, such that a net charge remains after separation of the bodies. The energy levels and the frequency of these trapped states are randomly distributed [109], and an additional probability for a relaxation process has to be taken into account. It should be pointed out that recent work has questioned the generality of the trapped states model [12].

Another mechanism that separates charges is the exchange of mobile ions and ion exchange through a medium. If mobile ions are present on the surfaces in contact, the concentrations will equilibrate by thermal motion, and the amount of charge exchanged correlates directly to the surface density of separable surface groups [10, 98, 99]. Alternative models exist for surfaces without separable surface molecules, which rely on aqueous ions in surface water films [55, 101] or in the atmosphere [13].

Third, charging by transfer of material was observed for contacts involving polymers [11, 92, 110, 111]. In such experiments, polymers were pressed into contact and material transfer can be verified in addition to charge transfer. Imaging the surfaces after separation with Kelvin Force Microscopy revealed a mosaic of positively and negatively charged microscopic spots [92]; the total net charge thus is the sum over many independent charge transfers.

Finally, the importance of polarization in generation of charge in granular media has been highlighted [14, 112]. The charge separated in a contact depends on the field generated by all charges present in the surrounding, and minute initial charge on one of the surfaces may be amplified.

The relevance of each of these four mechanisms, which may occur simultaneously in a single contact, and the extent of triboelectric charging during a contact will depend on the materials in contact and the aforementioned additionally relevant parameters and environmental conditions. The present knowledge of these mechanisms has been reviewed by several authors [10, 11, 113–115].

Common to these four mechanisms is a *stochastic microscopic process.* The polar-

ization mechanism may amplify some a priori unknown charge, but the electric field at the point of contact depends on a surrounding unknown charge landscape which justifies to assume a random electric field at the point of the contact zone. Also the microscopic processes at the contact of two bodies underlying the first three mechanisms can be modeled by two random surface distributions of donor and acceptor sites being pressed together [116], where the donors and acceptors may represent trapped and valence band states, concentrations of separable surface groups, or concentrations of transferable polymer chains. Following this model, charge transfer is proportional to the overlap between acceptor and donor sites. The transferred net charge turns into a sum over random overlaps, and can be expected to be normally distributed in the central limit [116].

A second group of studies has focused on the recombination of charges after the separation of the surfaces. The importance of the recombination and discharging of the surfaces to the full understanding of tribocharging has been discussed for long [117]. After all, discharging in spectacular sparks or lightnings is one of the most obvious manifestations of massive tribocharging.

Careful experiments have shown that even a single, nanoscale contact is followed by several discharging events [118, 119]. This can be understood by the fact that due to the limited surface conductivity a single discharging event cannot recombine the whole charge separated during the contact [86, 120]. The superposition of the many discharging events then becomes similar to the discharging of a capacitor [86, 121]. Moreover, experimentally observed decay times of triboelectric charges of tens of microseconds [86] are comparable to estimated contact times for Hertzian collisions [31], suggesting that contact mechanics limit discharging times.

Several mechanisms can be responsible for the individual discharge events, such as dark, glow and spark discharge [122]. Discharge by a spark discharge may cause the upper limit for the charge an insulator particle can carry after a collision [10, 15, 105]. This threshold charge required to ignite a spark can be derived from Paschen's law [123].

Which discharge mechanism will occur depends on parameters such as electric field strength, surface geometry, dielectric breakdown strength and separation velocity. However, all of these discharging processes through a gas have stochastic contributions like the probabilistic presence of ions formed by background radiation or illumination, stochastic collisional ionization of gas molecules and erratic path finding of streamers and sparks[124, 125]. In consequence, the realized conductance and the time the discharging persists will change stochastically.

If the contact involves granular particles, additional parameters such as surface roughness, particle shape variations or rotary particle motion will result in strong fluctuations of factors such as surface geometry and separation velocity. The net attenuation given by conductance and contact mechanics thus can be expected to be a random variable.

We conclude that both the mechanisms associated with triboelectric charging and subsequent discharging are of stochastic nature. The statistics of both charging and discharging and the combined effect have rarely been discussed. Fluctuations of the net charge of individual particles have been observed in previous studies [10, 12, 126–128]. In one of these studies a non-normal distribution of the generated charge is reported [10]. This nontrivial property motivates a closer investigation of the charge distribution and the relation to the two underlying mechanisms.

## 4.3 EXPERIMENTAL METHODS AND RESULTS

Stochastic triboelectric charging implies fluctuations of the charge on granular particles generated in identical configurations. We quantify this by repeated measurements of the charge generated in a single contact or during multiple collisions of a granular particle. A key aspect of our experiment is the minimization of charges generated during handling of the particles prior to the single contact measurement. Handling is inevitably connected to forming and breaking of contacts and as such creates charges on the particles which will be superimposed to the charge generated in the contact to be tested. Another elegant approach to minimize charging during handling is presented in a recent study, where the particles are levitated in an acoustic levitator prior to contact charging [99].

### 4.3.1 SINGLE CONTACTS

A schematic of the measurement setup is shown in the inset of Figure 4.1. Spherical particles (soda-lime glass beads, 4 mm diameter) are released from the reservoir one at a time through use of a particle dispenser (a). The dispenser picks particles by rotating a wheel with dimples below the reservoir. The particles are released from the dimples with rotation of the dispenser wheel and fall an identical distance of 300 mm. The particles are discharged while passing through ionized air with positive and negative ions created by an ionization needle (Haug OPI) (b). While the kinetic energy of the particles is given by their falling height, the release from the dispenser wheel imparts them with an additional unknown rotational component. The particles hit a collision target at an angle of $60°$ (grounded copper slab or polytetrafluoroethylene (PTFE) slab,(c)) and fall into the Faraday cup (d) where their charge is measured using a Keithley 6514 electrometer.

The electrometer measures continuously the charge accumulated by the Faraday cup. The particles falling into the cup led to equidistant changes in the charge (see exemplary charge curve in Fig. 4.1). As can be seen from the highlighted examples (I, II, III), the charges accumulated during the collision by the glass beads can vary orders of magnitude and also in their sign. The charge distribution $P(Q_n)$ of the net particle charges $Q_n$ is determined by counting each change of charge above a threshold of 0.1 pC. This threshold is necessary to take the drift of the electrometer into account.

All particles used in our experiments are first rinsed with water and ethanol and then cleaned in an Argon plasma for 10 min (Diener electronic Femto plasma cleaner).
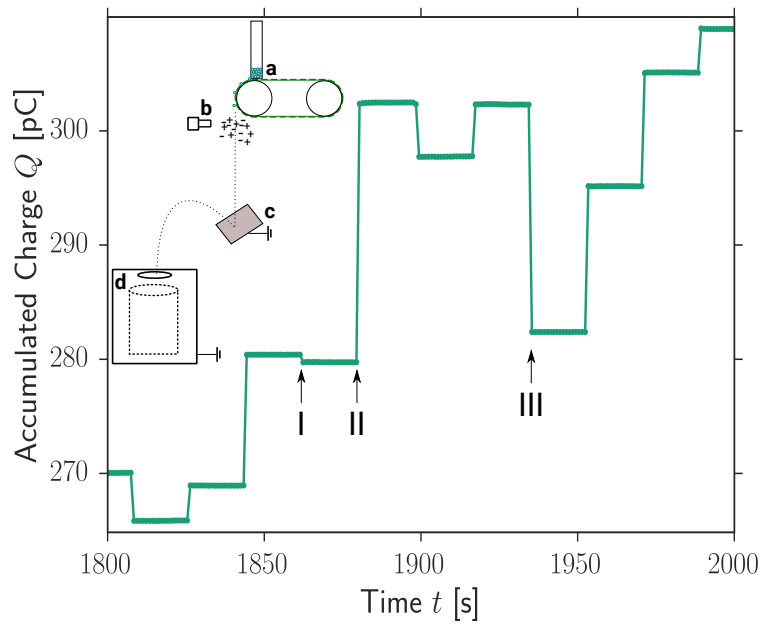
Figure 4.1: Detail of the charge measurements, here glass beads bouncing off a PTFE slab. Each particle dropping into the Faraday cup causes a change in charge accumulated in the Faraday cup, resulting in a jump of the curve. Steps I, II, and III exemplify the large variability in magnitude and sign of the charge on the particles. The inset shows the measurement setup, with the particle dispenser (a) dropping individual particles through a charge-neutralizing cloud of ionized air created by an ionization needle (b) onto a collision target (c). The particles bounce after a single collision into a Faraday cup inside of grounded conductive housing (d).
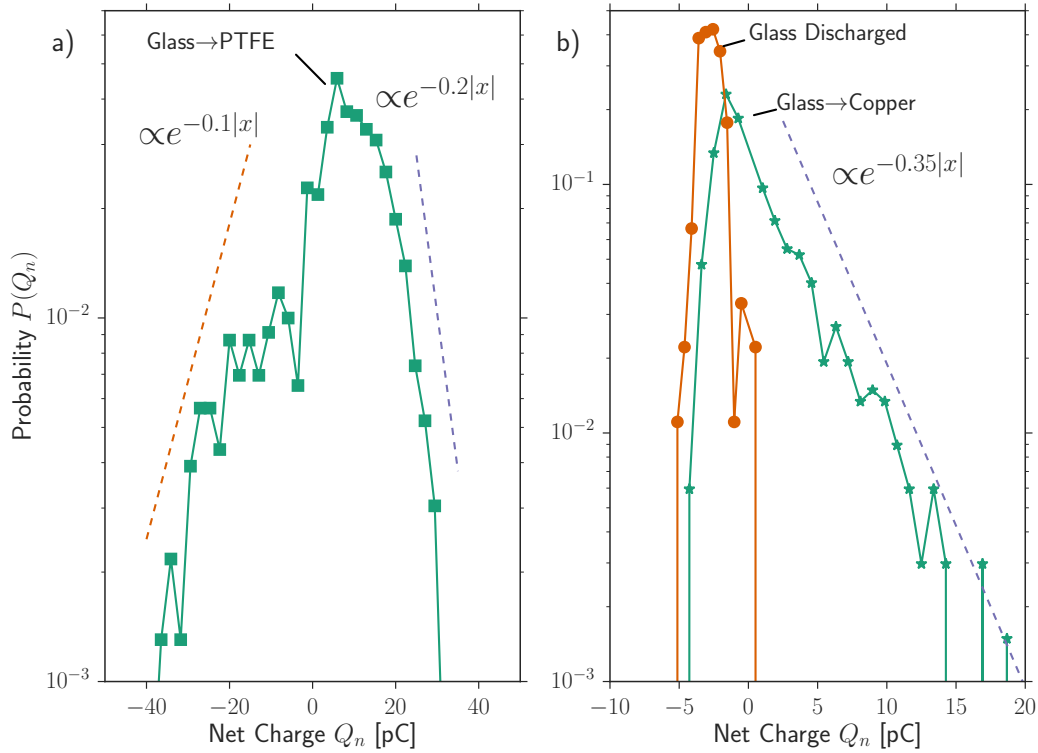
Figure 4.2: Probability distribution for charges accumulated in single collisions of Glass beads with a PTFE slab (a) and of Glass beads with a Copper slab (b). The dashed lines act as a guide to the eye and show the slope of the exponential decay of the tails. Also shown in (b) is the distribution of charges on the particles after passing the ionization needle without colliding with a target.

Between 500 to 1500 particles were dropped for each measurement, the exact numbers can be found in table 4.1.

In order to identify our background, we first measure the charge distribution of spheres which have not collided with a target, i.e. dropped directly into the Faraday cup. Without the ionization needle, these particles accumulate between 100 pc and 1 nC on their surface. After including the ionization needle in the setup, the residual charge is reduced to a narrow distribution between 1 pC and -5 pC with a mean of -2.65 pC; this distribution is shown in figure 4.2, b.

Introducing now a collision target in the path of the particles changes the charge measured on the particles (see Fig. 4.2). Instead of gathering a fixed amount of charge during the collision, the particle charge becomes wider distributed, with a strong dependency on the collision target material. The particles accumulate a mean charge of

4.12 pC in the case of of glass beads bouncing off a PTFE slab (Fig. 4.2, a), while after collision with copper a mean charge of 0.90 pC is accumulated (Fig. 4.2, b). The distributions are asymmetric, with a skewness of -1.16 (PTFE) / 1.89 (Copper), and are fat-tailed with an excess kurtosis of 1.63 (PTFE) / 5.20 (Copper). The tails of the distributions decay approximately exponentially. Noteworthy is the pronounced presence of charges of both signs.

An average charge densities of about $100 e^-/\mu m^2$ for both cases can be estimated from the mean net charge on the particles of 0.90 pC (Copper) / 4.12 pC (PTFE), assuming a Hertzian contact among a sphere and a flat surface [31] and taking into account a falling height of 30 cm. A detailed calculation is presented in the appendix section 4.7.4. The charge density is comparable to previous studies on triboelectricity, where numbers of $300 e^-/\mu m^2$ [84] or $500 e^-/\mu m^2$ [98] are reported. However much higher charge densities above $1200 e^-/\mu m^2$, more than ten times the mean, occurred on 3.5% of the spheres, exemplifying the effect of skewness and fat-tailedness of the measured distributions.

### 4.3.2 MULTIPLE CONTACTS

In a second series of experiments we replace the large glass spheres by smaller spheres with 500-560 $\mu$m diameter; these particles are made of either soda lime glass (Worf Glaskugeln GmbH) or polystyrene (Spheromers CS 500, Microbeads) and were cleaned as before. In one experiment, the soda lime glass beads were surface treated to attain PTFE-like properties. With these small spheres a charge neutralization down to a residual background charge between -0.1 pC and +0.1 pC is achieved, a much better value than for the larger spheres. The collision targets are replaced by tubes oriented at a 45° angle, such that the particles perform many contacts inside the tube before falling into the Faraday cup (see inset Fig. 4.3). Some experiments are performed inside of a climate chamber to test the influence of ambient conditions such as the relative air humidity (RH).

This setup allows us to test how the charge distribution changes as a function of the average number of contacts a particle experiences. For this purpose we vary the length of the polymethyl methacrylate (PMMA). We note that the contact mode, the ratio of normal and tangential component in a contact, may change along with the number of contacts. The resulting charge distributions are shown in Fig. 4.3. The number of contacts will grow systematically with tube length, but also the ratio of tangential to normal force component in each contact will change along the tube. The measured
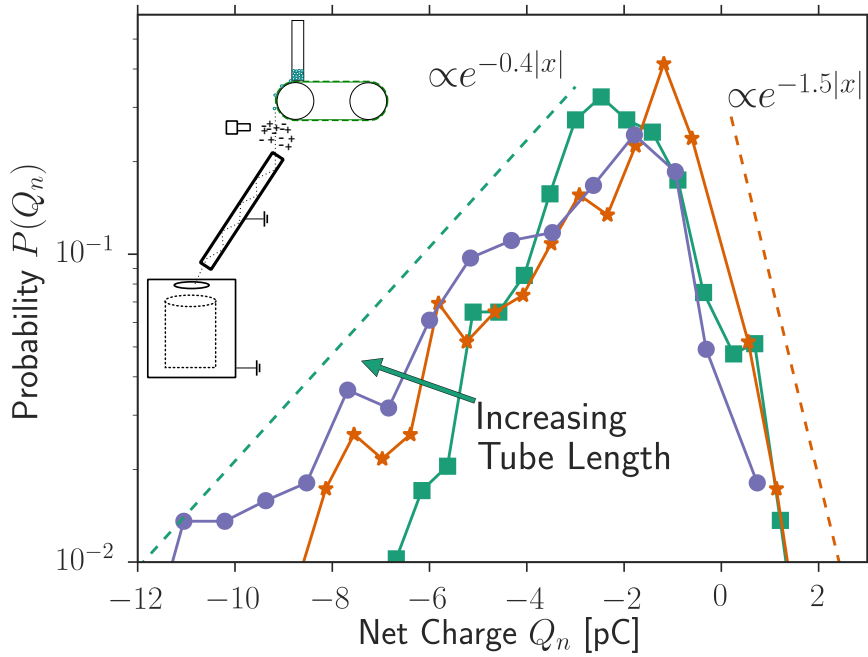
Figure 4.3: Probability distributions for charges accumulated by individual glass beads bouncing down inclined PMMA tubes with lengths of 20 cm, 80 cm, and 100 cm (as indicated by the arrow). The dashed lines are guides to the eye and highlight the approximately exponential tails of the distributions. Several key features like the asymmetry and the approximately exponential decay of the probability distributions do not change with number of collisions. The inset shows the measuring setup for multiple collision measurements.
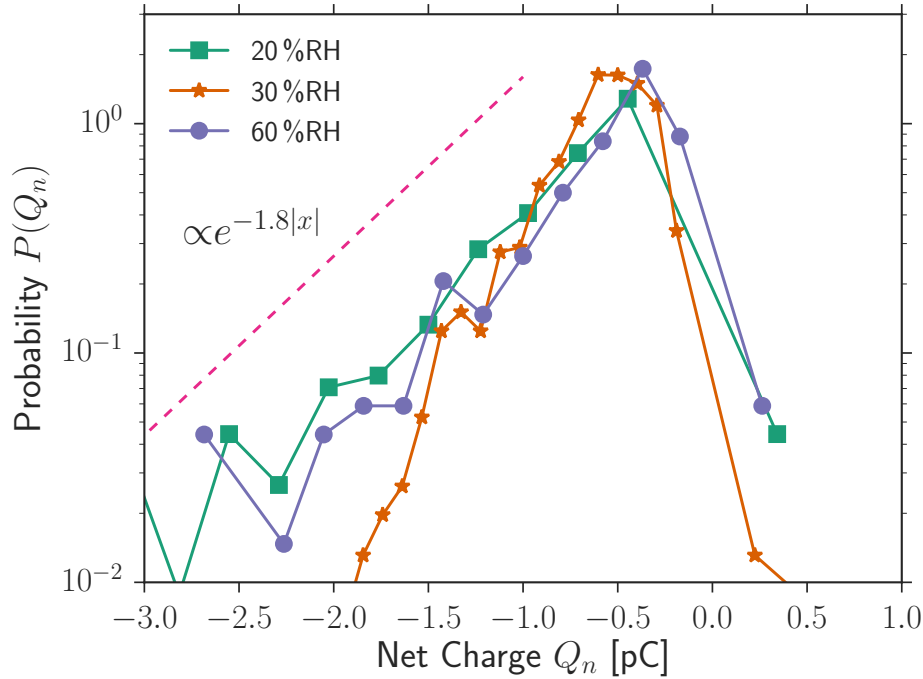
Figure 4.4: The charge distributions of glass beads bouncing down a stainless steel tube of 40 cm length, measured at different relative air humidities (RH). The distributions show no systematic trend with the relative humidity. Again we observe wide, asymmetric distributions.

average charge grows with tube length (from -2.37 pC to -3.55 pC), accompanied by an increasing negative skew (from -0.34 to -1.38). The features mentioned for the charge distributions measured after a single contact also hold for multiple contacts. All distributions possess approximately exponential tails and a strong asymmetry and have a positive excess kurtosis (from 0.72 to 1.96).

Because environmental conditions influence triboelectricity, we perform additional experiments where we vary the relative air humidity using the climate chamber described in [55]. The samples and the setup are kept at constant conditions for at least half an hour before the start of the measurements. The variation in relative humidity during the measurement time is smaller than $\pm$ 8%RH. The charge distributions measured at 20 %, 30 %, and 60 %RH are displayed in Fig. 4.4. Again we observe wide, asymmetric distributions irrespective of ambient humidity; the mean values, skew, and kurtosis are listed in table 4.1. A decrease of the mean charge with relative humidity can be observed. We also observe an enhanced drift of the charge measurements at higher humidities, similar to previous studies [13]. This effect prevents charge mea-
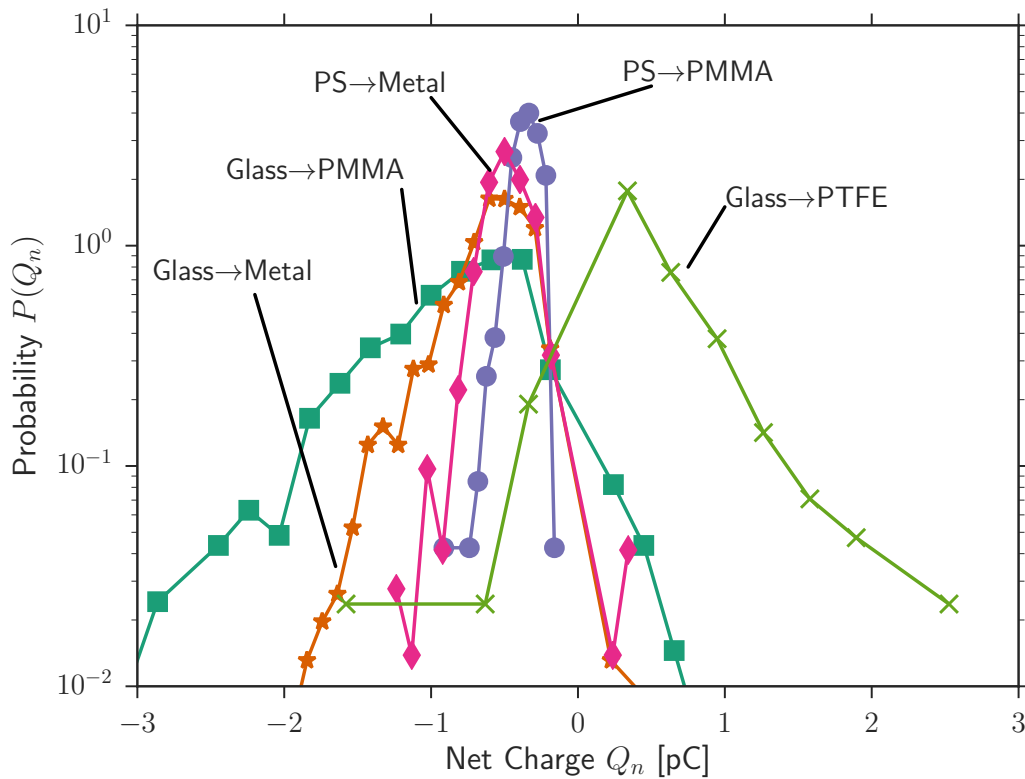
Figure 4.5: Probability distributions for the charges accumulated by individual particles bouncing down tubes made of different material. The particle materials glass and PS were combined with tube materials of PMMA, grounded stainless steel and PTFE. The general appearance of the distributions does not depend on the specific material combination, all combinations lead to sharp, fat-tailed distributions with an excess kurtosis ranging from 2.03 to 4.69.

surements above 60 %RH.

In order to test how generic the above described features of the charge distributions are, we tested a number of additional material combinations using both glass and polystyrene (PS) spheres, and tubes made either from PMMA, grounded stainless steel, or PTFE. The resulting charge distributions are displayed in Fig. 4.5. All distributions are asymmetric with skew values with the same sign as the mean. And they are fat-tailed with an excess kurtosis ranging from 2.03 to 4.69. Thus the characteristic shape of the distributions obtained in the previous measurements is preserved, although the average charge varies from -0.87 pC (glass against PMMA) to 0.52 pC (glass against PTFE). We also considered studying same-material tribocharging using 0.5 mm PMMA spheres in the PMMA tube. The achieved charges were typically less

than 0.1 pC, not enough to be reliably measured.

We have performed experiments where spheres are treated with 1H,1H,2H,2H-Per-fluorodecyltrimethoxysilane (PTMS, purchased from Sigma Aldrich) which creates a mono layer of fully fluorinated carbon chains on the surface of the glass beads. Details about the treatment process can be found in the appendix 4.7. The fluorinated carbon chains are chemically similar to PTFE and surfaces treated with PTMS exhibit properties expected from PTFE like a higher contact angle and less friction (see 4.7). Figure 4.6 shows the charge distribution of the surface treated glass spheres in comparison to the untreated glass spheres for PMMA and stainless steel tubes as collision material. The distributions for surface treated glass beads have a skewness with the same sign as the mean charge and are fat-tailed with an excess kurtosis of 1.06 and 1.47 for PMMA and stainless steel as tube material respectively. The mean of the distribution changes from -0.59 pC to -3.47 pC for collisions with the stainless steel tube when changing only the surfaces of the glass beads. The mean of the distributions of untreated and surface treated glass spheres is -0.87 pC and -4.46 pC respectively for collisions with the PMMA tube.

The moments of all charge distributions reported here can be found in table 4.1 in the appendix (see section 4.7). None of these distributions is close to a normal distribution. Beyond the peculiar common shape of the charge distributions, they share another feature: the standard deviation $\sigma_n$ and the mean $\mu_n$ of the charge distribution seem to be correlated. Figure 4.7 displays $\sigma_n$ as a function of $\mu_n$. The data points are taken from both our measurements with the $500\,\mu$m particles and from a previous study, where the standard deviation and the mean were reported [129]. A linear correlation of the width to the average charge can be observed in both cases, only the slopes differ for the two data sets. A correlation thus is present irrespective of material combination, surface treatment, average number of collisions, ambient conditions, setup and other experimental conditions.
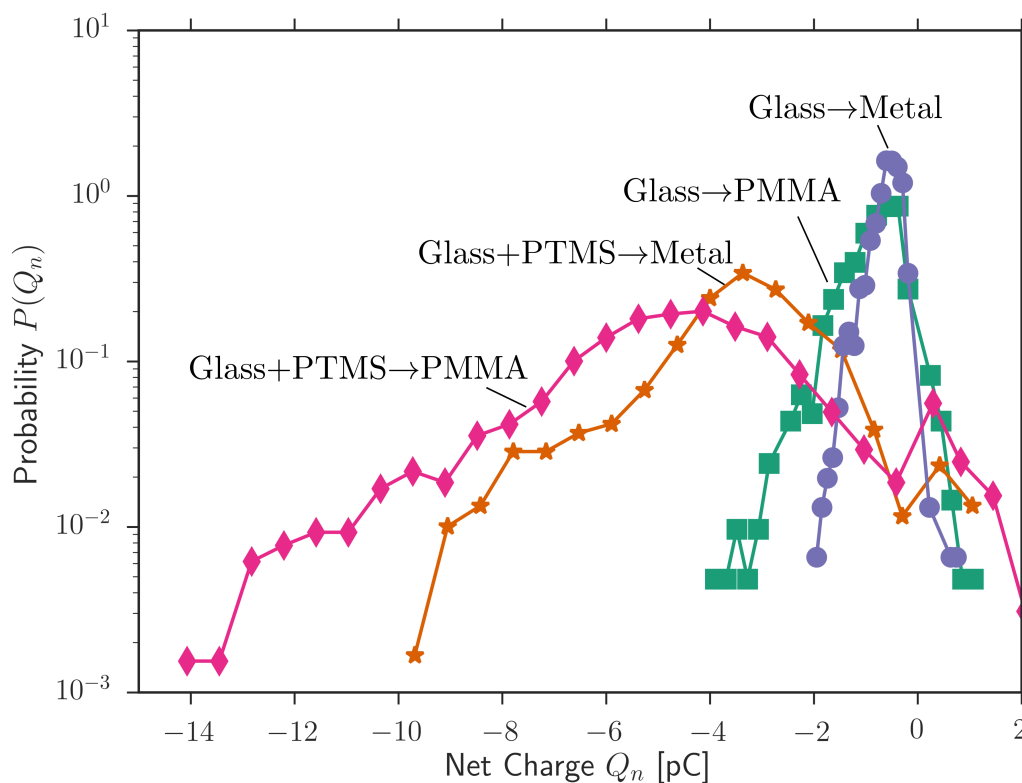
Figure 4.6: Probability distribution for charges accumulated by regular and surface treated glass spheres against tubes made from either PMMA or grounded stainless steel. The glass spheres modified with PTMS share the characteristics of asymmetry and fat-tailedness we find in other distributions. For the stainless steel tube, the mean of the distribution changes from -0.59 pC to -3.47 pC when using surface treated instead of regular glass spheres. For the PMMA tube, the mean of the distribution for regular glass beads is -0.87 pC while the distribution mean for the surface treated spheres is -4.46 pC.
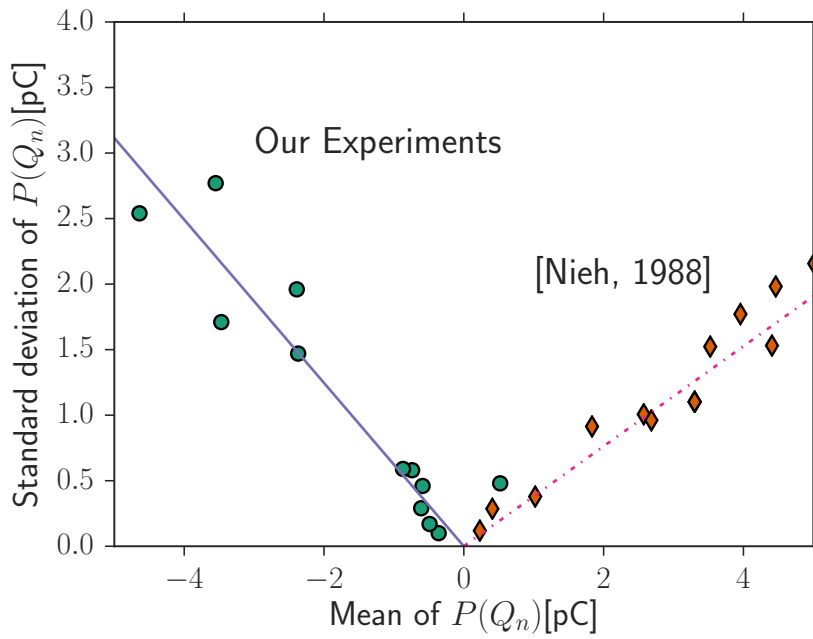
Figure 4.7: Standard deviations $\sigma_n$ of the charge distributions $P(Q_n)$ plotted as a function of the respective means $\mu_n$. The standard deviation grows linearly with the mean charge. Circles represent data from the measurements presented here, diamonds are values taken from a previous study [129]. The linear approximations describe measurements with a wide range of parameters, i.e. different materials, different surface treatments, different humidities, different number of contacts, and different setups.

## 4.4 DOUBLE STOCHASTIC MODEL

Our measurements confirm that the charge generated after breaking a contact between a particle and a solid is not a material constant, but a random variable. Particles colliding with the same material may gather positive as well as negative charges. The measured distributions of the triboelectric charges are asymmetric, i.e. mean and median differ, and they also exhibit long, close to exponentially decaying tails. These qualitative properties of the charge distributions do not change with relative humidity, type of material, or the average number or mode of the collisions. Moreover, the width of the distributions increases with the mean charge. This means that increasing the charge on a particle by more contacts or specific material combinations will also increase the fluctuations of that charge.

The observed charge distributions $P(Q_n)$ thus considerably differ from normal distributions. Availability of an improved functional form based on the observations would allow using realistic charge distributions when modeling granular media, and may guide development of extended microscopic theories. We rationalize a model based on the concepts summarized in Sec. 4.2. It can be seen that triboelectric charging is dominated by two processes, charge separation and charge recombination.

It is presently difficult to derive a functional form for the charge distribution predicted by the charge separation caused polarization and induced charging. However, the three other discussed fundamental mechanisms strongly suggest a normal distribution of initially separated charges $Q_c$ [116]. As discussed in Sec. 4.2, the net charge on a particle is the sum over many donor and acceptor sites, which may represent densities of trapped and valence band states, concentrations of separable surface groups, or concentrations of transferable polymer chains. A quantitative estimation can be derived from observed sizes of such sites [92]. Sites are observed on length scales of $4.5\mu m$ and $0.44\mu m$. In our experiment we can estimate a Hertzian contact radius of $127\mu m$ for the 4 mm glass spheres contacting the copper plate in the single contact experiments. From this one can estimate a lower limit for the number of involved sites of about 2500, justifying the use of the central limit theorem and the approximation of a normal distribution for the net separated charge $Q_c$.

The separated charges tend to equilibrate. This equilibration may happen by visible spark discharging, once the Paschen limit for initiating a breakdown is overcome [15]. Below the Paschen limit, discharging occurs by other gas discharging mechanism like dark and glow discharge [122]. The kinetics of the discharging of insulator surfaces in the presence of various discharging mechanisms and the distribution of the

exchanged charges are hard to be derived. Experimental observations have yet shown, that many discharging events superpose to the exponential discharging kinetics of a capacitor [86]. The attenuation $\alpha_d$ realized by discharging after a contact depends on the conductivity realized by the particular discharging mechanism and the time the two involved surfaces stay in proximity where discharging is efficiently possible. The total discharging of two surfaces intrinsically is the sum over several discharging events [86, 118, 119], and a normal distribution of the attenuation $\alpha_d$ is suggested as an approximation.

The net charge $Q_n$ remaining after a particular contact thus can be assumed to emerge from a normally distributed initially separated charge $Q_c$, which has decayed exponentially with a normally distributed attenuation $\alpha_d$:

$$Q_n = (Q_c | \mu_d, \sigma_d) \cdot \exp\left(-(\alpha_d | \mu_d, \sigma_d)\right), \tag{IV–1}$$

with the means and standard deviations $\mu_c$, $\sigma_c$, $\mu_d$ and $\sigma_d$. The exponential of a normally distributed variable $\alpha_d$ itself represents a lognormally distributed variable. The net charge $Q_n$ consequently is the product of a normally and a lognormally distributed variable, i.e. has a normal-lognormal distribution $P(Q_n)$ [130]. By writing

$$\exp\left(-(\alpha_d | \mu_d, \sigma_d)\right) = \exp\left(-(\alpha_d | 0, \sigma_d)\right) \cdot \exp\left(\mu_d\right). \tag{IV–2}$$

and multiplying the new exponential term to the normally distributed variable $Q_c$ one obtains

$$P(Q_n) = P((Q_c | \tilde{\mu}_c, \tilde{\sigma}_c) \cdot \exp\left(-(\alpha | 0, \sigma_d)\right)), \tag{IV–3}$$

a function of only three parameters $\tilde{\mu}_c$, $\tilde{\sigma}_c$ and $\sigma_d$. These parameters incorporate all material and ambient parameters of the configuration relevant to the charge separation and the recombination processes. Presently, in the absence of a microscopic theory, these are phenomenological parameters.

The analytical handling of this normal-lognormal distribution $P(Q_n)$ is difficult [130]. We therefore model $P(Q_n)$ numerically by drawing normally distributed random variables for the $Q_c$ and $\alpha_d$ and calculating the histogram for the final charge $Q_n$. It is instructive to consider the limiting cases of the predicted normal-lognormal distribution for $Q_n$ displayed in Fig. 4.8.

$P(Q_n)$ approaches a normal distribution and $Q_n = Q_c$ with $\sigma_d \to 0$, (Fig. 4.8, I). For a normal distribution of $Q_n$ charges of both signs are possible, the skewness and the kurtosis vanish, and the tails of the distribution decay faster than exponential, as can be seen from the semilogarithmic plot.
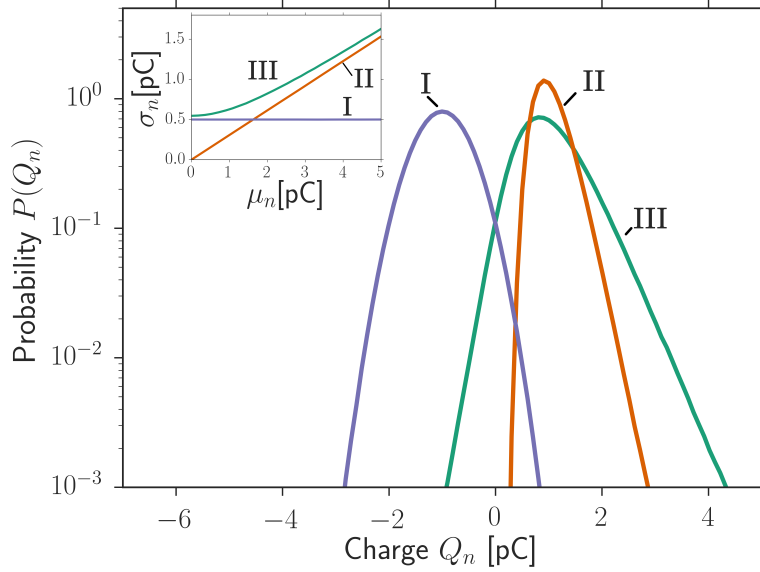
Figure 4.8: Expected shapes of the probability distribution $P(Q_n)$ of the net charges $Q_n$. I: For $\sigma_d \to 0$ no discharging occurs. The distribution is the normal distribution of the initially separated charges (here: $\tilde{\mu}_c = -1, \tilde{\sigma}_c = 0.5, \sigma_d = 10^{-6}$). II: The distribution turns into a lognormal distribution if the charge separation is deterministic and $\tilde{\sigma}_c \to 0$ (here: $\tilde{\mu}_c = 1, \tilde{\sigma}_c = 10^{-6}, \sigma_d = 0.3$). III: The intermediate case shows exponential tails, asymmetry about the mean and both positive and negative values can be reached (here: $\tilde{\mu}_c = 1, \tilde{\sigma}_c = 0.5, \sigma_d = 0.3$). The inset shows how the the standard deviation $\sigma_n$ depends on mean $\mu_n$ of the net charge $Q_n$, starting from each of the three cases above and varying the mean exchanged charge $\tilde{\mu}_c$. In the case of a lognormal and the normal-lognormal distribution a linear relation emerges.

A situation with $\tilde{\sigma}_c \to 0$, i.e. a deterministic $Q_c = \mu_c$, results in lognormally distributed $Q_n$ (Fig. 4.8, II). In this case the skewness and the excess kurtosis do not vanish, but the $Q_n$ all have the same sign.

The intermediate normal-lognormal cases combining non-vanishing $\sigma_d$ and $\tilde{\sigma}_c$ result in distributions for $Q_n$ that are not symmetric about the mean, with finite skewness and excess kurtosis, with net charges of both signs possible and with approximately exponentially decaying probabilities (Fig. 4.8, III). The probability distribution of the net charge in this normal-lognormal case thus deviates qualitatively from both the normal distribution and the lognormal distribution.

The inset of Fig. 4.8 shows the relations between the mean $\mu_n$ and the standard deviation $\sigma_n$ for all three cases. The intermediate case with a normal-lognormal distributed net charge $Q_n$ results in a linear relationship, at least for larger values of $\mu_n$. This linear dependence exists also in the case of a lognormal distribution [131]. The slopes of the linear regimes of the lognormal and the normal-lognormal distributions depend on $\sigma_d$, thus are characteristic for the discharging mechanism in the respective situation.

The normal-lognormal distribution thus exhibits the characteristics of the charge distributions observed in the experiments. Additionally it can be motivated from observations on the individual steps of charge separation and recombination presented in the literature. We consequently propose this distribution with three parameters as a minimum model to describe the shape of charge distributions generated by triboelectric charging.

# 4.5 Discussion

The measurements presented in sec. 4.3 demonstrate that the distribution of charges generated during the collisions of insulating granular particles posses characteristic features which are independent of the specifics of the experiment. These features include the possibility of charges of both signs, asymmetry, close to exponentially decaying tails and a linear correlation among standard deviation and mean.

The particular shape of the charge distribution proves that the mean particle charge is not sufficient to correctly model particle charging. Particles with charges of both signs are possible for the same material combination, and due to the approximately exponential decay of the distribution particles with extreme charges are more likely than expected from e.g. a normal distribution. The mean charge does not even describe the most likely charge that a particle has due to the strong asymmetry of the charge distribution.

The correlation among width and mean also implies, that parameters like the material combination or the number of collisions simultaneously determine how much charge is separated on average and how wide the distribution of separated charges is. Situations with large net charges will also have the greatest variation.

It is possible to systematically vary the mean net charge by using different material combinations or increasing the number of contacts. In addition, we have shown that changing only a mono layer on the particle surface and keeping the bulk material identical greatly influences the mean of the distributions. However, the charge distributions keep their characteristic general shape. Especially, they do not converge towards a normal distribution when the number of contact events is increased (controlled by the tube length). This implies that subsequent contacts of the particles do not fulfill the main requirements of the central limit theorem: statistical independence. In practical terms, this statistical dependence of subsequent triboelectric charging events demands a high efficiency of the initial neutralization of the particles used in experiments. Otherwise any residual charges from handling the particles will bias the results.

It is unclear whether this statistical dependence is due to the charging or the discharging process. Charges present on the particles may affect the uptake of new charges [14] as well as the discharging process [132]. In a recent study on the collisional triboelectric charging of a single sphere a linear increase of the charge on the sphere with the number of collisions was observed [99], suggesting a statistical independence of the charges generated during individual collisions. However, the average charge generated during collisions was orders of magnitude smaller than in the exper-

iments presented here. In the same study a strong dependence of the transfered charge on electrical fields is reported. In another recent study on polymer particles saturation of charge is apparent after tens of collisions [133]. Both these results suggest that a certain level of charge on the particles is required to obtain statistical dependence between charges transfered in subsequent collisions.

An alternative hypothesis for the statistical dependence observed in our experiments might be the small surface area of the particles. It cannot be excluded that during motion in the tube the particles contact the tube with the same spot several times or even switch to sliding motion. Depletion of charge carriers in this spot could cause statistical dependence.

We suggest a three-parameter normal-lognormal distribution for the net charge in sec. 4.4. This distribution reproduces the characteristic features of the experimentally measured charge distributions. We rationalized this shape of the distributions by combining two stochastic processes, charge separation during contact and subsequent charge recombination. This suggests that a complete description of triboelectricity requires simultaneous understanding of both the mechanisms relevant for charge separation and the mechanisms relevant for charge recombination.

The complexities arising from the combination of both the mechanisms can be illustrated by trying to connect the three parameters $\tilde{\mu}_c$, $\tilde{\sigma}_c$ and $\sigma_d$ (or $\mu_c$, $\sigma_c$, $\mu_d$ and $\sigma_d$) with the microphysical processes and the relevant parameters discussed in Sec. 4.2. Humidity for example is expected to increase mobility of charge carriers, in particular enhances presence and mobility of ions on solid surfaces. Humidity consequently could be expected to increase the mean exchanged charge $\mu_c$ and its variation [134]. On the other hand, humidity increases the mobility of charge carriers and the conductivity of air, thus can be expected to enlarge $\mu_d$ and to minimize the residual net charge [55, 135]. The factors which determine the dominating influence may be very subtle.

In future studies either charging or discharging shall be addressed separately or time-resolved measurements should be made. Humidity can be expected to affect both charging and discharging, but other parameter might be identifiable, which affect selectively the discharging. Gas atmospheres with varying conductivity or breakdown threshold with constant humidity, like $SF_6$-containing gas, may make isolating charging statistics possible [10, 15]. A setup to achieve situations with suppressed discharging using a bias voltage has also been proposed [136]. A situation where discharging is increasingly suppressed should converge to normally distributed charges $Q_n = Q_c$ with net charges of both signs possible (Fig. 4.8, I). In such a situation $\mu_c$ and $\sigma_c$ of the charging step may be studied. Time resolved measurements also may allow to distin-

guish charging and subsequent discharging and to follow the discharging kinetics [86, 118, 119].

The intermediate cases, where stochastic charging and stochastic discharging are combined, result in normal-lognormal distributions. The parameters $\mu_c$, $\sigma_c$, and $\mu_d$ turn into only two independent parameters $\tilde{\mu}_c$ and $\tilde{\sigma}_c$ (see derivation in Sec. 4.4). In this case the linear correlation among the mean $\mu_n$ and the standard deviation $\sigma_n$ of the net charge that we found in our experiments and also in a previous study reporting these parameters is particularly interesting. The model predicts that the slopes of the relation among $\mu_n$ and $\sigma_n$ are characteristic of $\sigma_d$, the standard deviation of the distributions of the attenuation coefficients $\alpha_d$. Such behavior may enable disentangling the contributions from the charging and the discharging to the final net charge in further studies.

The reasoning of the normal-lognormal distribution by combining a normal distribution for the charging step and a normal distribution for the attenuation coefficient may, of course, be a first order approximation. It relies on the experimental observations of a surface mosaic of separated charges, and an exponential decay of the charge. While the normal distribution of the separated charges is well justified by the central limit, the distribution of the attenuation coefficient is not yet clarified. Situations may arise, where several charge separation mechanisms or different charge dissipation mechanisms act simultaneously and may alter the distributions. Still, all tested situations in this work, including various materials, contact number and ambient conditions, match the predictions by a normal-lognormal distribution. This suggests that the proposed first order approximation covers already many aspects of triboelectric charging, and justifies a view of triboelectric charging as a combination of two coupled stochastic processes.

## 4.6 CONCLUSION

Triboelectric charging of granular particles is a stochastic process. The statistics of the generated net charges on the particles reveal several distinctive features: the distributions are more heavy-tailed than normal distributions with an exponential decay of the probability, are asymmetric, exhibit charges of both signs and exhibit a linear correlation among width and mean. We show that a normal-lognormal distribution is compatible with the observations. We rationalize the normal-lognormal distribution by describing triboelectric charging as a two-step random process. In the first step the

charges are separated during contact, while in the second step charge recombination occurs after separation of contact. Moreover we find that subsequent charging events are not statistically independent as the distribution of multiple triboelectric charging events does not converge to a normal distribution. The stochastic nature of granular tribocharging has direct consequences for our ability to control the tribocharging behavior: while we demonstrated that surface treatment can influence the way in which a material charges, the shape of the distribution remains the same and charges of both signs will be expected.

## 4.7 APPENDIX

### 4.7.1 DETAILS REGARDING THE ELECTRON TRANSFER MODEL FOR METALS

While the tribocharging mechanism involving insulators is still under debate, tribocharging between metals is well described by an electron transfer model. Harper [84] measured that the magnitude and direction of exchanged charge follows the difference in work function $\phi$ of the metals. Due to this, a model as depicted in figure 4.9 can be used to describe the phenomenon.

### 4.7.2 DETAILS REGARDING DEVICES USED

IONIZATION NEEDLE: A central point of our studies is the neutralization of charges on the spheres before the start of the experiment. For discharging the particles we use an ionization gun. The Haug one point ionizer we use consists of an exposed metal point electrode to which a high voltage AC signal is applied. The voltage is high enough to sustain corona glow without causing sparks. In corona discharge electrons in the air receive enough energy to ionize additional molecules and thus cause charge avalanches (Townsend avalanche). Corona glowing occurs preferentially in asymmetric geometries, i.e. a point electrode in proximity to a grounded plate [122]. Because of the asymmetric geometries, the field strength around the point electrode is high enough to permanently ionize the air but at greater distances from the point electrode, the electric field strength is weaker and a bridging of ionization channels between the electrodes in the form of sparks is prevented. The microscopic mechanisms surrounding corona discharge depend on the sign of the point electrode voltage. The ionizing gun used in our experiments is operated with AC voltage and thus both positive and negative charge carriers are produced that can neutralize charges on objects falling through the ion cloud.

CHARGE MEASUREMENT: After the discharged spheres are again charged by collision with a plate or the tube, we need to measure the charge on the spheres using the Faraday cup method. As shown in Figure 4.11, a sphere with charge $Q_S$ dropped into the Faraday cup will induce mirror charges in the conducting Faraday cup so that the region outside the Faraday cup is free of electric field. The charge the Faraday cup
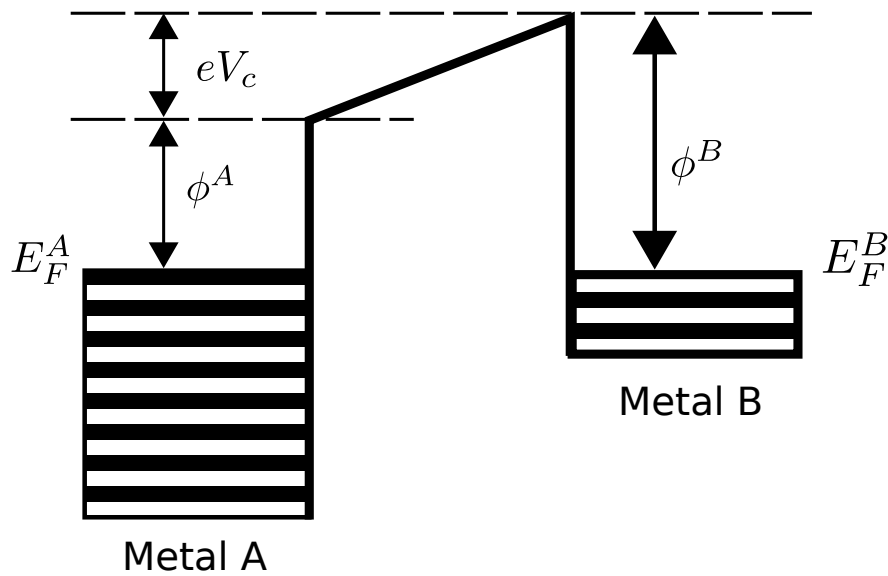
Figure 4.9: Schematic of two metals in contact. Electrons will flow from metal B to metal A until the Fermi energies have equilibrated. The amount of electrons exchanged will be proportional to the difference in surface potential $V_C = (\phi^A - \phi^B)/e$.



Figure 4.10: Ionization needle used in our experiment with the components: a) point electrode, b) ring counter electrode and c) high voltage AC transformer.
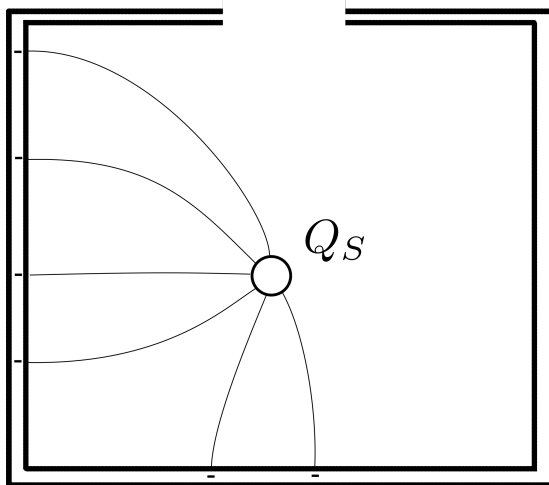
Figure 4.11: Working principle of a Faraday cup. If a charged object is placed in the cup, the electric field will be balanced by mirror charges in the metal of the cup. The charge of the object can then be determined as the integral of the current going to the cup.

needs to draw in order to accomplish this will be equal to the charge of the object $Q_S$. We can measure the charge $Q_S$ with an electrometer that contains a setup similar to the one shown in figure 4.12. A capacitor with accurately known capacitance $C_F$ is placed in the feedback loop of an operational amplifier. The charge on the capacitor will be identical to $Q_S$, the charge of the Faraday cup. We can then determine the charge $Q_S$ from the voltage $U_F$ and capacitance $C_F$ as $Q_S = U_F C_F$. That voltage is amplified and turned into a digital signal by an A/D converter. We then read out the value directly from the electrometer.

### 4.7.3 DETAILS REGARDING THE SILANIZATION TECHNIQUE

The technique used to coat the surface of the glass beads is called silanization. A silane in general is a compound with four substituents on a silicon atom. Examples include $SiH_4$, $SiCl_4$ or $Si(CH_3)_4$. Silanization is the process where a silane group is used to attach a certain rest group R to the hydroxy end of a glass surface here denoted as $SiO_3OH$. The silane group in our case is trimethoxysilane and the rest group is a fluorinated carbon chain of length 8 as shown in figure 4.13. The reaction at the glass surface will be:

$SiO_3OH + Si(CH_3)_3(CF_2)_7CF_3 \longrightarrow SiO_3CH_2Si(CH_3)_2(CF_2)_7CF_3 + H_2O$.
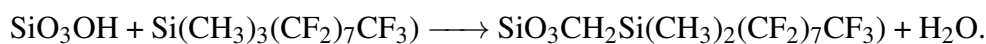
The surface treatment procedure is as follows:
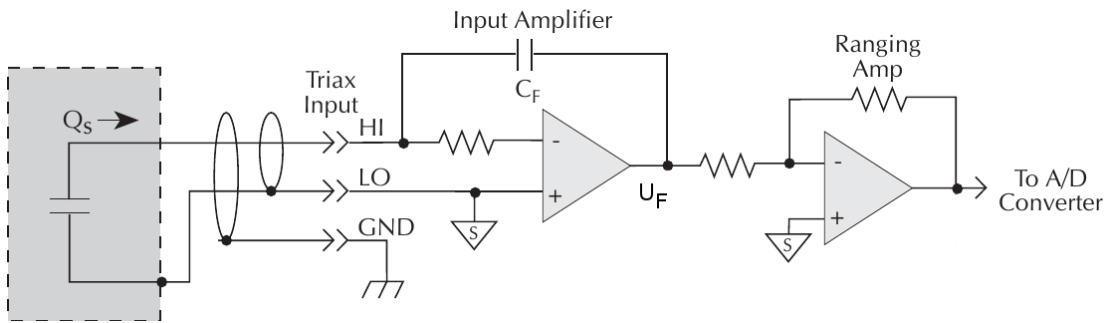
Figure 4.12: Electrical circuit used to measure charge with an electrometer. An unknown charge $Q_S$ is connected to an operational amplifier with a capacitor in the feedback loop. The capacitor has an accurately known capacitance and will mirror the charge on the Faraday cup. The source charge can therefore be calculated from the voltage $U_F$ that develops on the output of the operational amplifier and the capacitance $C_F$ according to: $Q_S = U_F C_F$. The voltage $U_F$ is amplified and read by an A/D converter. Image reprinted with permission from Keithley 6517A electrometer manual [137].

1. Cleaning and activation of glass surface in a $O_2$ plasma (Diener electronic femto) with parameters: generator power 100 W, gas pressure 0.3 mbar and duration 5 min

2. Reaction takes place in a toluene solution with 4% by volume of PTMS. Reaction time is 15 Minutes and stirring is applied during this time

3. The glass spheres are cleaned using absolute ethanol and water

We measured the water contact angle on a glass microscopy slide. If the glass slide was cleaned in the plasma device, the contact angle was close to 0°, as expected for glass. After silanization with PTMS, the contact angle increased to 107°, a value close to the literature value of PTFE (108-110°, [138]).

Measurement of the friction coefficient of glass beads against a glass microscopy slide showed a decrease in friction coefficient from 0.52 to 0.40 of the surface treated glass beads compared to cleaned glass beads.

## Glass surface    PTMS molecule

O−Si−O−Si−O−H
    |         |
    O       O

O−Si−O−Si−O−H
    |         |
    O       O

O−Si−O−Si−O−H
    |         |
    O       O
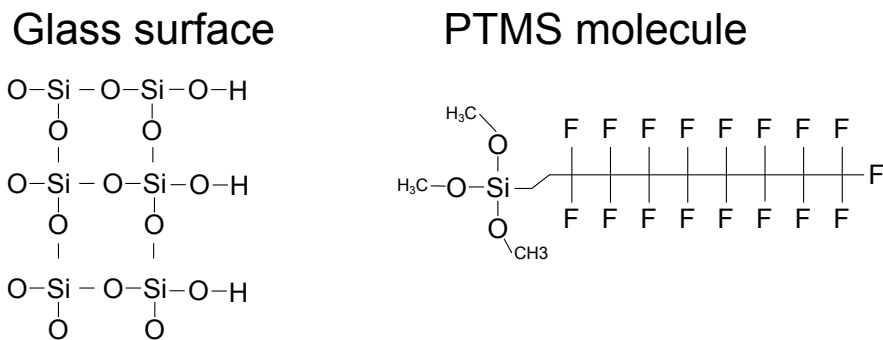
(a) Glass surface and PTMS molecule before the reaction takes place.

## Glass surface    PTMS molecule
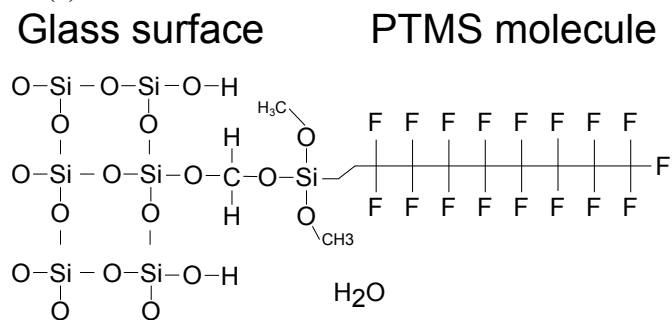
(b) Glass surface and PTMS molecule after the reaction.

Figure 4.13: Sketch of the reaction between 1H,1H,2H,2H-Perfluorodecyl-trimethoxysilane and the surface of a glass bead. The PTMS molecule attaches with its methyl group to an exposed hydroxyl group of the glass surface. From figure 4.13b, we can see why the reaction is self-terminating: a new PTMS molecule can only attach to a hydroxyl group and thus cannot attach to the already reacted PTMS.

110

### 4.7.4 CALCULATION OF HERTZIAN CONTACT AREA IN THE SINGLE COLLISION EXPERIMENT

We want to calculate the contact area of our sphere contacting the plate. According to [32, p.35], the radius of contact $r_c$ is given by:

$$r_c = F^{1/3} \left( E^* \frac{RR'}{R+R'} \right)^{1/3} \tag{IV–4}$$

where $F$ is the applied load (normal contact) and $E^*$ contains information about the materials in contact:

$$E^* = \frac{3}{4} \left( \frac{1-v^2}{E} + \frac{1-v'^2}{E'} \right). \tag{IV–5}$$

$R$ and $R'$ are the radii of the contacting spheres. The indentation during contact is given by [32]:

$$h = F^{2/3} \left[ E^{*2} \left( \frac{1}{R} + \frac{1}{R'} \right) \right]^{1/3} \tag{IV–6}$$

Finally, we have the potential energy $U$ given as [32]:

$$U = h^{5/2} \frac{2}{5E^*} \sqrt{\frac{RR'}{R+R'}} \tag{IV–7}$$

The stated relations are for two spheres contacting. The relations for a sphere contacting a plane are the limiting case of $R'$ being infinitely larger than $R$. From these relations, we can calculate the contact radius as a function of potential energy and we find for a sphere contacting a plate:

$$r_c = U^{1/5} \left( \frac{5}{2} R^2 E^* \right)^{1/5} \tag{IV–8}$$

The collisional energy $U_{\text{coll}}$ is determined from the falling height $h_f$, the particle mass $m_p$ and the impact angle $\alpha$ (see figure 4.14):

$$U_{\text{coll}} = \frac{m_p}{2} (\cos(\alpha) \sqrt{2gh_f})^2 \tag{IV–9}$$

In our experiment, where a glass sphere is impacting a copper plate, the relevant quantities are:

$$R = 2mm \qquad m_p = 0.09g \qquad h_f = 30cm \qquad \alpha = 30° \tag{IV–10}$$

$$v_{glass} = 0.24 \qquad v_{copper} = 0.35 \qquad E_{glass} = 65GPa \qquad E_{Copper} = 115GPa \tag{IV–11}$$
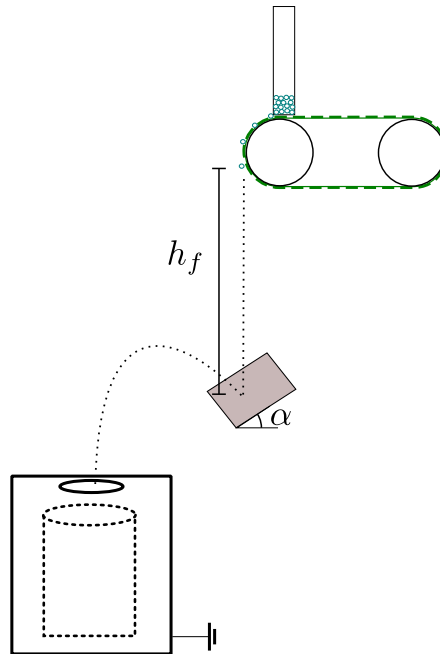
Figure 4.14: The speed at impact of the sphere contacting the plate in the single collision experiment is determined by the falling height $h_f$ and the impact angle $\alpha$.

And with that we get:

$$U_{\text{coll}} = 200\mu J \tag{IV–12}$$

$$r_c = 127\mu m \tag{IV–13}$$

$$<Q> = 0.9pC \rightarrow \text{Charge density: } 108e^-/\mu m^2 \tag{IV–14}$$

When the PTFE plate is used, the relevant quantities are:

$$v_{PTFE} = 0.48 \qquad E_{PTFE} = 420MPa \tag{IV–15}$$

$$r_c = 309\mu m \tag{IV–16}$$

$$<Q> = 4.12pC \rightarrow \text{Charge density: } 82.4e^-/\mu m^2 \tag{IV–17}$$

Table 4.1: Measured charge distributions and their moments.

| Fig. | Sphere Material | Sphere Diameter [mm] | Target Material | Length [cm] | Relative Humidity [%] | Mean Charge [pC] | Median Charge [pC] | Standard Deviation [pC] | Skew | Excess Kurtosis | Sample Size |
|---|---|---|---|---|---|---|---|---|---|---|---|
| 4.2 a) | Glass | 4 | PTFE | Plate | 50 | 4.12 | 6.83 | 14.54 | -1.16 | 1.63 | 991 |
| 4.2 b) | Glass | 4 | Copper | Plate | 50 | 0.90 | -0.49 | 3.82 | 1.89 | 5.20 | 764 |
| 4.3 | Glass | 0.5 | PMMA | 20 | NA | -2.37 | -2.33 | 1.47 | -0.34 | 0.72 | 556 |
| 4.3 | Glass | 0.5 | PMMA | 80 | NA | -2.39 | -1.68 | 1.96 | -0.99 | 0.59 | 399 |
| 4.3 | Glass | 0.5 | PMMA | 100 | NA | -3.55 | -2.81 | 2.77 | -1.38 | 1.96 | 525 |
| 4.4 | Glass | 0.5 | Metal | 40 | 20 | -0.74 | -0.56 | 0.58 | -2.06 | 5.60 | 429 |
| 4.4, 4.5, 4.6 | Glass | 0.5 | Metal | 40 | 30 | -0.61 | -0.56 | 0.29 | -1.02 | 2.03 | 1474 |
| 4.4 | Glass | 0.5 | Metal | 40 | 60 | -0.59 | -0.44 | 0.46 | -1.85 | 4.32 | 323 |
| 4.5 4.6 | Glass | 0.5 | PMMA | 40 | 20 | -0.87 | -0.76 | 0.59 | -1.00 | 2.66 | 998 |
| 4.5 | PS | 0.5 | PMMA | 40 | 25 | -0.36 | -0.35 | 0.10 | -0.86 | 2.34 | 406 |
| 4.5 | PS | 0.5 | Metal | 40 | 35 | -0.49 | -0.49 | 0.17 | -0.07 | 3.59 | 686 |
| 4.5 | Glass | 0.5 | PTFE | 40 | NA | 0.52 | 0.43 | 0.48 | 0.46 | 4.69 | 134 |
| 4.6 | PTMS | 0.5 | Metal | 40 | 25 | -3.47 | -3.32 | 1.71 | -0.66 | 1.47 | 945 |
| 4.6 | PTMS | 0.5 | PMMA | 40 | 27 | -4.64 | -4.58 | 2.54 | -0.26 | 1.06 | 1043 |

# BIBLIOGRAPHY

[9]     D. J. Lacks, N. Duff, and S. K. Kumar. "Nonequilibrium Accumulation of Surface Species and Triboelectric Charging in Single Component Particulate Systems". *Physical Review Letters* 100.18 (May 2008), p. 188305.

[10]    L. S. McCarty, A. Winkleman, and G. M. Whitesides. "Ionic Electrets: Electrostatic Charging of Surfaces by Transferring Mobile Ions upon Contact". *Journal of the American Chemical Society* 129.13 (Apr. 2007), pp. 4075–4088.

[11]    F. Galembeck, T. A. L. Burgo, L. B. S. Balestrin, R. F. Gouveia, C. A. Silva, and A. Galembeck. "Friction, tribochemistry and triboelectricity: recent progress and perspectives". *RSC Adv.* 4.109 (Nov. 2014), pp. 64280–64298.

[12]    S. R. Waitukaitis, V. Lee, J. M. Pierson, S. L. Forman, and H. M. Jaeger. "Size-dependent same-material tribocharging in insulating grains". *Physical Review Letters* 112.21 (2014), p. 218001.

[13]    T. R. D. Ducati, L. H. Simões, and F. Galembeck. "Charge Partitioning at Gas-Solid Interfaces: Humidity Causes Electricity Buildup on Metals". *Langmuir* 26.17 (Sept. 2010), pp. 13763–13766.

[14]    T. Shinbrot, T. S. Komatsu, and Q. Zhao. "Spontaneous tribocharging of similar materials". *EPL (Europhysics Letters)* 83.2 (July 2008), p. 24004.

[15]    T. Matsuyama and H. Yamamoto. "Charge relaxation process dominates contact charging of a particle in atmospheric conditions". *Journal of Physics D: Applied Physics* 28.12 (1995), p. 2418.

[17]    C. Cimarelli, M. A. Alatorre-Ibargüengoitia, U. Kueppers, B. Scheu, and D. B. Dingwell. "Experimental generation of volcanic lightning". *Geology* 42.1 (Jan. 2014), pp. 79–82.

[18]    C. Cimarelli, M. A. Alatorre-Ibargüengoitia, K. Aizawa, A. Yokoo, A. Díaz-Marina, M. Iguchi, and D. B. Dingwell. "Multiparametric observation of volcanic lightning: Sakurajima Volcano, Japan". *Geophysical Research Letters* 43.9 (May 2016), pp. 4221–4228.

[19]    C. D. Stow. "Dust and Sand Storm Electrification". *Weather* 24.4 (Apr. 1969), pp. 134–144.

[31] H. Hertz. "Ueber die Berührung fester elastischer Körper". *Journal für die reine und angewandte Mathematik* 92 (1882), pp. 156–171.

[32] L. D. Landau and E. Lifshitz. "Theory of Elasticity, vol. 7". *Course of Theoretical Physics* 3 (1986), p. 109.

[55] A. Schella, S. Herminghaus, and M. Schröter. "Influence of humidity on triboelectric charging and segregation in shaken granular media". *Soft Matter* 13.2 (2017), pp. 394–401.

[82] P. E. Shaw. "Experiments on tribo-electricity. I.—The tribo-electric series". *Proceedings of the Royal Society A* 94.656 (Nov. 1917), pp. 16–33.

[83] L. B. Loeb. "The basic Mechanisms of Static Electrification". *Science* 102.2658 (Dec. 1945), pp. 573–576.

[84] W. R. Harper. "Electrification following the contact of solids". *Contemporary Physics* 2.5 (June 1961), pp. 345–359.

[85] M. Glor. "Hazards due to electrostatic charging of powders". *Journal of Electrostatics* 16.2 (May 1985), pp. 175–191.

[86] N. Gibson and F. C. Lloyd. "Incendivity of discharges from electrostatically charged plastics". *British Journal of Applied Physics* 16.11 (1965), p. 1619.

[87] D. M. Pai and B. E. Springett. "Physics of electrophotography". *Reviews of Modern Physics* 65.1 (Jan. 1993), pp. 163–211.

[88] A. G. Bailey. "The science and technology of electrostatic powder spraying, transport and coating". *Journal of Electrostatics* 45.2 (Dec. 1998), pp. 85–120.

[89] A. Mizuno. "Electrostatic precipitation". *IEEE Transactions on Dielectrics and Electrical Insulation* 7.5 (Oct. 2000), pp. 615–624.

[90] H. Kawamoto, M. Uchiyama, B. L. Cooper, and D. S. McKay. "Mitigation of lunar dust on solar panels and optical elements utilizing electrostatic traveling-wave". *Journal of Electrostatics* 69.4 (Aug. 2011), pp. 370–379.

[91] C. I. Calle, C. R. Buhler, M. R. Johansen, M. D. Hogue, and S. J. Snyder. "Active dust control and mitigation technology for lunar and Martian exploration". *Acta Astronautica* 69.11 (Dec. 2011), pp. 1082–1088.

[92] H. T. Baytekin, A. Z. Patashinski, M. Branicki, B. Baytekin, S. Soh, and B. A. Grzybowski. "The mosaic of surface charge in contact electrification". *Science* 333.6040 (2011), pp. 308–312.

[93] D. J. Lacks. "The Unpredictability of Electrostatic Charging". *Angewandte Chemie International Edition* 51.28 (July 2012), pp. 6822–6823.

[94] J. Lowell and A. Rose-Innes. "Contact electrification". *Advances in Physics* 29.6 (Dec. 1980), pp. 947–1023.

[95] J. Lowell and W. S. Truscott. "Triboelectrification of identical insulators. I. An experimental investigation". *Journal of physics D: Applied physics* 19.7 (1986), p. 1273.

[96] A. F. Diaz and R. M. Felix-Navarro. "A semi-quantitative tribo-electric series for polymeric materials: the influence of chemical structure and properties". *Journal of Electrostatics* 62.4 (Nov. 2004), pp. 277–290.

[97] C. H. Park, J. K. Park, H. S. Jeon, and B. C. Chun. "Triboelectric series and charging properties of plastics using the designed vertical-reciprocation charger". *Journal of Electrostatics* 66.11 (Nov. 2008), pp. 578–583.

[98] L. S. McCarty and G. M. Whitesides. "Electrostatic Charging Due to Separation of Ions at Interfaces: Contact Electrification of Ionic Electrets". *Angewandte Chemie International Edition* 47.12 (Mar. 2008), pp. 2188–2207.

[99] V. Lee, N. M. James, S. Waitukaitis, and H. M. Jaeger. "Collisional Charging of Individual Sub-Millimeter Particles: Using Ultrasonic Levitation to Initiate and Track Charge Transfer". *arXiv preprint arXiv:1801.09278* (2018).

[100] E. Németh, V. Albrecht, G. Schubert, and F. Simon. "Polymer tribo-electric charging: dependence on thermodynamic surface properties and relative humidity". *Journal of Electrostatics* 58.1 (May 2003), pp. 3–16.

[101] D. W. Howell, I. S. Aronson, and G. W. Crabtree. "Dynamics of electrostatically driven granular media: Effects of humidity". *Physical Review E* 63.5 (Apr. 2001), p. 050301.

[102] L. Xie, N. Bao, Y. Jiang, and J. Zhou. "Effect of humidity on contact electrification due to collision between spherical particles". *AIP Advances* 6.3 (Mar. 2016), p. 035117.

[103] T. Poppe and R. Schräpler. "Further experiments on collisional tribocharging of cosmic grains". *Astronomy & Astrophysics* 438.1 (July 2005), pp. 1–9.

[104] M. Sow, R. Widenor, A. Kumar, S. W. Lee, D. J. Lacks, and R. M. Sankaran. "Strain-Induced Reversal of Charge Transfer in Contact Electrification". *Angewandte Chemie International Edition* 51.11 (Mar. 2012), pp. 2695–2697.

[105] T. Matsusyama and H. Yamamoto. "Impact charging of particulate materials". *Chemical Engineering Science*. Papers Presented at the Eleventh and Twelfth Nisshin Engineering Particle Technology International Symposium 61.7 (Apr. 2006), pp. 2230–2238.

[106] P. M. Ireland. "Triboelectrification of particulate flows on surfaces: Part I — Experiments". *Powder Technology* 198.2 (Mar. 2010), pp. 189–198.

[107] P. M. Ireland. "Triboelectrification of particulate flows on surfaces: Part II — Mechanisms and models". *Powder Technology* 198.2 (Mar. 2010), pp. 199–210.

[108] P. M. Ireland. "Dynamic particle-surface tribocharging: The role of shape and contact mode". *Journal of Electrostatics* 70.6 (Dec. 1, 2012), pp. 524–531.

[109] D. L. Wood and J. Tauc. "Weak Absorption Tails in Amorphous Semiconductors". *Physical Review B* 5.8 (Apr. 1972), pp. 3144–3151.

[110] T. A. L. Burgo, T. R. D. Ducati, K. R. Francisco, K. J. Clinckspoor, F. Galembeck, and S. E. Galembeck. "Triboelectricity: Macroscopic Charge Patterns Formed by Self-Arraying Ions on Polymer Surfaces". *Langmuir* 28.19 (May 2012), pp. 7407–7416.

[111] H. T. Baytekin, B. Baytekin, J. T. Incorvati, and B. A. Grzybowski. "Material Transfer and Polarity Reversal in Contact Charging". en. *Angewandte Chemie* 124.20 (May 2012), pp. 4927–4931.

[112] R. Yoshimatsu, N. a. M. Araújo, G. Wurm, H. J. Herrmann, and T. Shinbrot. "Self-charging of identical grains in the absence of an external field". en. *Scientific Reports* 7 (Jan. 2017), p. 39996.

[113] M. W. Williams. "Triboelectric charging of insulating polymers: some new perspectives". *AIP Advances* 2.1 (2012), p. 010701.

[114] D. J. Lacks and R. M. Sankaran. "Contact electrification of insulating materials". *Journal of Physics D: Applied Physics* 44.45 (Nov. 2011), p. 453001.

[115] S. Matsusaka, H. Maruyama, T. Matsuyama, and M. Ghadiri. "Triboelectric charging of powders: A review". *Chemical Engineering Science* 65.22 (2010), pp. 5781–5807.

[116] M. M. Apodaca, P. J. Wesson, K. J. M. Bishop, M. A. Ratner, and B. A. Grzybowski. "Contact Electrification between Identical Materials". *Angewandte Chemie* 122.5 (Jan. 2010), pp. 958–961.

[117]  J. A. Medley. "Frictional Electrification and Gaseous Discharge". *Nature* 166.4221 (Sept. 1950), 166524a0.

[118]  R. G. Horn and D. T. Smith. "Contact electrification and adhesion between dissimilar materials". *Science* 256.5055 (1992), pp. 362–364.

[119]  R. G. Horn, D. T. Smith, and A. Grabbe. "Contact electrification induced by monolayer modification of a surface and relation to acid–base interactions". *Nature* 366.6454 (Dec. 1993), pp. 442–443.

[120]  R. Elsdon and F. R. G. Mitchell. "Contact electrification of polymers". *Journal of Physics D: Applied Physics* 9.10 (1976), p. 1445.

[121]  W. D. Greason. "Triboelectrification of wood with PTFE". *Journal of Electrostatics* 71.2 (Apr. 2013), pp. 140–144.

[122]  C. F. Gallo. "Corona-A Brief Status Report". *IEEE Transactions on Industry Applications* IA-13.6 (Nov. 1977), pp. 550–557.

[123]  F. Paschen. "Ueber die zum Funkenübergang in Luft, Wasserstoff und Kohlensäure bei verschiedenen Drucken erforderliche Potentialdifferenz". *Annalen der Physik* 273.5 (Jan. 1889), pp. 69–96.

[124]  L. B. Loeb. "Statistical Factors in Spark Discharge Mechanisms". *Reviews of Modern Physics* 20.1 (Jan. 1948), pp. 151–160.

[125]  P. M. Davidson. "The statistics of ionization currents in gases between parallel plates". *Proceedings of the Physical Society* 83.2 (1964), p. 259.

[126]  M. Yoshida, A. Shimosaka, Y. Shirakawa, J. Hidaka, T. Matsuyama, and H. Yamamoto. "Estimation of electrostatic charge distribution of flowing toner particles in contact with metals". *Powder technology* 135 (2003), pp. 23–34.

[127]  M. K. Mazumder, R. E. Ware, T. Yokoyama, B. J. Rubin, and D. Kamp. "Measurement of particle size and electrostatic charge distributions on toners using E-SPART analyzer". *IEEE Transactions on Industry Applications* 27.4 (1991), pp. 611–619.

[128]  T. Matsuyama, M. Ogu, H. Yamamoto, J. C. Marijnissen, and B. Scarlett. "Impact charging experiments with single particles of hundred micrometre size". *Powder technology* 135 (2003), pp. 14–22.

[129]  S. Nieh and T. Nguyen. "Effects of humidity, conveying velocity, and particle size on electrostatic charges of glass beads in a gaseous suspension flow". *Journal of Electrostatics* 21.1 (July 1988), pp. 99–114.

[130]  M. Yang. "Normal log-normal mixture, leptokurtosis and skewness". *Applied Economics Letters* 15.9 (July 2008), pp. 737–742.

[131]  E. Limpert, W. A. Stahel, and M. Abbt. "Log-normal Distributions across the Sciences: Keys and Clues". *AIBS Bulletin* 51.5 (2001), pp. 341–352.

[132]  L. Stollenwerk, J. G. Laven, and H.-G. Purwins. "Spatially Resolved Surface-Charge Measurement in a Planar Dielectric-Barrier Discharge System". *Physical Review Letters* 98.25 (June 2007), p. 255001.

[133]  F. Chowdhury, A. Sowinski, M. Ray, A. Passalacqua, and P. Mehrani. "Charge generation and saturation on polymer particles due to single and repeated particle-metal contacts". *Journal of Electrostatics* 91 (Feb. 2018), pp. 9–15.

[134]  S. Pence, V. J. Novotny, and A. F. Diaz. "Effect of Surface Moisture on Contact Charge of Polymers Containing Ions". en. *Langmuir* 10.2 (Feb. 1994), pp. 592–596.

[135]  K. W. Biegaj, M. G. Rowland, T. M. Lukas, and J. Y. Y. Heng. "Surface Chemistry and Humidity in Powder Electrostatics: A Comparative Study between Tribocharging and Corona Discharge". *ACS Omega* 2.4 (Apr. 2017), pp. 1576–1582.

[136]  P. M. Ireland. "Contact charge accumulation and separation discharge". *Journal of Electrostatics*. 11th International Conference on Electrostatics 67.2 (May 2009), pp. 462–467.

[137]  Keithley Instruments Inc. *Model 6517A Electrometer User's Manual*. 1996.

[138]  H. W. Fox and W. A. Zisman. "The spreading of liquids on low energy surfaces. I. polytetrafluoroethylene". *Journal of Colloid Science* 5.6 (Dec. 1, 1950), pp. 514–531.

# 5 PACKING UNDER THE INFLUENCE OF TRIBOCHARGING

Electrostatic forces induced by tribocharging influence packing behavior of agitated granular sphere packings. We investigate the packing structure of a two material system designed to maximize attractive interparticle electrostatic interactions and find a body centered cubic arrangement with systematic deformations. In contrast, an otherwise identical single material system shows no signs of ordering. We additionally show that container interactions can greatly influence packing behavior and in our case lead to locally ordered structures near the wall without indications of global ordering.

## 5.1 INTRODUCTION

Granular spheres can achieve disordered and ordered states. The building of permanent contacts and lack of thermal motion typically limit the achievable densities. Monodisperse spherical granular media typically pack in the range between $\varphi_{RLP} = 0.55 - 0.573$ [68, 139] and $\varphi_{RCP} = 0.635 - 0.655$ [140–142] under the influence of gravity. The lower limit is typically referred to as random loose packing (RLP), while the upper limit is called random close packing (RCP). RCP describes the closest packed state achievable by experimental protocols such as shaking [143, 144], centrifugation [145] or sedimentation [68] and is amorphous without crystalline phases. Packing fractions higher than RCP are accompanied by crystalline phases and can be achieved by experimental protocols such as multidimensional shaking [146, 147], cyclic shear [78, 148], shear in a Couette cell [149] or epitaxy [150–152]. The crystalline phases typically observed in granular media are either Hexagonal close packed (HCP) or face centered cubic (FCC), both of which have a packing fraction of $\varphi_{HCP} = \varphi_{FCC} = \pi/\sqrt{18} \approx 0.74$.

A defining characteristic of a granular medium is the contact network which is formed since granular media can only transfer a force through contacts. The relation between granular structure and force network has been studied in 2D granular assemblies [153], simulations [45], theory [154, 155] and 3D experiments [146, 156, 157]. Mueggenburg et al. measured the response at the bottom of a packing to a locally applied force at the top. The pattern of forces at the bottom was focused in the

center for amorphous packings, formed a ring for HCP and a triangular arrangement of force maxima for FCC [156]. The influence of the force network on mechanical strength was shown by Muthuswamy and Tordesillas [45] who conclude that straighter chains are able to sustain a higher load but also that systems with more branching in the force network are mechanically stable. Hanifpour et al. have found that polycrystalline packings of spheres still have a highly random mechanical backbone similar to that of amorphous packings [146].

The unclear emergence of macroscopic mechanical properties from the packing structure of granular media motivated us to find new ways of influencing packing behavior by introduction of controlled electrostatic tribocharging. We will review the mechanisms that induce ordering in various systems in section 5.2. We will present three experiments in section 5.3 aiming to determine the ways in which inter-particle charging and interactions with the container can influence the packing structure for vertically vibrated samples. Our experiments show that an equal number mixture of monodisperse spheres made of Teflon and nylon will form a charge dominated crystalline BCC structure when the influences of the container are minimized (see section 5.4). If the container geometry facilitates crystalline structures and if charging against the container is not suppressed, we instead see crystallization near the container walls in the densest possible packings of HCP and FCC. In an experiment where only same material charging can occur and the interactions with the wall are minimized, we see no crystallization in the time frame of the experiment.

We will discuss those findings and the importance of charging in the packing in section 5.5. Section 5.7.1 contains details about the measurement method and implementation of the data analysis that was used.


## 5.2 MECHANISMS OF ORDERING IN RELATED SYSTEMS

HARD SPHERE SYSTEMS Hard sphere systems are of interest due to their phase transition between a disordered and an ordered state. The relevant control parameter is the global packing fraction $\varphi_{\text{global}}$. The hard sphere model has been shown to have an entropy driven [158] first order phase transition from a fluid to a crystalline phase [159, 160] with freezing density at $\varphi = 0.495$ and a melting density of $\varphi = 0.545$ and a coexistence region in between.

(a) Sodium chloride structure.       (b) Cesium chloride structure.
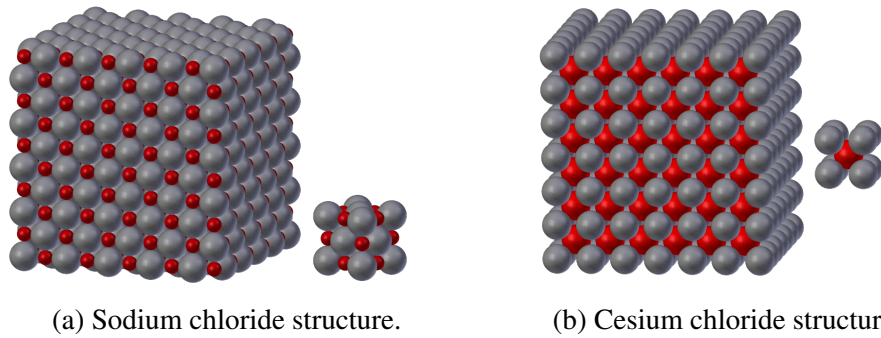
Figure 5.1: Examples of crystal structures in ionic crystals. Figure 5.1a shows the sodium chloride structure and its unit cell

SELF ASSEMBLY OF COLLOIDS AND DUSTY PLASMAS   A good example of microscopic, electrostatic interactions determining macroscopic behavior is the application to self assembly (SA) [161]. Whitesides and Grzybowski define SA as "the autonomous organization of components into patterns or structures without human intervention." As such, it is the components themselves which have the macroscopic behavior encoded in them. SA has been studied in many systems with varying length scales and complexities. At the molecular scale, proteins self assemble into DNA strands that form the basis for all life.

Another example are dust particles arranging in crystals inside a plasma field [162, 163]. The dust particles are charged by the plasma and form crystals based on the repulsive, electrostatic interactions forming between the dust particles. In experiments on the ISS, 3D plasma crystals oriented in a BCC structure could be observed [163].

Crystallization of mesoscale colloids is a process studied recently [164, 165]. Colloidal systems have the advantage that gravity effects can be effectively controlled by density-matching the colloids and the suspension. In a two-component system, the suspension was tuned so that the effective charge on one species was positive while that on the other one was negative. A BCC crystal structure formed [164] when the size ratio between the two components was close to unity. The crystal that forms has a NaCl-like lattice [165] when the size ratio is decreased to 0.3.

IONIC CRYSTALS   The atoms with lowest energy and highest ionization energy are generally those with a completely filled outer electron shell, called the valence shell [166]. A sodium (Na) atom can combine with a chloride (Cl) atom by exchange of one electron going from Na to Cl so that each atom achieves a filled valence shell. The ex-

| Ion radius ratio | Coordination number | Crystal type | Crystal structure of constituents | Lattice structure (constituent blind) |
| --- | --- | --- | --- | --- |
| 0.22 - 0.41 | 4 | ZnS | FCC | Diamond |
| 0.41 - 0.73 | 6 | NaCl | FCC | SC |
| 0.73 - 1 | 8 | CsCl | SC | BCC |

Table 5.1: Expected lattice type and coordination number as a function of the radius ratio of the ions [167].

change of an electron leaves Na with a positive charge while Cl has one extra negative charge. The electrostatic interaction between the ions leads to formation of an ionic bond. At room temperature, $Na^+Cl^-$ forms an ionic crystal, where each constituent arranges in a FCC lattice as shown in figure 5.1a. The second most common ionic crystal structure is that of cesium chloride (CsCl), that is shown in figure 5.1b. Here, the constituents form a simple cubic lattice where each cation is in the center of the cube formed by the anions. Because of this, the CsCl arrangement is also often referred to as having BCC structure [166], which is only true when not differentiating between different constituents. A rule that has in the past been used to predict which crystal structure will be most stable is the first Pauling rule [167]. In an ionic crystal, the electrostatic potential is minimized by reducing the distance between cations and anions while maximizing the distance between anions. Pauling thus calculated the maximum amount of anions that can be grouped around a cation without the anions touching each other depending on the ion size ratio. Those size ratios and examples of corresponding lattice arrangements are given in table 5.1.

The lower threshold for the NaCl structure is calculated by considering bigger spheres in a FCC lattice configuration and smaller spheres in the gaps between them. Figure 5.2a shows the face of a fcc unit cell with spheres of diameter $d$ and a virtual sphere placed in the gap on one of the edges. From the figure we can see that a minimum radius ratio of $\sqrt{2} - 1 \approx 0.41$ for the virtual sphere is needed to separate the anions. Then there will be 6 contacts between the anions and cations.

Similar considerations can be made for bigger spheres arranged in a simple cubic (SC) lattice with a smaller sphere in the center of the unit cell (see fig. 5.2b). If the smaller sphere radius is at least $\sqrt{3} - 1 \approx 0.73$ times the radius of the bigger sphere a CsCl structure can be formed which then has 8 cation-anion contacts.

The fact that these rules are based purely on geometric considerations makes them nicely applicable to hard-sphere systems. However, we need to point out that for ionic
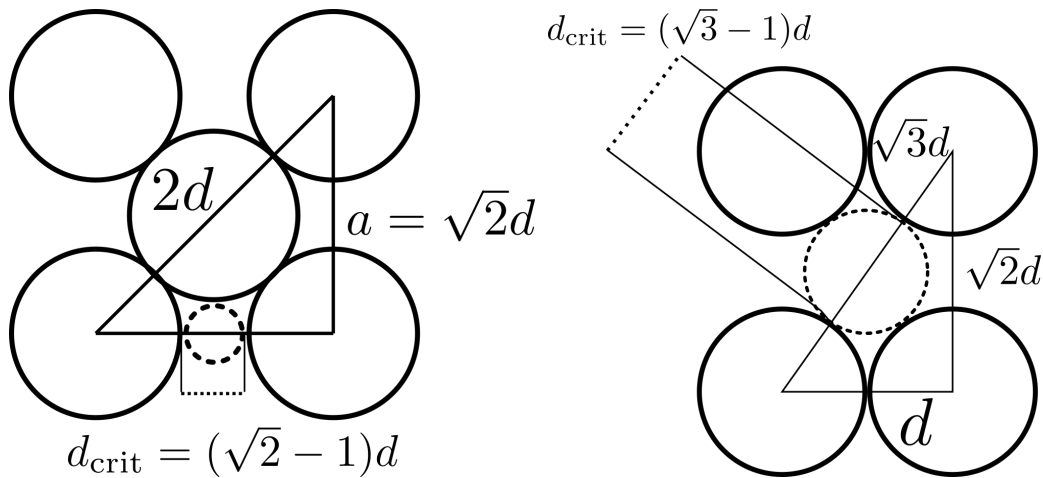
(a) Minimum radius required to stabilize NaCl structure.

(b) Minimum radius required to stabilize CsCl structure.

Figure 5.2: Visualization of the minimum critical radius a virtual sphere (dashed) needs to have to completely fill the gap formed in the unit lattice. Fig. 5.2a shows a face of a fcc unit cell, while fig. 5.2b shows the diagonal cross section through a simple cubic unit cell.

crystals there are many exceptions to the first Pauling rule. For example, sodium and fluorine form NaF which is in NaCl configuration at room conditions [168] despite the cation and anion being roughly the same size. In addition, CsCl and additional CsCl-type salts have a phase transition at higher temperatures to a NaCl-like structure that cannot be explained by such a simple rule [168, 169]. Instead, a combination of electrostatic potential and quantum energy considerations have to be used to predict these phase transitions.

ORDERING MECHANISMS IN GRANULAR SYSTEMS    Self assembly for granular particles has been studied in two-dimensional systems with triboelectric charging as the main driving force [170, 171]. Grzybowski et al. found either square, pentagonal or hexagonal lattices to form depending on the ratio of Teflon to nylon spheres. The lattice that forms additionally depends on agitation parameters with square lattices favored at higher amplitudes and frequencies [171]. Cademartiri et al. show that an equal mixture of Teflon and nylon spheres agitated in an aluminum dish has a square lattice where both species of spheres are highly charged [170]. In contrast, the aluminum dish filled with only nylon or only Teflon spheres shows looser structures with less

charge on the spheres. The authors also mention a minimum charge of $|Q| > 500 \, \text{pC}$ on 3.18 mm spheres required to achieve close packing, where spheres with less charge instead tended to form one-dimensional chains. Only few studies have been performed on two component electrostatics-driven crystallization in 3D granular media [55].

Predicting the behavior of a three dimensional granular system with electrostatic charging and gravity present is difficult since granular systems are dissipative and athermal. Still, it is obvious that for sufficiently large charging, the system should tend to self-arrange to minimize electrostatic interactions. It may be instructive to consider these equilibrium states or branches that the system may end up in.
The difficulties of predicting the behavior of athermal systems with noise are summarized by Horsthemke and Lefever who write [172, p.4]:

> "It has been found that the mechanisms of self-organization become much more complex in strongly dissipative systems than in conservative, equilibrium-type systems. In the vicinity of a stable thermodynamic equilibrium state, the behavior of a dissipative system can easily be predicted, given that in this domain it possesses a unique attractor, namely the thermodynamic branch. Far from thermodynamic equilibrium on the contrary, the same system may possess an amazingly complex network of bifurcations. The importance of elements of chance such as internal fluctuations then inevitably increases. Their influence becomes crucial in the choices which the system makes in the course of its evolution between the numerous basins of attraction, or dissipative structures, to which bifurcations give rise."

We can summarize three possible driving forces that will lead to crystallization in granular media:

- **Entropy maximization:** The hard-sphere simulations by Adler and Wainright exhibit a phase transition to FCC structure above the freezing packing fraction. This effect can also be shown in two-dimensional granular media where gravity does not influence the behavior. It is therefore likely that this driving force is the main contributor for granular crystallization without external potentials. The predicted structures will be either FCC or HCP, since the free energy difference between the two structures "is not significantly different from zero" [173].

- **Gravity potential minimization:** Particularly considering the epitaxy-based

experiments, it can become obvious how gravity potential minimization leads to crystallization. If spheres are injected one at a time onto an already crystalline substrate, the obvious point where they will come to rest will be in the space in between three touching spheres. This way, a new layer will eventually be formed. Experiments have been done that show both FCC [150, 151] and HCP [152] depending on container geometry. The relevance of this mechanism as driving force for crystallization in our experiments is unknown, and an additional consideration is that the structure that forms needs to be stable against the influences of gravity.

- **Electrostatic potential minimization:** Tribocharging between dissimilar materials can lead to oppositely charged spheres similar in concept to an ionic crystal. When the size ratio between positively charged spheres and negatively charged spheres is close to unity, one expects a CsCl-like BCC structure to form (see 5.2).

This makes a predictive theory very difficult to develop also because it might not only be the relative strength of each effect but also the time-scale on which they lead to crystallization that determines which structure will ultimately be reached. Additionally, interactions with the container can become important on the one hand because tribocharging will inevitably occur not just between the spheres but also between the spheres and the container and on the other hand because the wall can provide a nucleation site from which crystallization can occur. Finally, the way that the system is driven can be expected to not only influence the packing structure itself but also the way in which charge builds up in sphere collisions.

GRANULAR COLUMNS SUBJECTED TO VERTICAL VIBRATIONS   We need to agitate our granular media in order for reorganizations to become possible since granular media are dissipative and athermal. Given how crucial these agitation dynamics are for our experiments, it is instructive to consider how granular media behave when subjected to vertical vibrations. Simulations and experiments by Luding et al.[174, 175] show that a one-dimensional column of spheres subjected to vertical vibrations exhibits two regimes: one in which the spheres move collectively as a solid bloc and one in which the spheres only make contact sporadically and spend most of their time apart.

 The control parameter that determines the transition between the condensed and fluidized regime is the acceleration of the bottom plate where higher accelerations favor
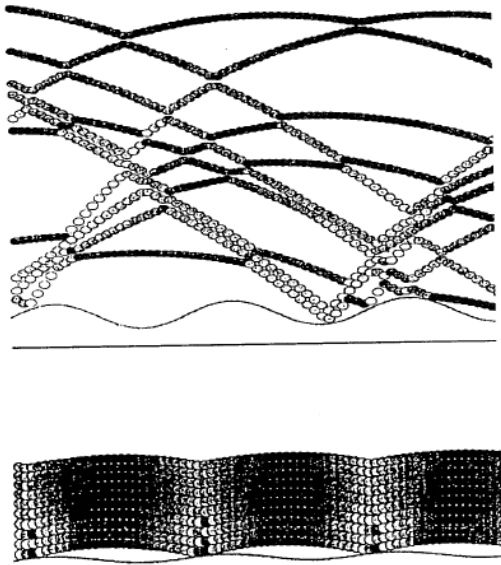
Figure 5.3: Driving regimes encountered for vertical columns of spheres. The system consists of 10 spheres vertically stacked in one dimension. Time progresses going from left to right in the figure. The motion of the bottom plate is indicated by a solid line. Top: For high accelerations and low dissipation a fluidized regime where the spheres are not in contact the majority of the time is simulated. Bottom: For lower accelerations or high dissipation the condensed regime is entered where spheres remain in contact the majority of the time. Figure reprinted with permission from [176, p. 81]

the fluidized regime. An additional parameter governing this transition is the reduced number $X = N_Z(1 - \varepsilon_p)$ that depends on the number of spheres in the column $N_Z$ and the coefficient of restitution between the spheres $\varepsilon_p$. For a sub critical value $X \leq X_C \approx \pi$, the system switches between the condensed regime and the fluidized regime at some acceleration. For $X \geq X_C$, the dissipation of the column is substantial enough that the system stays in the condensed state regardless of acceleration.

## 5.3 Experimental methods

Given the amount of factors that could influence packing, we have conducted three sets of experiments that aim to selectively reduce the impact of one or more effects. In the first set of experiments, we vertically vibrate 1000 Teflon and 1000 nylon spheres inside a spherical container made of aluminum. Teflon and nylon are two materials at the opposite ends of the triboelectric series and their propensity for charging oppositely when in contact is well documented [55, 177]. We will refer to these experimental conditions as the binary charging experiment. By choosing a metal as container material, a localized charge buildup on the container walls is prevented due to the materials high electric conductivity. Therefore, the electrostatic interaction with the wall should be limited to formation of mirror charges. The spherical shape of the container means that no crystal structure can be entirely compatible with the wall. This limits the influence the container walls play as possible nucleation site. As such, this experiment maximizes particle-particle charging while minimizing influences of the container.

In a second set of experiments, the aluminum sphere is filled with 2000 Teflon spheres and no nylon spheres so that for particle-particle contacts only same-material tribocharging occurs. While stochastic charge exchange will still occur and some spheres will charge positively while others charge negatively, the absence of nylon spheres will influence particle-particle charging. We will refer to this series of experiments as the same material charging experiment.

In the third set of experiments, we vertically vibrate 10.000 Teflon and 10.000 nylon spheres inside a PMMA container with square base and flat walls. With PMMA being an insulator, charge can build up freely on the walls and the low humidity conditions help to reduce charge dissipation. Therefore, charging against the walls can be expected to play a more significant role. Additionally, the flat walls form an ideal nucleation site for crystalline structures. We will refer to these experiments as the container dominated experiments.

All Teflon and nylon spheres used in this study have a diameter of $2\,\mathrm{mm}$ ($\pm 50\,\mu m$ according to the manufacturer, TIS Wälzkörpertechnologie). We use a low-force vibrating table of type LDS V721 made by Bruel & Kjaer to vibrate our sample. The vibrations are sine waves of amplitude $1\,\mathrm{mm}$ and frequency $23\,\mathrm{Hz}$, resulting in a peak acceleration of $\Gamma = 2.1\,g$ in vertical direction. These parameters were chosen based on a first experiment where at this frequency reorganizations in the packing were visible in the transparent PMMA container. For better comparability, we kept the shaking parameters constant and only varied the time which was spent shaking the sample. After

I: Sample        II: Vibrating table        III: Tomograph

a: 1,000 teflon
and 1,000 nylon
spheres in
spherical
container

b: 2,000 teflon
spheres in
spherical
container

c: 10,000 teflon
and 10,000
nylon spheres in
square base
container

$f = 23\,\mathrm{Hz}$, $A = 2\,\mathrm{mm}$, $t = 90\mathrm{Min}$
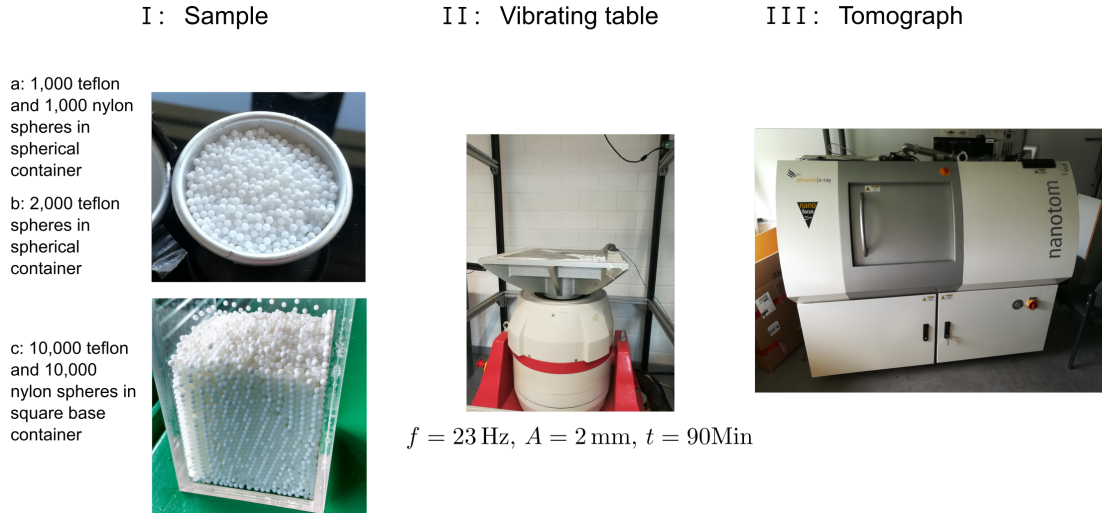
Figure 5.4: From left to right we see the spherical aluminum container filled with 2000 Teflon spheres (top) and the PMMA container filled with 10000 Teflon and 10000 nylon spheres (bottom), the vibrating table and the tomograph.

shaking, the sample is carefully removed from the vibrating table and a tomogram is recorded using a phoenix nanotom $\mu$CT system.

The devices used at each of the experimental steps are shown in figure 5.4. To measure the distribution of charges carried by spheres in the binary charging and same-material charging experiments, the vibration procedure is followed as described above but instead of recording a tomogram, the spherical container is opened and spheres are extracted one at a time using tweezers. By dropping the spheres individually into a Faraday cup connected to an electrometer. The charge distribution is calculated from the electrometer signal as described in section 4.7. We will provide an overview on the metrics used to describe the packing structure and provide additional details on the scanning procedure, sphere detection and implementation of the data analysis in section 5.7.2.

The methods we use for quantifying ordering in the packings are the radial distribution function $g(r)$ and the bond orientational parameters $q_4$ and $q_6$. The pair correlation function [178] $g(r)$ which can be used to describe simulated [179] or experimental [180, 181] hard-sphere systems gives the density of sphere centers a distance $r$ away from a test sphere (see also appendix 5.7.2:

$$g(r, \Delta r) = \frac{\langle N(r + \Delta r) - N(r) \rangle}{V_{\text{shell}}} \tag{v--1}$$

| Structure | $q4$ | $q6$ | Symbol in graphs |
|:---------:|:----:|:----:|:----------------:|
| HCP | 0.097 | 0.48 | ○ |
| FCC | 0.19 | 0.57 | □ |
| BCC | 0.51 | 0.63 | ◇ |

Table 5.2: Expected $q4$ and $q6$ values for the three most common crystal structures.

Since no angle is used for the calculation, $g(r)$ depends on the distances encountered in the sample alone. $g(r)$ is averaged over all spheres in the packing. For monodisperse spheres we expect to find a sharp peak at $r = d$, though this peak is broadened by particle polydispersity and inaccuracies in the image processing. The shape of the first peak can be used to accurately determine the mean particle diameter as well as the global contact number. In amorphous, monodisperse packings of spheres, we additionally expect to find a peak at $r = \sqrt{3}d$ and at $r = 2d$ [140, 147, 180, 182]. These peaks are a sign of local ordering which can occur even if no long-range order is present. For perfectly crystalline packings, $g(r)$ is a number of delta function corresponding to the distances found in the structure and $g(r)$ is 0 elsewhere. For binary mixtures, it is possible to discriminate between the material combinations and split $g(r)$ up into separate distributions according to the materials involved. This can for example be used to show charge ordering in binary liquids [179].

 The bond orientational parameters $q_4$ and $q_6$ are sensitive to periodicity in the orientations between neighboring spheres [183]. $q_l$ for any sphere in the packing is calculated according to:

$$q_l = \sqrt{\frac{4\pi}{2l+1} \sum_{m=-l}^{l} \left| \frac{1}{Z_l} \sum_{j=1}^{Z_l} Y_l^m[\theta(\mathbf{x_j}), \phi(\mathbf{x_j})] \right|^2}. \tag{v-2}$$

with $Z_l$ the number of neighbors of the test sphere and $Y_l^m$ the spherical harmonics functions. The neighbors considered for the calculation of the bond orientational parameters are chosen based on a threshold distance between spheres. The threshold is chosen so that the average number of neighbors for all spheres in the packing matches the global contact number as determined using the fit to the first $g(r)$ peak (for details see appendix (5.7.2). We can determine a value of $q_4$ and $q_6$ for every sphere in the packing. For amorphous packings, both $q4$ and $q6$ have been found to be normally distributed [183]. For perfectly crystalline packings, a certain value for $q4$ and $q6$ unique to the structure as provided in table 5.2 is expected.
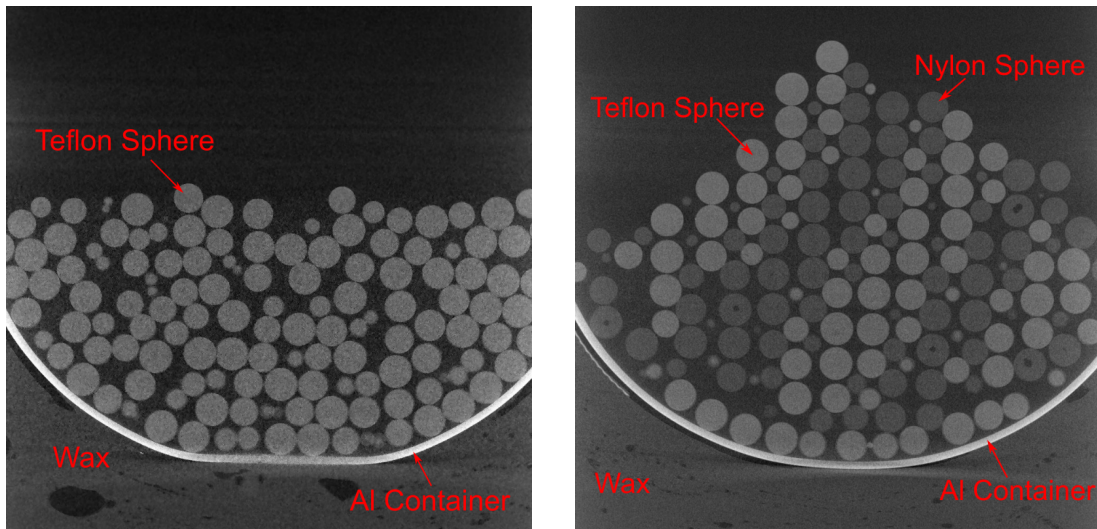
(a) Same material charging experiment.    (b) Binary charging experiment.

Figure 5.5: Slices through tomograms for the same material (5.5a) and the binary charging (5.5b) experiment where each sample was shaken for 90 minutes. In both images, gravity is pointing downward. The outline of the container sphere is also visible in the images. For the same-material charging case, the bulk of the sample shows no clear signs of ordering while a regular pattern can be seen a few particle layers from the container walls. In the binary charging sample, there is a regular pattern visible in the bulk of the sample which is incompatible with the arrangement of spheres close to the container walls.

## 5.4 RESULTS

Our experiments show that for identical preparation and shaking procedure, the applied protocols lead to significantly different packings in terms of achieved contact number, packing fraction and local ordering. We will first look at the influence of inter-particle charging by comparing the Teflon-nylon system with the pure nylon system.

### 5.4.1 EFFECT OF BINARY OR SAME-MATERIAL INTER-PARTICLE CHARGING.

There is no obvious ordering in the bulk for the same-material charging case, while for the binary charging case there is visible ordering (see fig. 5.5). We evaluate $g(r)$ in the systems to better quantify the degree of ordering.

$g(r)$ for the same-material 5.6a and the binary 5.6b charging case are shown in
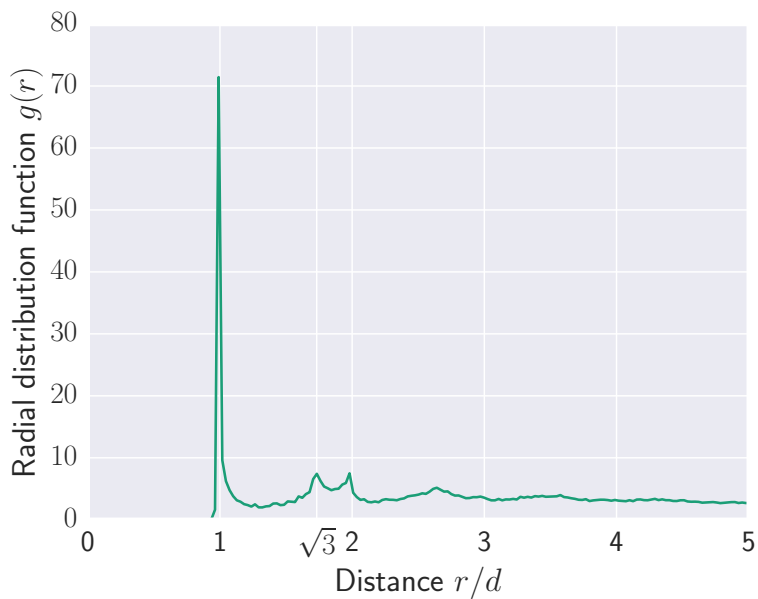
(a) Same material charging experiment.
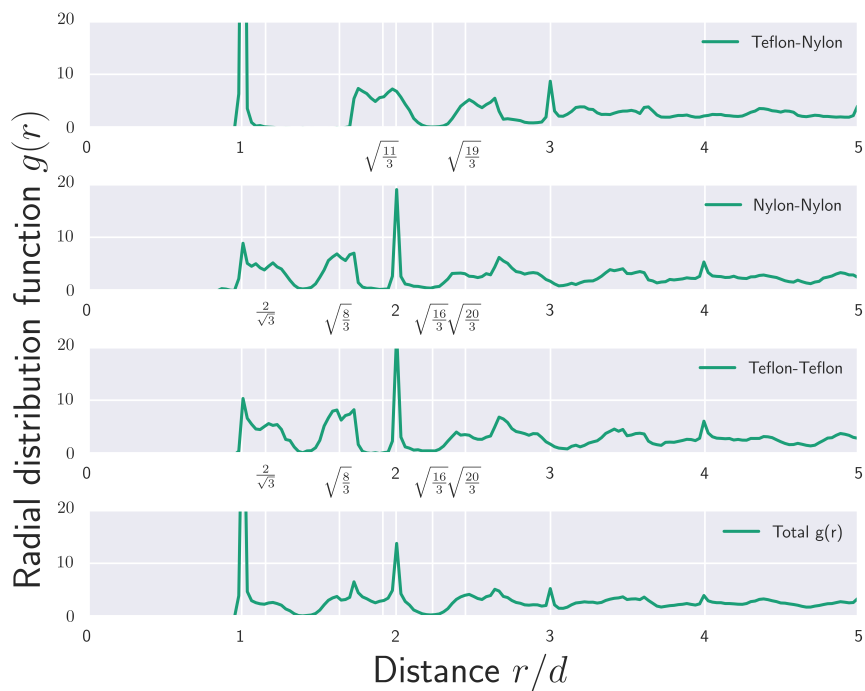


(b) Binary charging experiment.

Figure 5.6: Partial radial distribution functions for the same material and binary charging experiment. Markers on the x axis of fig. 5.6a indicate expected peaks for an amorphous packing while those in fig. 5.6b are expected peak locations up to $r = 3$ for a BCC crystal.

(a) Same material charging experiment.

(b) Binary charging experiment.
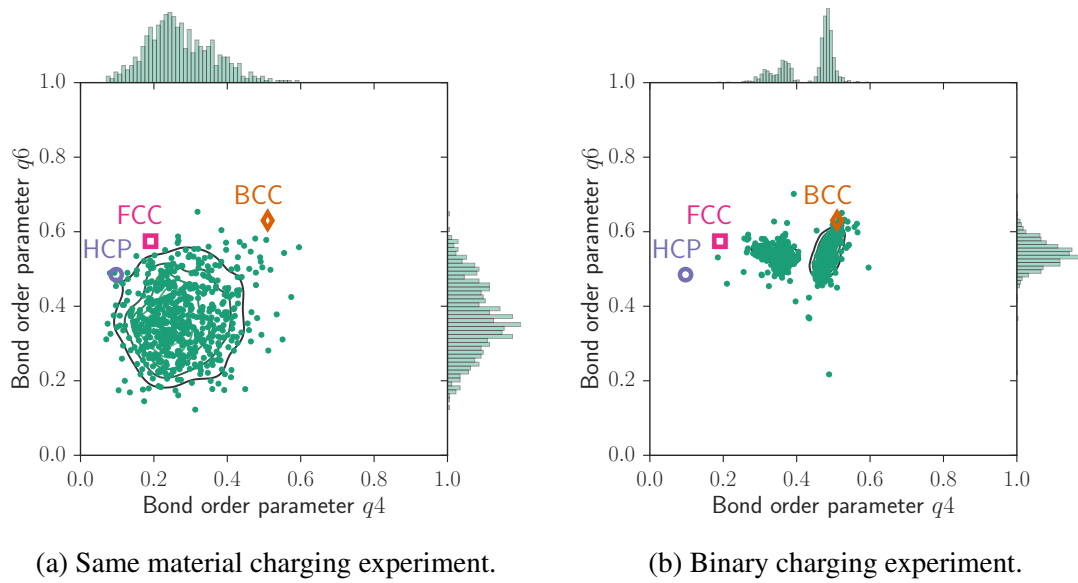
Figure 5.7: Bond orientational parameters $q4/q6$ for all spheres inside the packings that resulted after 90 minutes of vertical vibrations. In the same-material charging case, the data is scattered and no crystal structure is clearly favored. For the binary charging case, most cells are closest to ideal BCC.

figure 5.6. For the packing from the same-material experiment, there are peaks visible at $r = 1d, = \sqrt{3}d$ and $r = 2d$, as is expected in an amorphous packing. In particular, there are no peaks for higher $r$, which is where long-range order would be observable. We can determine a separate $g(r)$ for each of the material combinations possible in the binary charging experiment by differentiating between Teflon and nylon spheres, as shown in 5.6b. We can see that the packing from the binary charging experiment shows more distinct peaks. The peak locations roughly match those encountered in a BCC crystal (see markers on the x-axis), although many of the peaks are broadened. There are peaks visible up to at least $r = 4d$, meaning that there are particle-particle correlations for higher distances than in the same-material charging experiment. In the binary charging experiment, the $g(r)$ for Teflon-nylon distances differs qualitatively from that of nylon-nylon or Teflon-Teflon distances.

The bond orientational order parameters for the same-material charging experiment and the binary charging experiment are shown in figure 5.7. In the same-material charging experiment, there is greater spread in the data and the densest region is not close to any of the crystalline points, both of which are features encountered in amorphous packings. In the binary charging experiment, the densest region is close to the

135
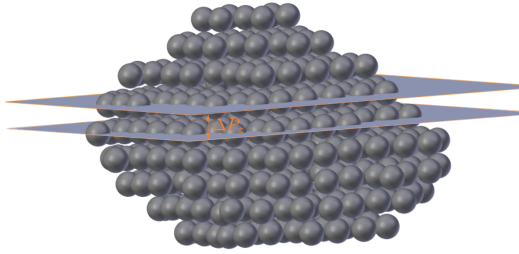
(a) Illustration showing the distance between two nylon planes with a distance $\Delta P_z$.
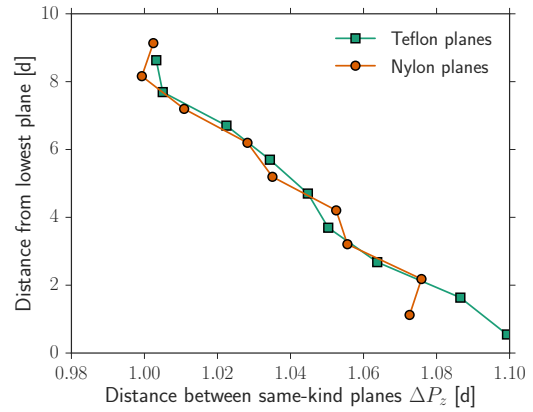
(b) Distance $\Delta P_z$ between planes of identical material in the z direction as a function of height in the sample.

Figure 5.8: We determine the distance between two planes of the same material in the binary charging experiment as illustrated in 5.8a. The plane distance $\Delta P_z$ decreases with increasing height in the sample. The value is closest to the value expected in a BCC crystal at the bottom of the sample.

expected value for an ideal BCC, although there is noticeable spread in the data, indicating deviations from perfect BCC.

To analyze the deviations of the packing structure in the binary charging experiment compared to a perfect BCC lattice, we determine the distance between neighboring planes consisting of the same material as a function of height in the sample. In a perfect BCC structure, this plane distance is $\Delta P_z = 2/\sqrt{3} \approx 1.15$ and corresponds to the first peak in $g(r)$ for nylon-nylon or Teflon-Teflon distances in figure 5.6b. A 3D rendering of the packing from the binary charging experiment is shown in figure 5.8a but only the nylon spheres are rendered. What is also shown is two planes fitted to a layer of nylon particles each.

Figure 5.8b shows the distance of each fitted XY-plane to the next highest plane of the same material kind as a function of the height in the sample $z$. The plane fits show that the planes are oriented at an angle of roughly $6°$ to the z axis. There is a systematic decrease of the inter-plane distance $\Delta P_z$ with the height within the sample. We can see that the planes towards the bottom of the sample are closer to the ideal BCC value than those at the top. The trend appears to be identical for both nylon planes and Teflon planes. This is further discussed in section 5.4.3 and 5.5.

(a) Slice through the entire packing.

(b) Slice through bulk region.

(c) Slice through wall region.
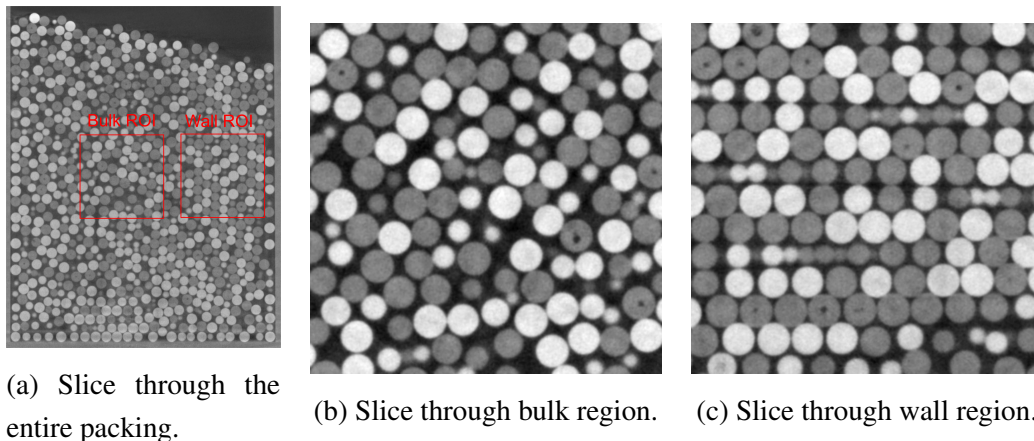
Figure 5.9: Slices through the tomograph of the container-dominated experiment. Figure 5.9a shows an overview of the entire packing, while 5.9b and 5.9c show slices through the bulk and the wall region respectively. The locations of the regions of interest are indicated in figure 5.9a (see color version)

### 5.4.2 INFLUENCE OF CONTAINER WALLS

For the container dominated experiment, we have separately analyzed two smaller regions, one close to the wall and one in the middle of the packing (see figure 5.9). The radial distribution functions for the container dominated experiment in the bulk region as shown in figure 5.10 exhibit no peaks other than at $r = 1d$, $r = \sqrt{3}d$ and $r = 2d$. $g(r)$ near the wall is shown in figure 5.10b and here we can see sharp peaks even for distances of at least $r = 5d$. In both subvolumes, there is no qualitative difference between the distributions plotted for different material combinations.

The bond orientational order parameters for the bulk region of the container experiment are shown in figure 5.11a. There is a large spread in the data and no obvious clustering around any of the potentially expected crystalline structures. Near the wall, $q4$ and $q6$ are distributed around the HCP and FCC spots, although the distributions are broad so that no single crystal structure can be identified.

All the packing fractions and contact numbers by material type are given in table 5.3. The packing fraction in the binary charging experiment is very close to the packing fraction in ideal BCC $\varphi_{BCC} = 0.68$. The packing fractions are close to $\varphi_{RCP}$ for the same-material experiment and for the bulk region of the container experiment.
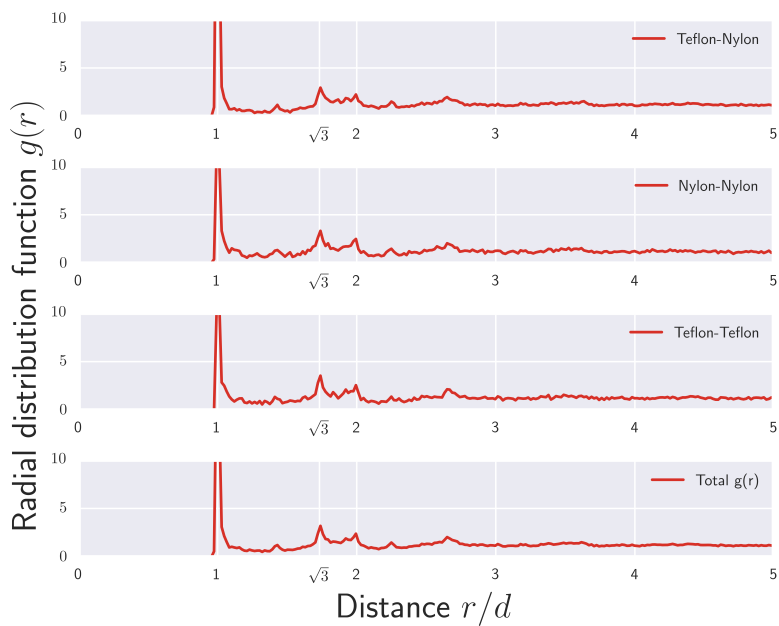
(a) Bulk of container-dominated experiment.
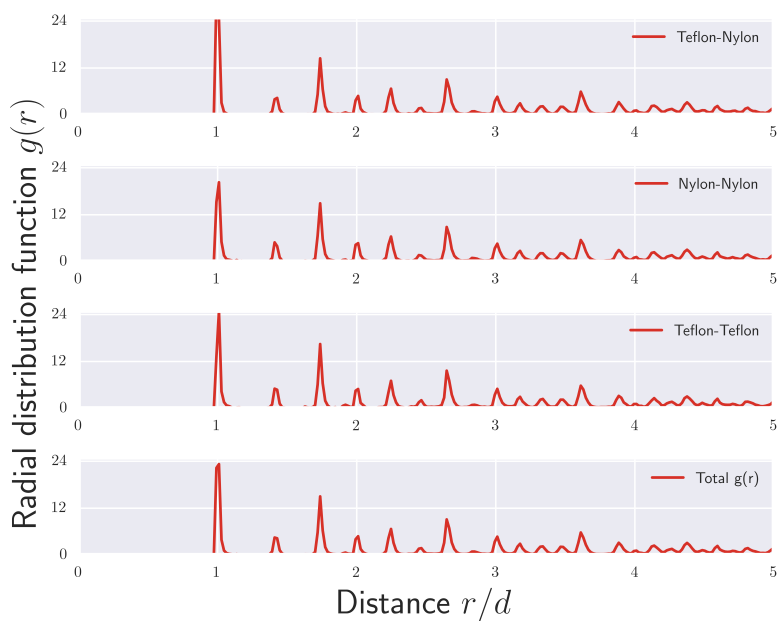


(b) Near wall of container-dominated experiment.

Figure 5.10: Partial radial distribution $g(r)$ for the container dominated experiment. The top panel in each figure shows $g(r)$ only counting the Teflon-nylon distances, while the second and third panels show $g_{NN}(r)$ with only nylon-nylon and $g_{TT}(r)$ with only Teflon-Teflon distances counted. The bottom panel of each figure shows the total $g(r)$ with all distances counted.
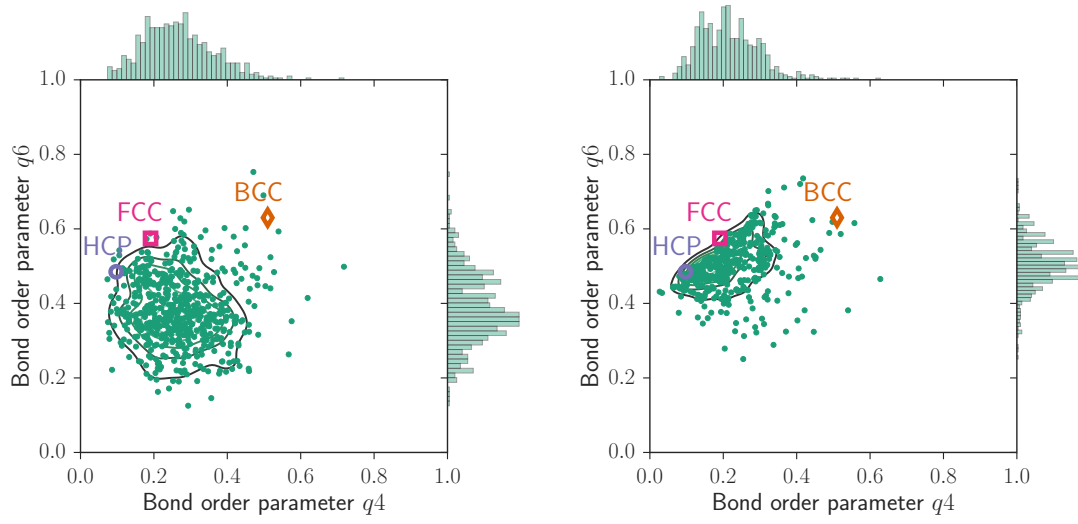
(a) Container experiment in the bulk region.

(b) Container experiment near the wall.

Figure 5.11: Bond orientational parameters $q4/q6$ for every sphere in the bulk 5.11a and the wall 5.11a subvolume of the container dominated experiment.

| Experiment | $\varphi_{\text{global}}$ | $Z_{\text{global}}$ | $Z_{TT}$ | $Z_{NN}$ | $Z_{TN}$ | $N_T/(N_T+N_N)$ |
|---|---|---|---|---|---|---|
| Binary charging | 0.678 | 6.7 | 0.5 | 0.3 | 6.5 | 0.50 |
| Same-material charging | 0.645 | 6.7 | - | - | - | 1 |
| Container – bulk | 0.632 | 6.0 | 1.9 | 1.7 | 4.3 | 0.48 |
| Container – wall | 0.698 | 7.5 | 2.8 | 2.6 | 5.1 | 0.46 |

Table 5.3: Packing fractions, contact numbers and fraction of Teflon spheres in the observed volumes for the experiments.

(a) Same-material charging experiment.

(b) Binary charging experiment.
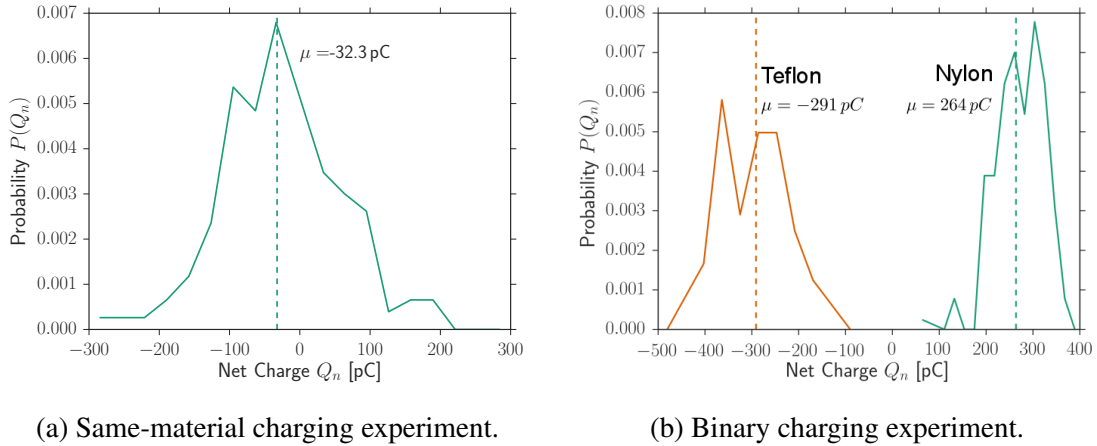
Figure 5.12: Charge distributions measured with the tweezer method for the same-material (fig. 5.12a) and the binary (fig. 5.12b) charging experiment.

### 5.4.3 CHARGING EFFECTS

We have measured the charge distribution of spheres in the binary charging and same-material charging experiments to quantify the effects that charging might play in our experiments. The charge distribution in the same-material charging experiment is shown in figure 5.12a. The distribution has a mean of $\mu = -32.3\,pC$ and a width of $\sigma = 90\,pC$. Although the mean charge is negative, about one third of spheres carried a positive charge. The skewness and excess kurtosis for the measured distribution are 0.144 and 0.02, respectively.

The charge distribution of the Teflon and nylon spheres in the binary charging experiment are shown in figure 5.12b. The charge measured on all Teflon spheres was negative while that of every nylon sphere was positive. The mean charge of the Teflon spheres was $-291\,pC$ and that of the nylon spheres was $264\,pC$.

Given the potential influence of charging on our experiments, it is necessary to consider the effects that ionizing radiation in the tomograph might have on the charges in our packing. We performed an experiment where we shake a set of monodisperse 1000 Teflon and 1000 nylon spheres in a polystyrene container using a vortex mixer and measure the charges on the spheres. The packing is placed in the tomograph and radiated for one hour at the usual intensities used for the other scans. After an hour of radiation exposure, we again measure the charge on the beads using the tweezer extraction method. The results of this experiment are shown in figure 5.13. The distributions shifted closer to 0 and the absolute mean of the distribution for Teflon is reduced to roughly a third of the original value and for nylon the mean reduces to a
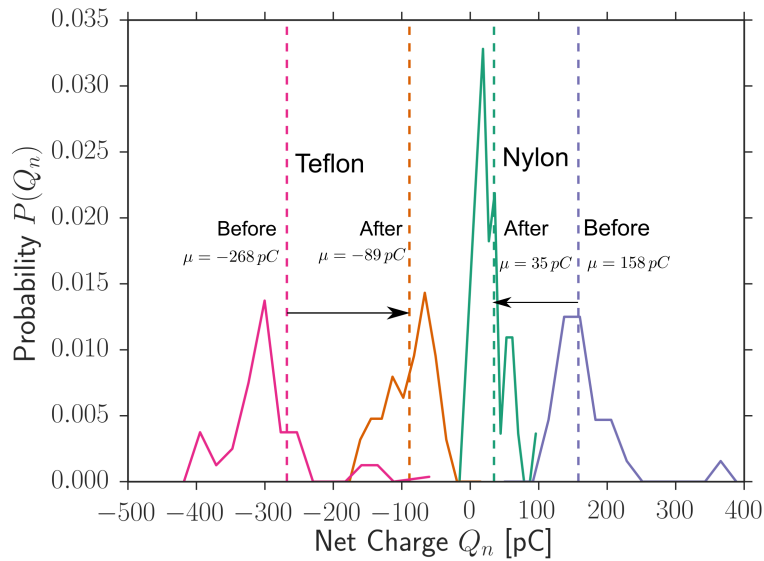
Figure 5.13: Histogram of the charges measured before and after an hour long exposure to X-ray radiation.

quarter after radiation.

To check if the measured discharging effect of the X-rays during scanning might influence the packing structure in our experiments, we repeated the binary charging experiment with 90 minutes of vertical vibrations applied. The radiogram for this packing is shown in figure 5.14a. We then recorded radiograms in the same projection direction in 5 minute intervals. By subtracting each radiogram from the one recored 5 minutes earlier, we can detect spheres that moved in the time interval. A sphere moving from point A in the radiogram at 0 minutes to point B in the radiogram at 5 minutes will show up bright at point A and dark at point B in the difference image. A sphere that moved by less than its diameter will create a bright and dark area proportional to the displacement. Figure 5.14b shows the difference image between the radiogram recorded at 5 minutes and 0 minutes of radiation. One sphere which moved by more than its diameter is visible. This could for example be caused by a sphere stuck to the container by electrostatic forces. In the intervals from 20 to 25 and from 25 to 30 minutes, there are multiple sub-diameter sphere movements visible that appear to be close together in the difference image. Figure 5.15 shows the cumulative of the percentage of pixels in each of the difference images that are more than 4 standard deviations brighter than the mean gray value of the picture. This value will increase with increasing movement in the sample. The first data point in this graph corresponds
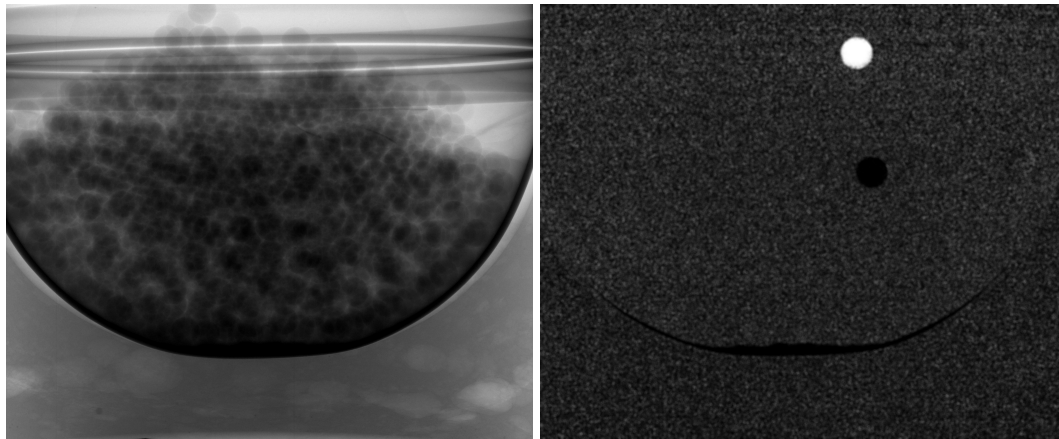
(a) Radiogram before radiation.

(b) Difference image after 5 Mins.
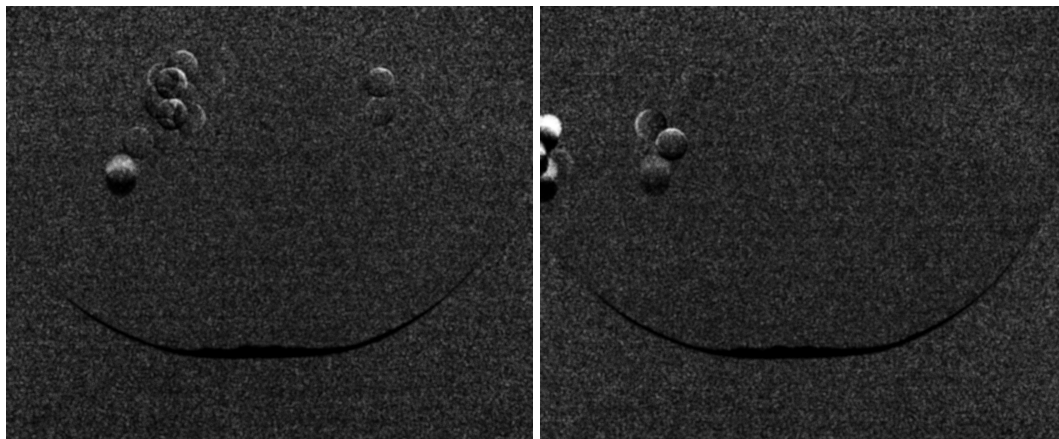
(c) Difference image after 25 Mins.

(d) Difference image after 30 Mins.

Figure 5.14: (a): Radiogram of the packing before long exposure to X-rays. (b)-(d): pixel by pixel subtraction of the gray values of the radiogram recorded at the specified time and the gray values in the radiogram in fig. 5.14a.
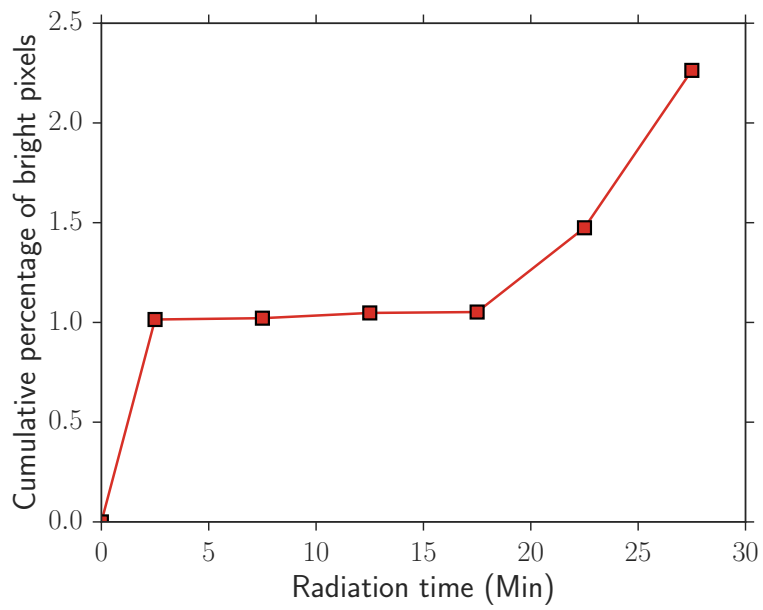
Figure 5.15: Cumulative of the percentage of pixels in the subtracted images that are at least 4 standard deviations brighter than the mean gray value.

to the difference image shown in figure 5.14b.

## 5.5 DISCUSSION

The measurements presented in 5.4 show that quite significant differences in the packing structure of monodisperse spheres can be achieved simply by changing the materials involved. For the same material charging where only teflon spheres were used no long range ordering as quantified by $g(r)$ occured. In addition, the bond orientational order parameters are exactly as we would expect from an amorphous packing. In the binary charging experiment where an equal number mixture of teflon and nylon spheres was used a clear ordering according to the material occurred and a structure similar to BCC was formed. We showed that the inter-plane distances in the binary charging experiment changed systematically with height in the sample, suggesting that deformations of the BCC cells are due to the influence of gravity. The deviations from ideal BCC are smallest at the bottom of the sample and increase with height. A possible explanation for this could be that near the bottom of the sample, the weight of the spheres above can be effectively transferred to the container walls, granting mechanical stability. In a BCC structure as it is oriented in our experiments, the force network does not allow direct force transfer in the negative z direction or any direction perpendicular to it, meaning the only stabilization against forces can come from the four contacts oriented at $45\,^{\circ}$ to the gravitational pull. The deformations of the BCC cells might therefore be a response to gravity induced compression.

There is no way to tell when this deformation occurred. The first scenario is that the crystal could have gotten deformed already while applying the vertical vibrations. The second scenario is that when stopping the vertical vibrations, the packing relaxed into the structure as we see it now. The third scenario is that the deformations occurred after radiation with X-rays. The results presented in figure 5.13 suggest that movement of spheres was present in response to the ionizing radiation. The motion appeared to happen in localized regions, suggesting that spheres moved collectively, i.e. spheres on top moved in response to displacements below them. Motion in response to a reduction of charging indicates that charging helped to maintain the structure as it appeared in the first place. Clearly, there were spheres being held in their place by help of coulombic interactions. Since it is not possible to make a scan without applying the radiation, we cannot check the whole structure before and after radiation exposure to exactly quantify the influence that charges played in maintaining the mechanical stability of the packing. However, we can provide estimates of the relative importance based on our charge measurements. The average charges on teflon and nylon spheres was $Q_T = -291\,pC$ and $Q_N = 264\,pC$. If we assume that this charge is equally distributed

on each sphere and we assume purely coulombic interaction between two spheres in contact, we get a force of $F_q = \frac{Q_T Q_N}{4\pi\varepsilon_0 d^2} = 173\,\mu N$. In comparison, the gravitational force on the (heavier) teflon spheres is $F_g = mg = 9.06\text{mg}\,9.81 m/s^2 = 90\,\mu N$, showing that the coulombic pair forces are on average about twice as high as the gravitational forces acting on a single sphere.

As introduced in section 5.2, Cademartiri et al. measured a charge of $|Q| > 500\,pC$ as the threshold charge for the formation of densely packed charge-ordered packings of 3mm spheres vibrated in a disc [170]. For spheres with a diameter of 2mm as used in our experiments, the same charge density would correspond to a total charge on the spheres of 300 $pC$, a value quite similar to the one we measure in our experiments.

The mean charge density of the teflon spheres assuming equal coverage of the entire sphere corresponds to a surface charge density of $145\,e^-(\mu m)^{-2}$, a value comparable to the density measured in our single contact tribocharging experiments [16]. The mean charge for the teflon spheres and the nylon spheres is not equal, which can have two reasons: first, the container wall could be carrying some charge, meaning that charge neutrality can only be expected when considering the entire system. Second, it could be an inaccuracy of the measurement method employed: before the charge can be measured, the sphere must be picked up with a tweezer. An interaction with the tweezers either while picking up or separating from the tweezers could change the measured charges and there is no way to know if this would affect teflon or nylon spheres the same way.

If we multiply the mean charge measured in the same-material charging experiment by the total amount of spheres in our system, we get a charge of $Q_{\text{total}} = 65.6\,nC$.

This value can be compared to the $Q_{\text{total}} \approx 100\,nC$ that Schella et al. [55] measured using a contact-less method to determine the total charge of 2000 teflon spheres agitated in a metal container. This could be interpreted as a sign that picking up the spheres with tweezers does not change the mean charge significantly. The distributions we measure in the same-charging experiment had a skew of 0.144 and an excess kurtosis of 0.02, indicating that the distributions do not differ significantly from a Gaussian distribution. In this regard, the distributions are different to the ones measured in our study on single and multiple collisions [16], where the measured charge distributions were fat-tailed and asymmetric. These contradicting results could be due to measurement inaccuracies of the tweezer extraction method and the relatively small statistics ($N \approx 150$). An alternative explanation would be that for a sufficiently large number of collisions, the distribution becomes a Gaussian distribution in accordance with the central limit theorem. Our experiments show that not only the material of the constituent

spheres but also container material and geometry play a crucial role in determining the packing structure. In the container experiments, the same spheres were used as in the binary charging experiment and yet the resulting structures were completely different. In the container dominated experiment, the center of the packing remained amorphous while the regions near the wall showed a mixture of FCC and HCP polycrystalline structures. In both subvolumes, the shape of $g(r)$ does not change with material pairing, indicating that no ordering by material type occurs.

## 5.6  CONCLUSIONS

We subjected a two component granular medium of monodisperse teflon and nylon spheres to vertical vibrations and measured the resulting packing structure. We found that the packing structure is not just influenced but determined by electrostatic interactions caused by tribocharging. If the influence of container walls is minimized, a CsCl like structure emerges with systematic deviations from an ideal BCC structure that can be explained by gravitational compression. The crystal structure is most pronounced in the bulk of the sample and the sphere layers close to the wall appear disordered. A reference system that was prepared in an identical fashion but consists of only teflon spheres remains amorphous when vertically vibrated. In an identical two component system where charging against the container walls is not suppressed and where the container wall is commensurate to crystalline structures, we find crystallization in HCP and FCC polycrystalline structures close to the container walls and an amorphous structure emerges in the bulk.

## 5.7 Appendix

### 5.7.1 X-ray Computed Tomography

An invaluable tool for the detection of particle positions in a static granular packing is X-ray computed tomography (CT). The X-rays that a CT tomograph uses can penetrate most granular samples and therefore information about the entire bulk and not just the visible surface can be obtained. The intensity of the recored image largely depends on the attenuation of the material that the X-ray beam passed through. According to Beer-Lambert law [184, 185], the Intensity $I$ through a sample with $N$ components is given by:

$$I = I_0 e^{-\sum_{i=1}^{N} \sigma_i^s \int_0^l n_i(z) dz} \tag{v–3}$$

where $\sigma_i^s$ is the scattering cross-section of material $i$ and $n$ is the corresponding density along the path. An image recorded by this technique is called a radiogram. By recording multiple radiograms from different directions, it is possible to calculate the attenuation at every 3D point within the sample using an algorithm based on the Radon transform [186]. The generated information is in the form of gray values in a volume element commonly referred to as a voxel. The attenuation depends mostly on the energy of the incoming radiation and the material that is scanned. There are three ways in which matter interacts with X-rays at the energies used in out experiment:

1. **Compton Scattering:** This effect describes the inelastic scattering of light off essentially free charged particles. The effect is mostly independent of the atomic number for the energies used in our experiment.

2. **Thomson Scattering:** This effect describes elastic scattering of light off charged particles which occurs when the light wavelength is much greater than the particle wavelength.

3. **Photoelectric effect:** The absorption of a photon by an electron can only happen if an atom is present to balance the exchanged momentum. Therefore, the photoelectric effect causes the transition of a bound electron to an unbound electron. This leaves behind an ionized atom and is the cause for the X-ray's ionization potential. The photoelectric effect scales as $\sigma_{\text{photo}}^s \propto \frac{Z^n}{E^3}$ where $n \approx 4.5$ for light elements and $E$ is the photon energy.

In practice, the attenuation coefficients of compounds can be looked up in an online database like XCOM of the National Institute of Standards and Technology (NIST) [187].

(a) Attenuation curve for Teflon.

(b) Attenuation curve for Nylon.
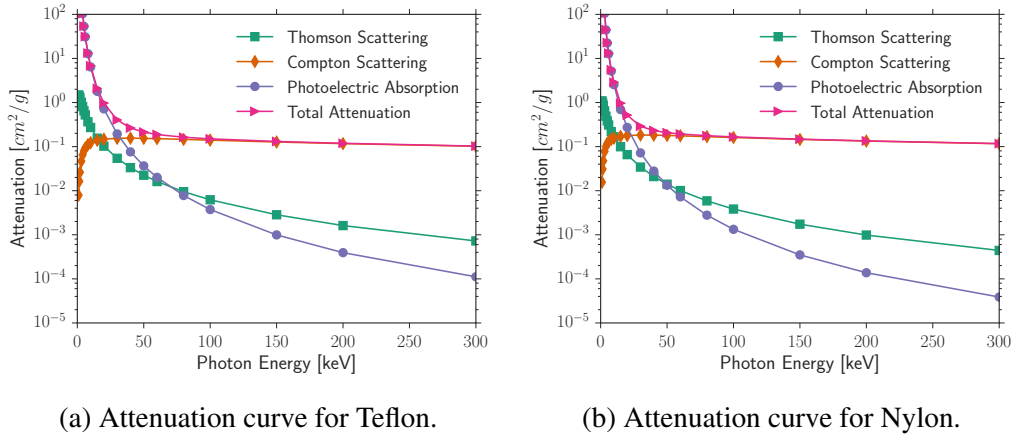
Figure 5.16: Attenuation curves for the materials used in our experiments.

The corresponding curves for Teflon and Nylon are shown in the figure 5.16. Given the similarity of the chemistry of both materials, it is obvious that any difference in attenuation is due to the higher density of Teflon.

A schematic showing the principle of operation of the tomograph is shown in figure 5.17. In our experiments, we used a pheonix Nanotom m CT system with an acceleration voltage of $U_0 = 90 \, \text{kV}$ and a current of $I_0 = 110 \, \mu\text{A}$. These parameters showed the best contrast between the two materials observed and air. We rotate the sample in 800 steps ($0.45°$ per step) and average over two recorded radiograms with $1000 \, ms$ exposure time per radiogram, resulting in a total measuring time of 54 minutes per scan. The voxel size at the chosen parameters is $31.7 \mu m$, giving 63 voxels per diameter of the 2mm spheres.

## 5.7.2 DETAILS REGARDING THE DATA ANALYSIS

The first goal is to extract particle positions as precisely from the tomography data as possible. The C++ code that was used for this is a modified version of the work of Weis and Schröter [188]. The steps involved are:

1. **Bilateral filtering:** A bilateral filter is used to smooth the image while maintaining edges [189]. This is crucial for maintaining voxels on the surface of the spheres. The bilateral filter replaces each voxel by a weighted average intensity of nearby voxels. The weighting function used was a Gaussian distribution. The goal here is to achieve a uniform gray value corresponding to each sphere material that can be discriminated against air.

148
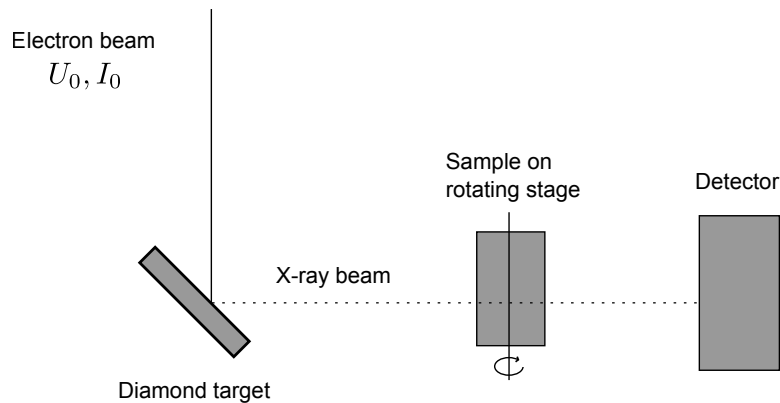
Figure 5.17: Working principle of a X-ray tomograph. An electron beam with current $I_0$ and energy $U_0 e$ per electron is accelerated against a diamond target. During the rapid deceleration of the electrons, X-rays from Bremsstrahlung are radiated towards the sample on a rotating stage. After passing through the sample, the X-rays are measures by a detector.

2. **Binarization:** The goal here is to assign a label to each voxel identifying it as one of the materials based on its gray value. For this purpose, we use the OpenCV [190] implementation of kmeans clustering [191, 192]. The algorithm works by dividing provided data into $k$ groups so that the variance within each group is minimized. By providing the gray values as data and setting $k = 3$, we obtain a label corresponding to the highest (Teflon), the middle (nylon) and the lowest (air) gray value.

3. **Void filling:** Due to the manufacturing process, the nylon beads often have holes inside of them which are visible in the tomograms. Since these voxels would obstruct the centroid calculation, they are removed using the Hoshen Kopelman algorithm [193]. The basic principle is that connected air-type voxels are detected. The biggest of these connected structures will be the air between particles while all other connected air structures come from holes in the spheres. Therefore, the biggest connected structure is set to air while all other connected air structures are set to the material type surrounding them.

4. **Particle Identification:** We construct a Euclidian distance map [194] that assigns each voxel the distance to the next air-type voxel. For a sphere this assigned value thus corresponds to the distance of the voxel to the sphere surface. By setting an erosion cutoff value, neighbouring spheres, whose voxels may

have been overlapping, can be separated and labeled. Afterwards, the eroded voxels are reintroduced and labeled according to their distance to the closest sphere center. Finally, the mean position of every voxel assigned to one sphere is used to calculate the exact sphere centroid.

$g(r)$ describes the average density of sphere centroids a distance $r$ away from a test sphere. A discretized version can be stated as:

$$g(r, \Delta r) = \frac{\langle N(r + \Delta r) - N(r) \rangle}{V_{\text{shell}}}, \qquad \text{(v–4)}$$

where the brackets denote an average over all spheres and $V_{\text{shell}} = 4\pi r^2 \Delta r$ is the volume of the sphere shell as long as $r$ is small enough so that the sphere shell does not reach the edge of the container. In order to correct for this effect, there are three options. The first option is to restrict the search for particles to regions not intersecting the container. This restricts the statistics gathered for longer distances and is thus an undesirable option. The second option is to mathematically calculate the partial sphere shell still inside the container [195, 196]. The option we chose is to calculate an unnormalized $g(r)$ for a box filled with randomly assigned particle positions and divide by this reference value:

$$g(r, \Delta r) = \frac{\langle N(r + \Delta r) - N(r) \rangle}{\langle N(r + \Delta r) - N(r) \rangle_0}, \qquad \text{(v–5)}$$

where the subscript 0 indicates the simulation result.

We fit a Gaussian function to the first peak of $g(r)$ to determine the best estimate for the particle diameter $D_p$ and the uncertainty arising from sphere polydispersity and measurement accuracy $\sigma$. We split $g(r)$ up according to material pairings where the partial radial distribution function $g_{AB}(r)$ describes the density of spheres of material type $B$ to a test sphere of material $A$. We fit to the cumulative partial radial distribution function $\int_0^D g_{AB}(r)dr$ to a function of the form [188, 197, 198]:

$$n_{AB}(D; D_p, \sigma, Z_{AB}, m) = \frac{Z_{AB}}{\sqrt{2\pi}\sigma} \int_0^D \exp\left(-\frac{(r - D_p)^2}{2\sigma^2}\right) dr + \Theta(r - D_p)m(r - D_p)$$

$$\text{(v–6)}$$

with $Z_{AB}$ the estimated number of contacts between materials A and B and $m$ a fit parameter. This function essentially assumes a normal distribution about the actually contacting particles at $r = d$ and then a uniform distribution of "almost touching" distances at $r \gtrsim d$. For the purpose of determining sphere contacts, we set the threshold
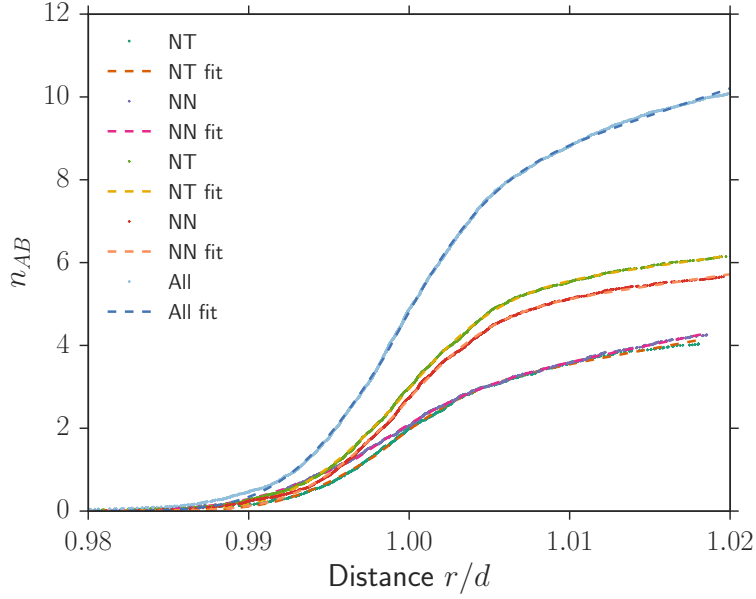
Figure 5.18: Example fit of equation (V–6) to experimental data in the container experiment near the wall. In the legend AB refers to spheres made of material A contacting spheres made of material B.

to the value which reproduces the global contact number determined by the fit to the cumulative $g(r)$. An example of a fit according to equation (V–6) is shown in figure 5.18. The agreement with the data is good.

The bond orientational order parameter $\mathbf{q}_l^m$ for a single sphere with $Z_l$ neighbors is defined as

$$\mathbf{q}_l^m = \frac{1}{Z_l} \sum_{j=1}^{Z_l} Y_l^m[\theta(\mathbf{x_j}), \phi(\mathbf{x_j})] \qquad m = -l, -l+1, \ldots, l \qquad (\text{V–7})$$

Here, $\mathbf{x}$ is the vector pointing to each of the spheres neighbors and $Y_l^m$ are the spherical harmonic functions $Y_l^m(\theta, \phi) = \sqrt{\frac{(2l+1)(l-m)!}{4\pi(l+m)!}} e^{im\theta} P_l^m(\cos(\phi))$ with $P_l^m$ the associated Legendre polynomial. In this work, we use the rotation invariant form given by:

$$q_l = \sqrt{\frac{4\pi}{2l+1} \sum_{m=-l}^{l} |\mathbf{q}_l^m|^2}. \qquad (\text{V–8})$$

The two parameters we are particularly interested in are $q_4$ for $l = 4$ and $q_6$ for $l = 6$, which we determine for every sphere.

# Bibliography

[16] J. Haeberle, A. Schella, M. Sperl, M. Schröter, and P. Born. "Double origin of stochastic granular tribocharging". *Soft Matter* 14.24 (2018), pp. 4987–4995.

[45] M. Muthuswamy and A. Tordesillas. "How do interparticle contact friction, packing density and degree of polydispersity affect force propagation in particulate assemblies?" *Journal of Statistical Mechanics: Theory and Experiment* 2006.9 (Sept. 7, 2006), P09003–P09003.

[55] A. Schella, S. Herminghaus, and M. Schröter. "Influence of humidity on triboelectric charging and segregation in shaken granular media". *Soft Matter* 13.2 (2017), pp. 394–401.

[68] M. Schröter, D. I. Goldman, and H. L. Swinney. "Stationary state volume fluctuations in a granular medium". *Physical Review E* 71.3 (Mar. 30, 2005).

[78] F. Rietz, C. Radin, H. L. Swinney, and M. Schröter. "Nucleation in Sheared Granular Matter". *Physical Review Letters* 120.5 (Feb. 2, 2018), p. 055701.

[139] G. Y. Onoda and E. G. Liniger. "Random loose packings of uniform spheres and the dilatancy onset". *Physical Review Letters* 64.22 (May 28, 1990), pp. 2727–2730.

[140] G. D. Scott. "Packing of Spheres: Packing of Equal Spheres". *Nature* 188.4754 (Dec. 1960), pp. 908–909.

[141] J. G. Berryman. "Random close packing of hard spheres and disks". *Physical Review A* 27.2 (Feb. 1, 1983), pp. 1053–1061.

[142] A. V. Anikeenko and N. N. Medvedev. "Polytetrahedral Nature of the Dense Disordered Packings of Hard Spheres". *Physical Review Letters* 98.23 (June 8, 2007).

[143] J. B. Knight, C. G. Fandrich, C. N. Lau, H. M. Jaeger, and S. R. Nagel. "Density relaxation in a vibrated granular material". *Physical Review E* 51.5 (May 1, 1995), pp. 3957–3963.

[144] P. Richard, M. Nicodemi, R. Delannay, P. Ribière, and D. Bideau. "Slow relaxation and compaction of granular systems". *Nature Materials* 4.2 (Feb. 2005), pp. 121–128.

[145] S. R. Liber, S. Borohovich, A. V. Butenko, A. B. Schofield, and E. Sloutskin. "Dense colloidal fluids form denser amorphous sediments". *Proceedings of the National Academy of Sciences* 110.15 (Apr. 9, 2013), pp. 5769–5773.

[146] M. Hanifpour, N. Francois, S. M. Vaez Allaei, T. Senden, and M. Saadatfar. "Mechanical Characterization of Partially Crystallized Sphere Packings". *Physical Review Letters* 113.14 (Oct. 1, 2014), p. 148001.

[147] T. Aste, M. Saadatfar, and T. J. Senden. "Geometrical structure of disordered sphere packings". *Physical Review E* 71.6 (June 20, 2005), p. 061302.

[148] J. D. Bernal, K. R. Knight, and I. Cherry. "Growth of Crystals from Random Close Packing". *Nature* 202.4935 (May 1964), pp. 852–854.

[149] K. E. Daniels and R. P. Behringer. "Characterization of a freezing/melting transition in a vibrated and sheared granular medium". *Journal of Statistical Mechanics: Theory and Experiment* 2006.7 (July 31, 2006), P07018–P07018.

[150] O. Pouliquen, M. Nicolas, and P. D. Weidman. "Crystallization of non-Brownian Spheres under Horizontal Shaking". *Physical Review Letters* 79.19 (Nov. 10, 1997), pp. 3640–3643.

[151] Y. Nahmad-Molinari and J. C. Ruiz-Suárez. "Epitaxial Growth of Granular Single Crystals". *Physical Review Letters* 89.26 (Dec. 11, 2002).

[152] A. Panaitescu and A. Kudrolli. "Epitaxial growth of ordered and disordered granular sphere packings". *Physical Review E* 90.3 (Sept. 3, 2014).

[153] A. P. F. Atman, P. Brunet, J. Geng, G. Reydellet, G. Combe, P. Claudin, R. P. Behringer, and E. Clément. "Sensitivity of the stress response function to packing preparation". *Journal of Physics: Condensed Matter* 17.24 (2005), S2391.

[154] C. Goldenberg and I. Goldhirsch. "Small and large scale granular statics". *Granular Matter* 6.2 (2004), pp. 87–96.

[155] C. Goldenberg and I. Goldhirsch. "Effects of Friction and Disorder on the Quasi-Static Response of Granular Solids to a Localized Force". *Physical Review E* 77.4 (Apr. 8, 2008).

[156] N. W. Mueggenburg, H. M. Jaeger, and S. R. Nagel. "Stress Transmission through Three-Dimensional Ordered Granular Arrays". *Physical Review E* 66.3 (Sept. 23, 2002).

[157] M. J. Spannuth, N. W. Mueggenburg, H. M. Jaeger, and S. R. Nagel. "Stress transmission through three-dimensional granular crystals with stacking faults". *Granular Matter* 6.4 (2004), pp. 215–219.

[158] D. Frenkel. "Entropy-driven phase transitions". *Physica A: Statistical Mechanics and its Applications*. Proceedings of the 20th IUPAP International Conference on Statistical Physics 263.1 (Feb. 1, 1999), pp. 26–38.

[159] B. J. Alder and T. E. Wainwright. "Phase Transition for a Hard Sphere System". *The Journal of Chemical Physics* 27.5 (Nov. 1957), pp. 1208–1209.

[160] W. W. Wood and J. D. Jacobson. "Preliminary Results from a Recalculation of the Monte Carlo Equation of State of Hard Spheres". *The Journal of Chemical Physics* 27.5 (Nov. 1957), pp. 1207–1208.

[161] G. M. Whitesides and B. Grzybowski. "Self-Assembly at All Scales". *Science* 295.5564 (Mar. 29, 2002), pp. 2418–2421.

[162] H. Thomas, G. E. Morfill, V. Demmel, J. Goree, B. Feuerbacher, and D. Möhlmann. "Plasma Crystal: Coulomb Crystallization in a Dusty Plasma". *Physical Review Letters* 73.5 (Aug. 1, 1994), pp. 652–655.

[163] A. P. Nefedov, G. E. Morfill, V. E. Fortov, H. M. Thomas, H. Rothermel, Tanja Hagl, A. V. Ivlev, M. Zuzic, B. A. Klumov, A. M. Lipaev, V. I. Molotkov, O. F. Petrov, Y. P. Gidzenko, S. K. Krikalev, W. Shepherd, A. I. Ivanov, M. Roth, Horst Binnenbruck, J. A. Goree, and Y. P. Semenov. "PKE-Nefedov: plasma crystal experiments on the International Space Station". *New Journal of Physics* 5.1 (2003), p. 33.

[164] M. E. Leunissen, C. G. Christova, A.-P. Hynninen, C. P. Royall, A. I. Campbell, A. Imhof, M. Dijkstra, R. van Roij, and A. van Blaaderen. "Ionic colloidal crystals of oppositely charged particles". *Nature* 437.7056 (Sept. 2005), pp. 235–240.

[165] E. C. M. Vermolen, A. Kuijk, L. C. Filion, M. Hermes, J. H. J. Thijssen, M. Dijkstra, and A. van Blaaderen. "Fabrication of large binary colloidal crystals with a NaCl structure". *Proceedings of the National Academy of Sciences* 106.38 (Sept. 22, 2009), pp. 16063–16067.

[166] A. F. Holleman and E. Wiberg. *Holleman-Wiberg Lehrbuch der Anorganischen Chemie*. Walter de Gruyter, 1971.

[167] L. Pauling. "The Principles determining the Structure of Complex Ionic Crystals". *Journal of the American Chemical Society* 51.4 (Apr. 1929), pp. 1010–1026.

[168] M. Flórez, J. M. Recio, E. Francisco, M. A. Blanco, and A. M. Pendás. "First-principles study of the rocksalt–cesium chloride relative phase stability in alkali halides". *Physical Review B* 66.14 (Oct. 31, 2002), p. 144112.

[169] M. Watanabe, M. Tokonami, and N. Morimoto. "The transition mechanism between the CsCl-type and NaCl-type structures in CsCl". *Acta Crystallographica Section A: Crystal Physics, Diffraction, Theoretical and General Crystallography* 33.2 (Mar. 1, 1977), pp. 294–298.

[170] R. Cademartiri, C. A. Stan, V. M. Tran, E. Wu, L. Friar, D. Vulis, L. W. Clark, S. Tricard, and G. M. Whitesides. "A simple two-dimensional model system to study electrostatic-self-assembly". *Soft Matter* 8.38 (2012), p. 9771.

[171] B. A. Grzybowski, A. Winkleman, J. A. Wiles, Y. Brumer, and G. M. Whitesides. "Electrostatic self-assembly of macroscopic crystals using contact electrification". *Nature Materials* 2.4 (Apr. 2003), pp. 241–245.

[172] W. Horsthemke and R. Lefever. "Noise-induced transitions: Theory and application in physics, chemistry, and biology". *Springer Series in Synergetics, Springer-Verlag, Berlin* 15 (1984).

[173] D. Frenkel and A. J. C. Ladd. "New Monte Carlo method to compute the free energy of arbitrary solids. Application to the fcc and hcp phases of hard spheres". *The Journal of Chemical Physics* 81.7 (Oct. 1, 1984), pp. 3188–3193.

[174] S. Luding, E. Clément, A. Blumen, J. Rajchenbach, and J. Duran. "Anomalous energy dissipation in molecular-dynamics simulations of grains: The "detachment" effect". *Physical Review E* 50.5 (Nov. 1, 1994), pp. 4113–4122.

[175] S. Luding, E. Clément, A. Blumen, J. Rajchenbach, and J. Duran. "Studies of columns of beads under external vibrations". *Physical Review E* 49.2 (Feb. 1, 1994), pp. 1634–1646.

[176] J. Duran. *Sands, Powders, and Grains*. Partially Ordered Systems. Springer New York, 2000.

[177] B. A. Grzybowski and G. M. Whitesides. "Macroscopic Synthesis of Self-Assembled Dissipative Structures". *The Journal of Physical Chemistry B* 105.37 (Sept. 1, 2001), pp. 8770–8775.

[178] J. G. Kirkwood and E. M. Boggs. "The Radial Distribution Function in Liquids". *The Journal of Chemical Physics* 10.6 (June 1, 1942), pp. 394–402.

[179] J. P. Hansen and I. R. McDonald. "Statistical mechanics of dense ionized matter. IV. Density and charge fluctuations in a simple molten salt". *Physical Review A* 11.6 (June 1, 1975), pp. 2111–2123.

[180] G. T. Seidler, G. Martinez, L. H. Seeley, K. H. Kim, E. A. Behne, S. Zaranek, B. D. Chapman, S. M. Heald, and D. L. Brewe. "Granule-by-granule reconstruction of a sandpile from x-ray microtomography data". *Physical Review E* 62.6 (Dec. 1, 2000), pp. 8175–8181.

[181] T. Aste. "Variations around disordered close packing". *Journal of Physics: Condensed Matter* 17.24 (2005), S2361.

[182] G. Mason. "Radial Distribution Functions from Small Packings of Spheres". *Nature* 217.5130 (Feb. 1968), pp. 733–735.

[183] P. J. Steinhardt, D. R. Nelson, and M. Ronchetti. "Bond-orientational order in liquids and glasses". *Physical Review B* 28.2 (July 15, 1983), pp. 784–805.

[184] J. H. Lambert. *Photometria sive de mensura et gradibus luminis, colorum et umbrae*. Eberhard Klett, 1760.

[185] A. Beer. "Bestimmung der Absorption des rothen Lichts in farbigen Flüssigkeiten". *Annalen der Physik* 162.5 (1852), pp. 78–88.

[186] J. Radon. "On the determination of functions from their integral values along certain manifolds". *IEEE Transactions on Medical Imaging* 5.4 (Dec. 1986), pp. 170–176.

[187] C. Suplee. *XCOM: Photon Cross Sections Database*. NIST. Sept. 17, 2009. URL: https://www.nist.gov/pml/xcom-photon-cross-sections-database (visited on 08/07/2018).

[188] S. Weis and M. Schröter. "Analyzing X-Ray tomographies of granular packings". *Review of Scientific Instruments* 88.5 (2017), p. 051809.

[189] C. Tomasi and R. Manduchi. "Bilateral filtering for gray and color images". *Sixth International Conference on Computer Vision (IEEE Cat. No.98CH36271)*. Jan. 1998, pp. 839–846.

[190] G. Bradski. *The OpenCV Library*. URL: https://opencv.org/ (visited on 08/07/2018).

[191] S. Lloyd. "Least squares quantization in PCM". *IEEE Transactions on Information Theory* 28.2 (Mar. 1982), pp. 129–137.

[192] A. K. Jain. "Data clustering: 50 years beyond K-means". *Pattern Recognition Letters*. Award winning papers from the 19th International Conference on Pattern Recognition (ICPR) 31.8 (June 1, 2010), pp. 651–666.

[193] J. Hoshen and R. Kopelman. "Percolation and cluster distribution. I. Cluster multiple labeling technique and critical concentration algorithm". *Physical Review B* 14.8 (Oct. 15, 1976), pp. 3438–3445.

[194] P.-E. Danielsson. "Euclidean distance mapping". *Computer Graphics and Image Processing* 14.3 (Nov. 1, 1980), pp. 227–248.

[195] S. Frank-Richter. "Dichte ungeordnete Packungen in drei Dimensionen". Diploma thesis. Feb. 2011.

[196] S. Frank-Richter. "Disordered Binary Granular Packings in Three Dimensions". PhD thesis. May 2014.

[197] F. M. Schaller, M. Neudecker, M. Saadatfar, G. Delaney, K. Mecke, G. E. Schröder-Turk, and M. Schröter. "Tomographic analysis of jammed ellipsoid packings". *AIP Conference Proceedings* 1542.1 (June 18, 2013), pp. 377–380.

[198] A. Schella, S. Weis, and M. Schröter. "Charging changes contact composition in binary sphere packings". *Physical Review E* 95.6 (June 15, 2017).

# 6  FORCE TRANSMISSION IN GRANULAR MEDIA

Results published in:

Chen, H., Hess, S., Haeberle, J., Pitikaris, S., Born, P., Güner, A., Sperl, M. & Tekkaya, A. E. (2016). Enhanced granular medium-based tube and hollow profile press hardening. CIRP Annals-Manufacturing Technology, 65(1), 273-276.

Force transmission in granular media is influenced by boundary conditions and the granular force network. We show that in an indentation experiment, the forces decay exponentially with distance from the punch and that higher wall friction leads to a greater buildup of forces near the punch. We additionally show that the shape of the punch determines the force network and that a round punch leads to a more homogeneous distribution of forces in the granular medium compared to a flat punch. Finally, we show that the displacements inside a semi-confined granular medium are more localized when the punch is flat, while they extend further into the packing for the round punch.

## 6.1  INTRODUCTION

Force transmission and plastic deformation proceed fundamentally different in granular media than in gas and liquid. Strongly fluctuating force distributions[4, 44], history dependent response functions [153] and shear banding [199] are examples of phenomena where a grain-scale description of the granular medium is required for an explanation. In granular media, forces can only be transmitted through contacts, leading to what is typically called a force network. Stress birefringent measurements reveal that only a fraction of all particles participate in this force network. The reliability of models that accurately describe granular media depend strongly on the observed length scales [154].

Interactions with container walls set the boundary conditions for the force balance defining the force network. An example where the grain scale behavior of granular media is important to consider is the Janssen granular column [25]. Although Janssen originally used a continuum model to accurately describe the pressure on the bottom

of a silo filled with grains as a function of filling height, a more modern investigation of the problem [200] found that a continuum model description underestimated a measured overshoot effect by a factor of 30 to 40.

In this chapter we investigate the stress response of granular media subjected to various external parameters. The force network in response to a static load is investigated for varying friction with container walls and for different punch shapes. In addition, we measure the displacements inside a semi-confined granular medium in response to a flat or round punch.

## 6.2 EXPERIMENTAL METHODS AND RESULTS

We use stress birefringent epoxy resin discs (Vishay PS4) of sizes 3 mm and 4.5 mm for all experiments. Stress birefringent materials rotate the polarization direction of incoming light by a certain amount based on the materials local stress state. A setup as shown in figure 6.1a can be used to make the stresses inside a two dimensional granular medium visible. Light from the light source (e) passes through the bottom polarizer (d). If the granular medium on the plate (c) is unstressed, the second polarizer (b) will filter the incoming light and the picture recorded by the camera (a) will appear dark. If the granular medium is stressed, this will induce a angular retardation $\delta$ proportional to the principal stress $\tau_{pr} = \sigma_1 - \sigma_2$ [201]:

$$\delta = \frac{2\pi dk\tau_{pr}}{\lambda} \tag{VI–1}$$

where $k$ is the stress-optical coefficient of the material found by calibration, $d$ is the thickness of the discs and $\lambda$ is the wavelength of the light. The measured intensity will behave as $I = I_0 \sin^2(\delta)$ and so for high enough forces a fringe pattern consisting of dark and bright regions will emerge. The exact contact forces including tangential forces can be determined by fitting a computer generated stress pattern based on Hertzian contacts [31] to the recorded fringe pattern. By also recording an image without the second polarizer (b in fig. 6.1a), we can determine the particle centers by fitting circles to the images. The setup was built by Sebastian Pitikaris who also did image analysis and calculation of the forces and positions for the following experiments. Additional details can be found in ref. [202].

We study the effects of external parameters influencing force propagation in granular media in three experiments. In the first experiment, we lowered the friction between discs and wall by applying teflon tape to the otherwise rough wall. A flat punch is used to indent the confined granular medium by a fixed amount.The force network as it develops for low friction (left) and high friction (right) between particles and wall is shown in figure 6.2. A quantitative analysis of the forces measured in figure 6.2 reveals that the forces fade with increasing distance from the punch (see fig. 6.3) and that for the same displacement, higher forces build up near the punch in the sticky boundary case. A stretched exponential decay fit of the form

$$F(x; a, b, c) = ae^{-bx^c} \tag{VI–2}$$

agrees well with the data. The exponent $c$ is 0.52 and 0.68 for the slip and stick boundary, respectively. In a second experiment we compare indentation of the granular

(a) Schematic of setup



(b) Discs used in experiment.
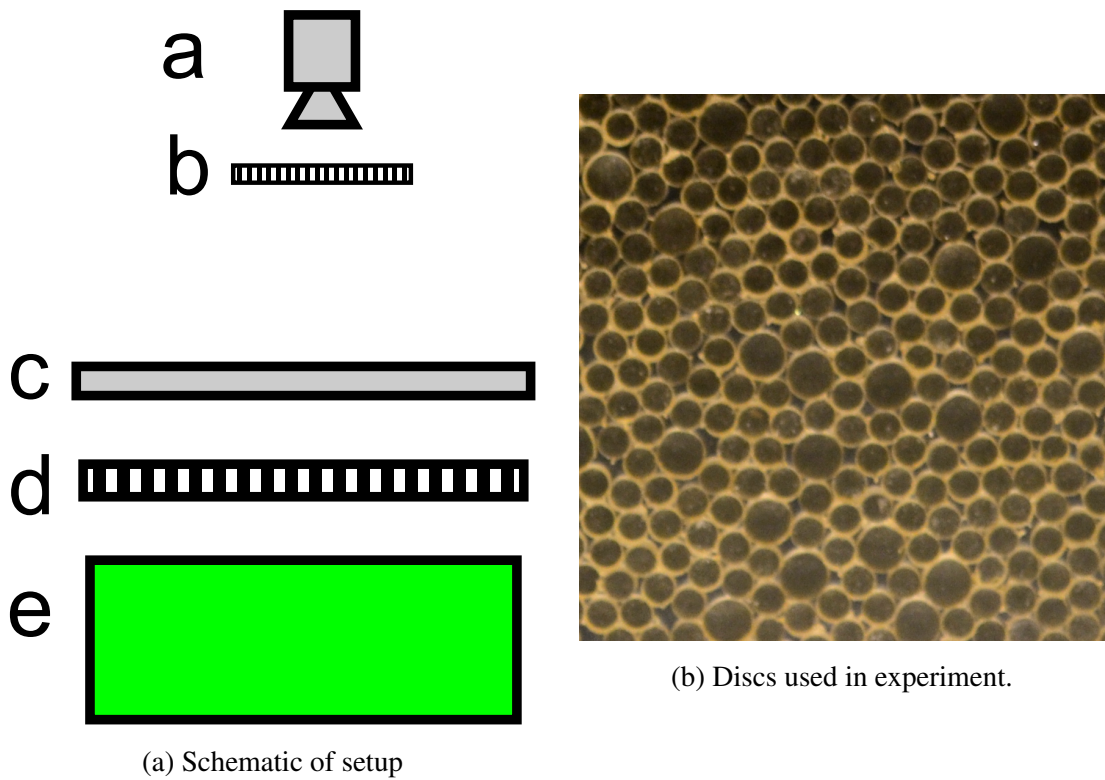
Figure 6.1: Drawing of the setup used to record the stress-birefingent images. Components are: a) Camera, b) removable circular polarizer, c) plate with discs, d) circular polarizer crossed with b, e) green light source.
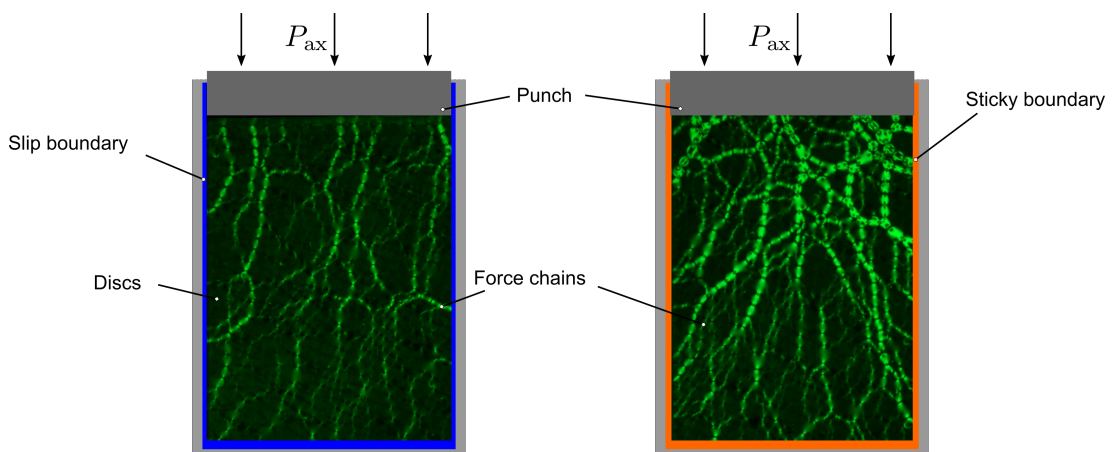


Figure 6.2: Force chains form as the granular medium is indented by a punch. Bright areas correspond to areas with increased contact forces. In the left picture, the friction between particles and wall is higher than in the right picture.
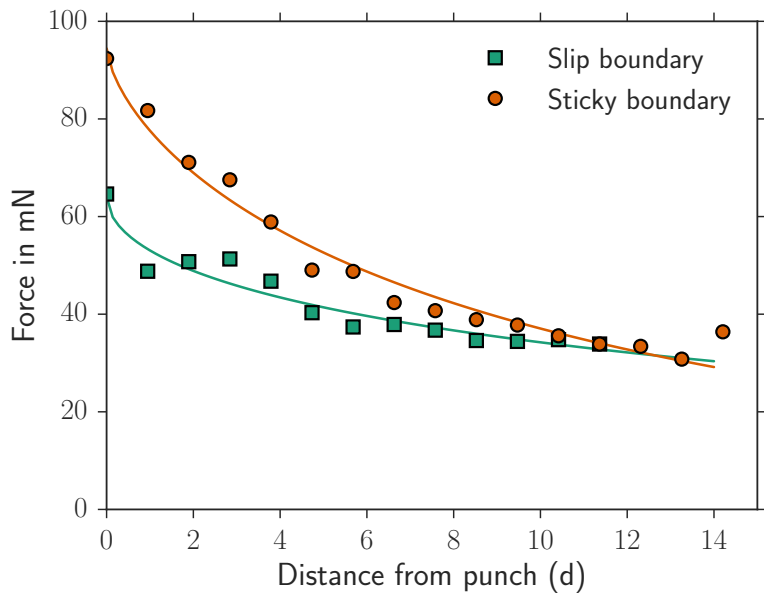
Figure 6.3: Contact forces of packings shown in figure 6.2 averaged over all pixels a certain distance away from the punch. The contact forces decrease with increasing distance from the punch in agreement with the shown stretched exponential decay fits.
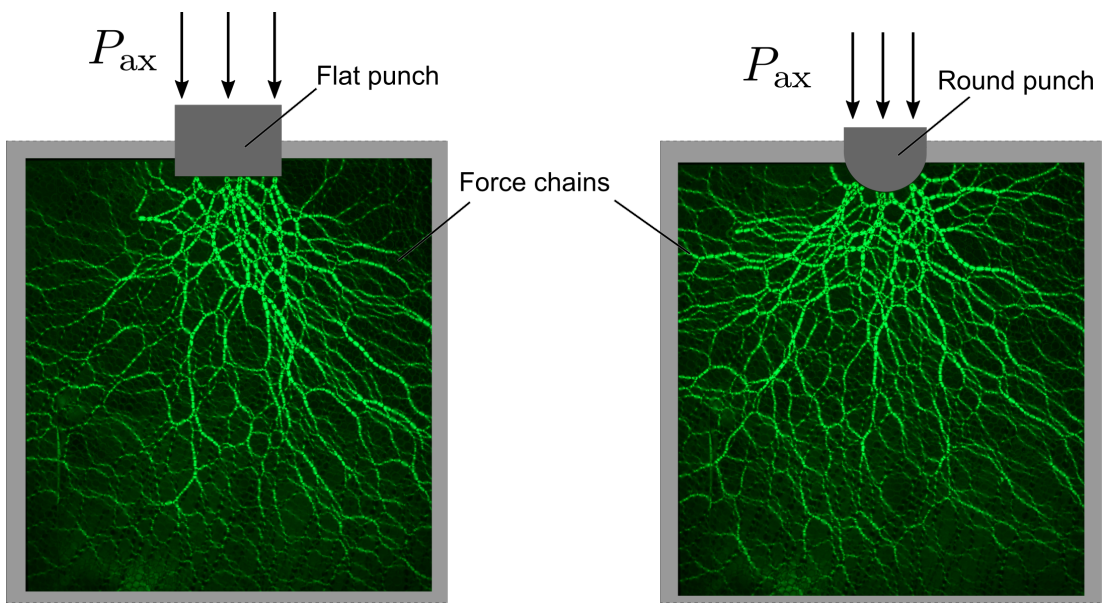


Figure 6.4: Force network appearing in a compressed granular medium for a flat punch (left) and a round punch (right).
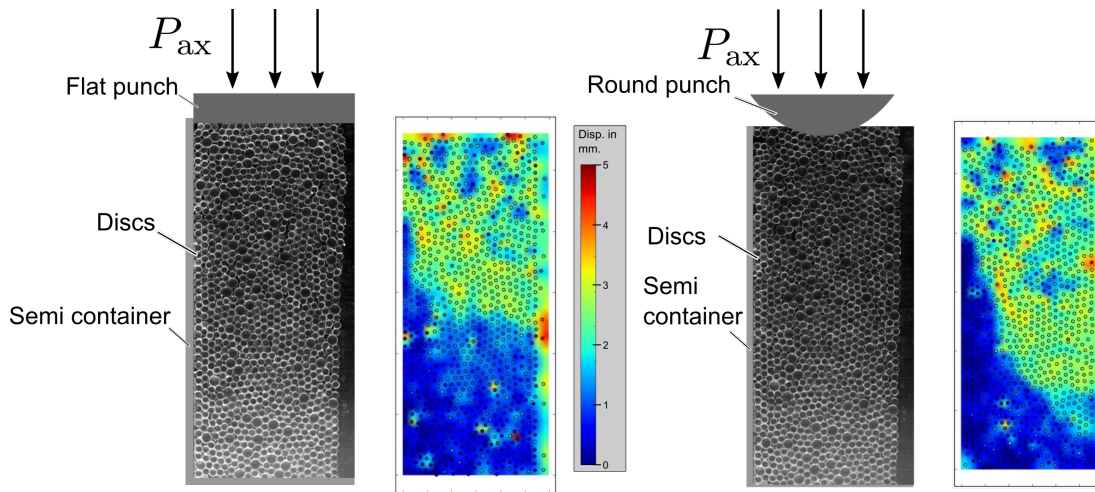
Figure 6.5: Displacements of discs when indentation is applied by a flat punch (left) and a round punch (right). In each case, the discs are only confined on the left and bottom wall but free to move to the right side.

medium with a flat punch to that of a round punch. The force chains that develop are locally aligned with the punch shape, i.e. vertical for the flat punch (see fig. 6.4, left) and radially for the round punch (see fig. 6.4, right). In a third experiment, we measure the displacements inside the granular medium when indented by a flat (see fig. 6.5, left) or round (fig. 6.5, right) punch. The granular medium is confined by walls to the left and bottom but free to move to the right. The particle displacement is the total movement before and after indentation determined by tracking particle positions over a series of images. For the flat punch, displacements are more localized to the region around the punch while for the round punch, movement can be measured a greater distance away from the punch.

## 6.3 Discussion

Our results highlight the influence of external parameters like wall friction and punch shape on mechanical properties of granular media. Container walls set the boundary conditions to the force-balance problem imposed on the granular medium. Our results show that a lower wall friction coincides with lower forces building up near the punch for identical indentation. Forces transmitted from the punch will be repartitioned by the contact network within the granular medium leading to some force chains ending at the container walls at an angle. The Coulomb criterion for contacts with the wall limits the angles that are mechanically stable and therefore the maximum force that can be transferred to the wall. In other words, if the friction with the walls is lowered, the discs near the wall will tend to rearrange rather than arch.

When the flat punch is replaced with a round punch, we see that the force chains locally align perpendicular to the punch surface. While branching leads to redistribution of forces in both cases, the round shape of the piston leads to more force chains entering e.g. the top corners than is observable for the flat punch. The force network appears more isotropic for the round punch than the flat punch.

Punch shape not only influences force propagation but also the way a granular medium rearranges in response to an indenter. The rearrangements occur markedly localized, comparable with the formation of shear bands. In the heterogeneous force network of the flat indenter, the displacements appear only close to the punch, while displacements for the round punch were visible nearly throughout the sample.

## 6.4 Conclusion

In conclusion, the frictional nature of the granular media and the localization of plastic deformation can be expected to strongly affect mechanical behavior. The friction among the particles and with the tube walls yields an exponential decay of externally applied forces within the medium, while the shape of the punch can determine the force propagation and the plastic behavior of the granular medium.

# Bibliography

[4]    T. S. Majmudar and R. P. Behringer. "Contact force measurements and stress-induced anisotropy in granular materials". *Nature* 435.7045 (June 2005), pp. 1079–1082.

[25]   H. Janssen. "Versuche über Getreidedruck in Silozellen". *Zeitschr. d. Vereins deutscher Ingenieure* 39.35 (1895), pp. 1045–1049.

[31]   H. Hertz. "Ueber die Berührung fester elastischer Körper". *Journal für die reine und angewandte Mathematik* 92 (1882), pp. 156–171.

[44]   D. L. Blair, N. W. Mueggenburg, A. H. Marshall, H. M. Jaeger, and S. R. Nagel. "Force distributions in 3D granular assemblies: Effects of packing order and inter-particle friction". *Physical Review E* 63.4 (Mar. 27, 2001).

[153]  A. P. F. Atman, P. Brunet, J. Geng, G. Reydellet, G. Combe, P. Claudin, R. P. Behringer, and E. Clément. "Sensitivity of the stress response function to packing preparation". *Journal of Physics: Condensed Matter* 17.24 (2005), S2391.

[154]  C. Goldenberg and I. Goldhirsch. "Small and large scale granular statics". *Granular Matter* 6.2 (2004), pp. 87–96.

[199]  P. V. Lade. "Instability, shear banding, and failure in granular materials". *International Journal of Solids and Structures* 39.13 (June 2002), pp. 3337–3357.

[200]  G. Ovarlez, C. Fond, and E. Clément. "Overshoot effect in the Janssen granular column: A crucial test for granular mechanics". *Physical Review E* 67.6 (June 30, 2003).

[201]  M. M. Frocht. "Photoelasticity, vol. II". *N. York* (1948), p. 333.

[202]  S. Pitikaris. "Local Mechanical Properties of Granular Media" (2017), p. 163.

# 7 Summary and Conclusions

In this thesis we investigated ways in which microscopic interactions between grains in granular media can be controlled and the ways in which this influences the macroscopic behavior of the granular medium.

We have found that tuning frictional properties of zirconia beads is possible using three commercially available solid lubricants as well as a PECVD based carbofluorination technique we adapted for use with granular particles. We measured that while all tested surface treatments lead to a reduction of the static friction coefficient against a smooth surface, some surface treatments actually lead to an increase in particle-particle friction coefficient. This behavior could be related to an increased roughness due to agglomeration of the lubricant at the surface which has little influence when in contact with a smooth surface but leads to an increase in friction due to interlocking in particle-particle contacts.

We quantified the flowing behavior of the tailored granular media using two quantities: the tensile strength which is a measure for how easy it is to induce flow of the granular medium and the continuous yield limit, which represents the energy which must be expended to keep the medium in a steady state of flowing. Here we found that the tensile strength was anti correlated to the static friction coefficient which we explained by considering the looser mechanically stable packing that can be achieved for frictional particles and as such the tensile strength is defined by the packing structure and the preparation history. The continuous yield limit was found to increase with increasing particle-particle friction, in agreement with the model of velocity-independent friction in shear bands.

Our measurements show that the surface treatments also changed contact angle and triboelectric charging behavior, but neither of those effects could be correlated to macroscopic quantities. In particular, we did not see a decrease of the tensile strength with increasing contact angle, likely because liquid bridge formation was negligible given that all surfaces exhibited relatively high contact angles and the experiments were done in dried air.

Additionally, our measurements show a decrease of the measured air pressure in front of the granular column as a consequence of shearing the granular medium at gas velocities below fluidization. This phenomenon can be explained by density fluctuations causing a local decrease of the granular gas resistance.

A new approach to influencing the packing structure using the triboelectric charg-

ing was presented. In this context, an extensive study about the stochastic nature of triboelectric charging was conducted with the result that the distribution of charges exchanged in a single or multiple collisions follows a unique shape exhibiting fat-tailedness and asymmetry. For the same material combinations, charges of both signs could be observed. We offered a model that reproduces many of these results and is based on a discharge step immediately following the triboelectric charge exchange step. We show that surface treatments can indeed influence the tribocharging behavior but that such surface modifications only change the parameters of the tribocharging distribution, not the shape of the distribution itself.

Our experiments on the influence of tribocharging on the packing structure show that in packings of monodisperse equal number mixtures of teflon and nylon spheres exposed to vertical vibrations ordering according to the material occurs and a CsCl-like structure is formed. This behavior is most consistent with a system driven by electrostatic potential minimization such as it occurs in an ionic crystal. Structural deviations from a perfect CsCl structure were measured which could be due to gravitational compression and perhaps discharging effects from radiation exposure during the tomography.

A reference experiment consisting of the same number of spheres that are all made of teflon instead exhibited an amorphous structure, further indicating that charge potential minimization is what drives the ordering process in the teflon and nylon mixture system.

A third experiment which was conducted in a container with flat walls and where charging against the container was not prevented revealed that in such an environment the granular packing structure is determined by interactions with the wall which lead to ordering in a dense polycrystalline structure near the wall and an amorphous structure in the bulk.

Finally, we investigated the influence of boundary conditions on the force propagation and displacement behavior of granular media in a two dimensional model system. We found that lower wall friction reduced the amount of pressure that builds up right in front of the piston and lead to a more homogeneous pressure profile. We additionally showed that using a round instead of a flat piston leads to a more homogeneous force distribution and displacement field if the confinement of one wall is removed.

## 7.1 Outlook

The experiments presented in this thesis reveal interesting connections between the microscopic interactions and macroscopic behavior of granular media. However, there are still many open questions and possible continuations of the work presented here.

### Friction properties and rheological experiments

- A big part of the argument of why particle particle friction was different from static friction against a smooth surface was an increase roughness on the surface as apparent from SEM. A more quantitative method like vertical scanning interferometric microscopy [39] would allow to determine the exact size of asperities and their frequency.

- The cause of the roughness increase is believed to be an agglomeration of the solid lubricant on the surface. Reducing the amount of the additive or changing the vibration protocol during dispersion could be a way to maintain the reduction in friction without the increase in roughness.

- We have investigated the properties of surface treated zirconia beads which are used in milling processes because of their hardness and chemical resistance. Contrasting this material to a softer one e.g. a polymer would be an interesting way to test the generality of the observations made in our experiments. Additionally, scaling the particle size would be a great way of testing the same generality.

- We performed the particle-particle friction coefficients by controlling the rotation rate and measuring the torque required for rotation. An alternative approach where the torque is set and the rotation rate is measured would allow determining the static particle-particle friction coefficient.

- In the rheological measurements, using a different geometry like Couette cell geometry would be interesting way to test how sensitive the observations we made are to the boundary conditions of the setup.

- There exist surface coatings that aid in dissipating charges accumulated at the container wall. By applying such a surface coating, charging against the wall could be reduced and the influence of charging in this experiment could be investigated.

- We measured a decrease of air pressure when some air flow is provided and the material is sheared. We believe that this is due to packing density inhomogeneities but this theory could be tested with methods such as DWS or X-ray radiography. By correlating the measurements of both methods, the decrease in air pressure could be established as a metric for density inhomogeneities.

EXPERIMENTS ON TRIBOCHARGING

- In our experiments we varied material combinations, number of collisions, humidity and surface treatments and found the same characteristic features of the triboelectric charge distribution. Still, additional factors such as breakdown voltage of the surrounding gas, kinetic energy of impact or extreme humidities would be interesting to investigate.

- In our experiments we investigate both single collisions and multiple collisions. However, the experiments with multiple collision have the disadvantage that we do not know how many collisions are involved. A sensible extension of the work would be to create a setup in which two collisions are performed by the same particle. An example of how such a setup could look like is shown in figure 7.1. With such a setup, it would even be possible to make one of the plate materials different to the other and measure e.g. the distribution when a sphere first hits a copper plate and then a PTFE plate.

- With the setup as we have built it studying same-material tribocharging could be highly interesting. We attempted to measure PMMA particles colliding with a PMMA tube but these experiments yielded too low of a charge to be reliably measured. Other combinations like glass colliding with glass could be tested.

- We have demonstrated that surface treatments are effective at changing the charging behavior of materials. It would be interesting to compare the surface treated particles to particles of the raw material that the surface treatment is attempting to replicate. In particular, the silanization with PTMS that gives glass spheres properties similar to PTFE could be compared to raw PTFE. One problem with this is that changing the bulk material will inevitably have additional consequences like changing the collision dynamics which would alter the charging behavior as well.
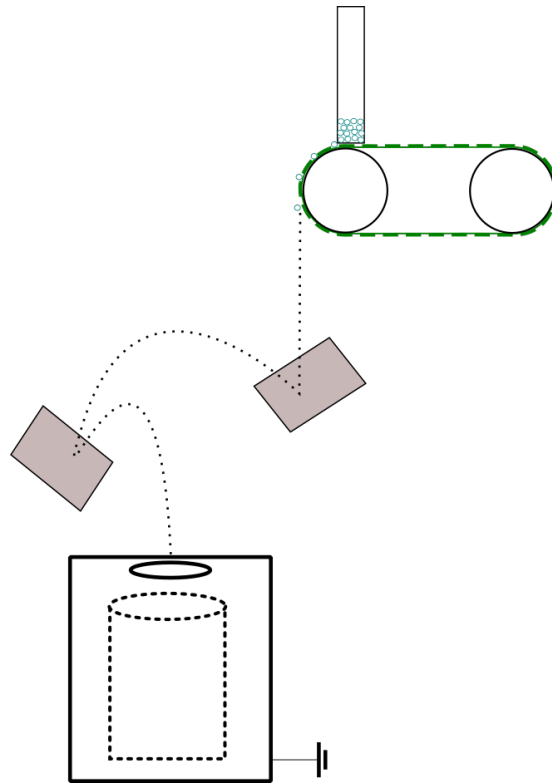
Figure 7.1: Suggested setup for studying the two collision tribocharging distribution.

- We have demonstrated that in binary mixtures of monodisperse spheres, tribocharging can lead to ordering according to a structure which minimizes electrostatic potential. We have also shown that surface treatments can be used to influence the tribocharging behavior. A natural extension of this work would be to show that the packing structure can be influenced simply by surface coating half of the spheres in the packing. We have already attempted this and measured the charge distribution (see figure 7.2) in a packing where half the spheres are made of nylon and half the spheres are made of nylon but were coated with hexafluoropropene using the carbofluorination technique described in section 2.6.1. The distribution was qualitatively similar to the distribution in packings of teflon and nylon spheres. However, the magnitude of the charges in the experiment where surface treatements were used was lower and no ordering in a crystal lattice could be observed when vertically vibrating at the standard protocol. An additional obstacle here is that the surface treated nylon spheres look identical in the X-ray tomographies and so we can not see chemical ordering, i.e. surface
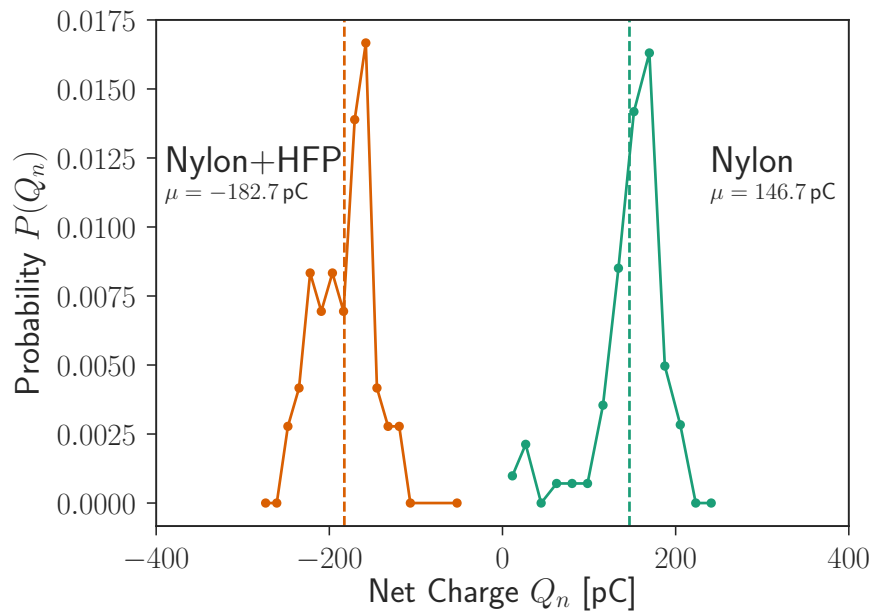
Figure 7.2: Charge distribution of an equal number mixture of nylon beads and nylon beads whose surface was treated with hexafluoropropene after being subjected to vibrations for 30 minutes. The distributions are qualitatively similar to those in a teflon and nylon mixture, but the magnitudes of the means are lower.

treated nylon spheres preferentially being close to untreated spheres.

- We have shown that the container geometry has a great influence on the packing structure. By modifying the container geometry to be compatible with one particular crystal structure, this might enable us to make the system tend towards these structures. Being able to set up a granular system in various crystalline configurations would be an invaluable tool for researchers who investigate mechanical properties of such packings. Recently, Wang et al. [203] have presented a method that allows them to arbitrarily control the two dimensional patterning of millimeter sized polymer beads on a substrate. If this technology could be adapted to provide a pattern compatible with one particular crystal structure, we might be able to control the packing structure even more.

- In our studies, we have always used the same vibration protocol. Varying this parameter is an obvious candidate for influencing the ordering process.

- We have measured that the X-rays that the packing is exposed to can alter the packing structure. Perhaps a quick low resolution scan could be performed to

measure the particle positions before discharging by the X-rays. The differences in packing structure before and after radiation would allow us to estimate how many contacts in the sample are being held stable specifically by electrostatic charging.

- Finally, a study on the mechanical properties of the granular crystal would be of great interest. Measuring the tensile strength could help us further quantify the strength of the Coulombic forces. An alternative approach would be to remove the top of the container after the crystal has formed but when the sample is still on the vibrating table. We could then increase the strength of the vibrations and determine the point when the vibrations become strong enough to destroy the crystal.

EXPERIMENTS ON FORCE PROPAGATION IN GRANULAR MEDIA

- The experiments we have performed could be extended to three dimensional experiments testing the influence of wall friction and punch shape in a granular column. The advantage of the two dimensional setup is that we can evaluate the exact forces on every particle. Some approaches for three dimensional force tomography exist but they only work for soft particles [204, 205] or a small number of particles [206, 207]. Alternatively, the stresses could only be determined at the container walls using stress birefringence.

- If a setup for measuring the three dimensional force distribution existed, it would be of interest to test the crystalline structures produced in chapter 5 with regards to their force propagation properties.

- We tested the displacement behavior when one wall is removed. It would be interesting to see how this behavior changes if the missing wall is replaced by an elastic border providing a resistance to the deformations.

# BIBLIOGRAPHY

[39]    S. Utermann, P. Aurin, M. Benderoth, C. Fischer, and M. Schröter. "Tailoring the frictional properties of granular media". *Physical Review E* 84.3 (Sept. 22, 2011).

[203]   Y. Wang, X. Y. Wei, S. Y. Kuang, H. Y. Li, Y. H. Chen, F. Liang, L. Su, Z. L. Wang, and G. Zhu. "Triboelectrification-Induced Self-Assembly of Macro-Sized Polymer Beads on a Nanostructured Surface for Self-Powered Patterning". *ACS Nano* 12.1 (Jan. 23, 2018), pp. 441–447.

[204]   M. Saadatfar, A. P. Sheppard, T. J. Senden, and A. J. Kabla. "Mapping forces in a 3D elastic assembly of grains". *Journal of the Mechanics and Physics of Solids* 60.1 (Jan. 2012), pp. 55–66.

[205]   N. Brodu, J. A. Dijksman, and R. P. Behringer. "Spanning the scales of granular materials through microscopic force imaging". *Nature Communications* 6 (Mar. 5, 2015), p. 6361.

[206]   C. M. Wensrich, E. H. Kisi, J. F. Zhang, and O. Kirstein. "Measurement and analysis of the stress distribution during die compaction using neutron diffraction". *Granular Matter* 14.6 (Nov. 2012), pp. 671–680.

[207]   J. M. Laskar, P. Shravan Kumar, S. Herminghaus, K. E. Daniels, and M. Schröter. "High refractive index immersion liquid for superresolution 3D imaging using sapphire-based aplanatic numerical aperture increasing lens optics". *Applied Optics* 55.12 (Apr. 20, 2016), p. 3165.

# LIST OF FIGURES

182

184

# Danksagung

Das Anfertigen dieser Arbeit wäre nicht möglich gewesen ohne die Hilfe einiger bestimmter Menschen bei denen ich mich hier bedanken möchte. Mein Danke geht zuallererst an meinen Doktorvater Prof. Dr. Matthias Sperl und an meinen Betreuer Dr. Philip Born, die mir jederzeit mit Rat zur Seite standen und mich bei allen meinen Ideen stets unterstützt haben.

Außerdem möchte ich mich bedanken bei allen Mitarbeitern des Institut für Umformtechnik und Leichtbau der TU Dortmund für die erfolgreiche und konstruktive Zusammenarbeit und bei Prof. Dr. Dr. Erman Tekkaya dafür, dass er das Projekt ermöglicht hat und sich bereit erklärt hat, meine Arbeit zu bewerten.

Ich bedanke mich besonders bei Philip Born, Till Kranz und Koray Önder für das Korrekturlesen meiner Arbeit.

Diese Arbeit wäre sicherlich nicht in diesem Umfang möglich gewesen, wenn ich nicht die Hilfe zahlreicher Studenten gehabt hätte. Deshalb bedanke ich mich bei Christoph Hansen, der als Bachelorstudent maßgeblich am Design meines fluidisierten Bettes beteiligt war; bei Sarah Nefzger, die während ihrer Bachelorarbeit und als Werksstudentin durch viel (systematisches) Ausprobieren das Silanisieren von Glasteilen perfektioniert hat; bei Stephanie Oppelt, die während ihrer Bachelorarbeit und als Werksstudentin maßgeblich an den Experimenten zur Reibungsmodifikation und deren Auswirkungen auf das Fließverhalten beteiligt war; und bei Janni Harju, die während eines RISE Praktikums des DAAD entscheidend bei den Experimenten zu Strukturanalyse und Kristallisation in geladenen Systemen mitgewirkt hat. Weiterhin möchte ich mich für die Hilfe beim Erstellen technischer Zeichnungen bei Alexandre Meurisse, Olfa Lopez und Anabelle Horb bedanken.

Weiterhin bedanke ich mich bei jedem Mitglied unserer Arbeitsgruppe, wegen denen die Arbeitsatmosphäre immer angenehm war und man stets mit jemandem über seine Probleme sprechen konnte. Vor allem das fast tägliche Kicker Spielen hat während der Zeit hier sicherlich zur Schonung der Nerven beigetragen.

Zum Schluss bedanke ich mich noch bei meinen Eltern Ingrid Haeberle und Thomas Haeberle bedanken, dafür sie mir diesen Weg ermöglicht haben und immer an mich geglaubt haben. Natürlich beschränkt sich dieser Dank nicht nur auf die finanzielle Unterstützung während Studium und diverser Abenteuer im Ausland, sondern auch dafür, dass ich mich stets auf eure Hilfe verlassen konnte.

Bei der Deutschen Forschungsgemeinschaft (DFG) bedanke ich mich für die Finanzierung meines Projekts.

## ERKLÄRUNG ZUR DISSERTATION

Ich versichere, dass ich die von mir vorgelegte Dissertation selbstständig angefertigt, die benutzten Quellen und Hilfsmittel vollständig angegeben und die Stellen der Arbeit – einschließlich Tabellen, Karten und Abbildungen –, die anderen Werken im Wortlaut oder dem Sinn nach entnommen sind, in jedem Einzelfall als Entlehnung kenntlich gemacht habe; dass diese Dissertation noch keiner anderen Fakultät oder Universität zur Prüfung vorgelegen hat; dass sie – abgesehen von unten angegebenen Teilpublikationen – noch nicht veröffentlicht worden ist sowie, dass ich eine solche Veröffentlichung vor Abschluss des Promotionsverfahrens nicht vornehmen werde. Die Bestimmungen dieser Promotionsordnung sind mir bekannt. Die von mir vorgelegte Dissertation ist von Prof. Dr. Matthias Sperl betreut worden.

☐ Teilpublikationen liegen nicht vor.
☒ Nachfolgend genannte Teilpublikationen liegen vor:

Chen, H., Hess, S., Haeberle, J., Pitikaris, S., Born, P., Güner, A., Sperl, M. & Tekkaya, A. E. (2016). Enhanced granular medium-based tube and hollow profile press hardening. CIRP Annals-Manufacturing Technology, 65(1), 273-276.

Haeberle J, Schella A., Sperl M., Schröter M., & Born P. (2018). Double origin of stochastic granular tribocharging. Soft Matter, 14, 4987-4995.

**Promotionsbeginn:**                  01.Juni 2015
(Beginn der praktischen Arbeit)

**Promotionsende:**
(Monat der mündlichen Prüfung)      Januar 2019

Ich versichere, dass ich alle Angaben wahrheitsgemäß nach bestem Wissen und Gewissen gemacht habe und verpflichte mich, jedmögliche, die obigen Angaben betreffenden Veränderungen, dem Dekanat unverzüglich mitzuteilen.

_____      _____
Datum                          Unterschrift

# Biography

Jan Haeberle was born 28.June 1989 in Fürth (Bayern). He attended Altes Kurfürstliches Gymnasium in Bensheim, where he obtained his Abitur in 2008. During this period, he spent one semester at Otumoetai College in Tauranga, New Zealand in 2005. He graduated with a bachelor of science in physics at Karlsruhe Institute of Technology (KIT) in 2012. He continued his studies at the University of Edinburgh, where he graduated with first class honours to obtain the masters of physics degree in 2014. Since 2015, Jan Haeberle has been working at the Institute of Materials Physics in Space at the German Aerospace Center (DLR) in pursuit of a Ph.D. in physics.

# Current Publications

- Chen, H., Hess, S., Haeberle, J., Pitikaris, S., Born, P., Güner, A., Sperl, M. & Tekkaya, A. E. (2016). Enhanced granular medium-based tube and hollow profile press hardening. CIRP Annals-Manufacturing Technology, 65(1), 273-276.

- Haeberle J, Schella A., Sperl M., Schröter M., & Born P. (2018). Double origin of stochastic granular tribocharging. Soft Matter, 14, 4987-4995.

# Conferences and Contributed Presentations

- Strength of Tailored Granular Media in a Fluidized Bed. Condensed Matter Days 26, (2016), Groningen, the Netherlands.

- Triboelectric Charging of Surface Treated Granular Media, DPG Spring Meeting, (2017), Dresden

- Stochastic Nature of Granular Tribocharging, DPG Spring Meeting, (2018), Berlin

- Stochastic Nature of Granular Tribocharging, Gordon Research Seminar, (2018), Boston, USA

- Stochastic Nature of Granular Tribocharging, Gordon Research Conference, (2018), Boston, USA